2016

Role of Nanosize Effects on the Adsorptive and Catalytic Properties of NiO Nanoparticles towards Heavy Hydrocarbons

Marei, Nedal Nael

UNIVERSITY OF CALGARY

Role of Nanosize Effects on the Adsorptive and Catalytic Properties of NiO Nanoparticles towards Heavy Hydrocarbons

by

Nedal Nael Marei

A THESIS

SUBMITTED TO THE FACULTY OF GRADUATE STUDIES

IN PARTIAL FULFILMENT OF THE REQUIREMENTS FOR THE

DEGREE OF MASTER OF SCIENCE

GRADUATE PROGRAM IN CHEMICAL ENGINEERING

CALGARY, ALBERTA

APRIL, 2016

ABSTRACT

The effect of NiO nanoparticle size was studied to understand its impact on adsorption and catalytic activity during oil recovery and upgrading. A series of different-sized NiO nanoparticles between 5 and 80 nm were prepared. XRD, BET, FTIR, HRTEM and TGA were used to characterize the nanosize effect on the textural properties, shape and morphology. Quinolin-65 (Q-65) was first used as an asphaltene model molecule. Langmuir and Freundlich adsorption isotherms models and computational modeling for the interaction between NiO nanoparticle surface and Q-65 were carried out to understand the adsorption behavior. TGA/DTA and TGA-MS techniques were used to study the effect of NiO nanosizes on catalytic thermo-oxidative decomposition of the adsorbed Q-65.

The entire study was repeated using visbroken residue n-C_5 asphaltenes. For both Q-65 and n-C_5 asphaltene post-adsorption oxidation, the Kissinger-Akahira-Sunose (KAS) kinetic method was used to estimate the kinetic triplets, namely $f(\alpha)$, E_α and A_α.

ACKNOWLEDGEMENTS

I dedicate my first and most significant acknowledgement to my supervisor Dr. Nashaat Nassar who truly inspired me in so many different ways. Your faith and continued encouragement throughout my journey will never be forgotten. I have truly fulfilled my scientific curiosity and pushed all academic boundaries with your support and guidance. I feel lucky to have had the opportunity to join your group for its innovation and creativity. My University of Calgary experience would not have been enriching without our coffee meetings which were truly our daily chemichats, in addition to lots of caffeine injections that kept me working all night. I finally thank you for your financial support through my masters' studies.

I would like to thank Dr. Pedro Pereira Almao who gave me the chance to join one of the most exciting groups on campus, the catalysis group. I was able to benefit from their discussions, lab space and technical meetings.

Dr. Gerardo Vitale and Dr. Azfar Hassan will always be remembered not only for their innovative analysis of the experimental results, but also for their meticulous approaches in the experimental procedures attributed to their chemistry background. They contributed towards my experimental scientific analysis and both were co-authors on my publications. I value all your time, ideas and effort.

A special couple on my team, Amjad and Maryam are recognized for their team spirit both academically and personally. Our research overlaps and that was a great chance for us to collaborate technically. We have learned and taught ourselves many techniques and tools.

I would like to extend a special thanks to all my group members for their continued support and motivation. Tatiana with her advanced ability in Matlab who helped with my experimental results

modeling. Ghada for proof reading, editing my written material and for her continuous inspiration, Abdallah, Jose and Afif for what I would call critical logistic support.

I would like to gratefully acknowledge the Dr. Nassar Group for Nanotechnology Research, the Catalysis and Bitumen Upgrading Group (CBUG), the Department of Chemical and Petroleum Engineering and the Schulich School of Engineering at the University of Calgary.

Finally, my co-authors and I are grateful for all the organizations that have contributed towards my research; Natural Sciences and Engineering Research Council of Canada (NSERC), Nexen-CNOOC Ltd, and Alberta Innovates-Energy and Environment Solutions (AIEES) for the financial support provided through the NSERC/NEXEN/AIEES Industrial Research Chair in Catalysis for Bitumen Upgrading. Also, the contribution of facilities from the Canada Foundation for Innovation, the Institute for Sustainable Energy, Environment and Economy. A special acknowledgement to Dr. Tobias Fürstenhaupt for access to the Microscopy and Imaging Facility of the Health Science Center at the University of Calgary, which receives support from the Canadian Foundation for Innovation and the Alberta Science and Research Authority.

Dedication

To

Mom and Dad, it is impossible to thank you adequately for everything you've done

Dana and Hamoda

All my friends

Palestine with love

Table of Contents

The copyrights forms are attached in a separate file.

List of Tables

List of Figures and Illustrations

CHAPTER ONE: INTRODUCTION

The application of nanoparticles in the oil and gas industries has increased in recent years because of their unique physical and chemical properties. Notwithstanding the great deal of interest in the use of nanoparticles as adsorbents and catalysts for enhancing heavy oil upgrading and recovery, still the effect of nanoparticle size on their adsorption and catalytic behaviour towards heavy hydrocarbons remain unclear. This study opens up new possibilities for manipulating adsorptive and catalytic performance of metal oxide nanoparticles, and widens our general understanding of their surface functionality and chemical activity.

1.1 Background

The global energy demand continually rises with a 12% increase over the last 10 years and is set to only increase (British Petroleum, 2016). Canada oil reserves, the third largest reserves in the world after Venezuela and Saudi Arabia, is around 173 billion barrels (Oil Sands Review, 2016). Of Canada's total reserves, 170 billion barrels are located in Alberta of which 168 billion barrels of bitumen is considered recoverable using today's technology. With new technologies the figure 168 billion is expected to reach 1.8 trillion recoverable barrel (Oil Sands Review, 2016, Alberta Energy, 2016). In February 2016, Canada's oil production reached 4.78 million barrel per day including: conventional light crude oil, heavy crude oil and upgraded bitumen. The total Canadian production is forecasted to grow to 5.5 million barrel per day in 2025 (National Energy Board, 2016, Oil Sands Review, 2016).

Alberta produces more than 2 million barrels of oil sand per day (Oil Sands Review, 2016). However, there are several challenges that face the industry with the heavy oil and bitumen recovery from oil sands due to their heavy and extremely viscous nature. These challenges include,

oil treatment before it is sent to refineries to produce usable fuels, the low prices of oil, the high capital and operating costs, the need for improved crude oil quality, the need to reduce greenhouse gas emissions and the need to focus more on the environmental impacts and to meet environmental regulations (Government of Alberta, 2009). All the extensive processes for the treatment and upgrading contribute to the high capital and operating costs for the production of oil (COYNE, 2016, Oil Sands Review, 2016). Figure 1.1 shows a comparison between the common major oil producing countries in the world for their conventional oil production cost.

Looking at the capital and operating costs for conventional oil production, Canada spends between $40-65 USD to produce oil from oil sands. The price of oil has seen strong fluctuations over the recent years, today it stands at $38 USD which heavily impacts the economy in Alberta since it is below the cost of production.

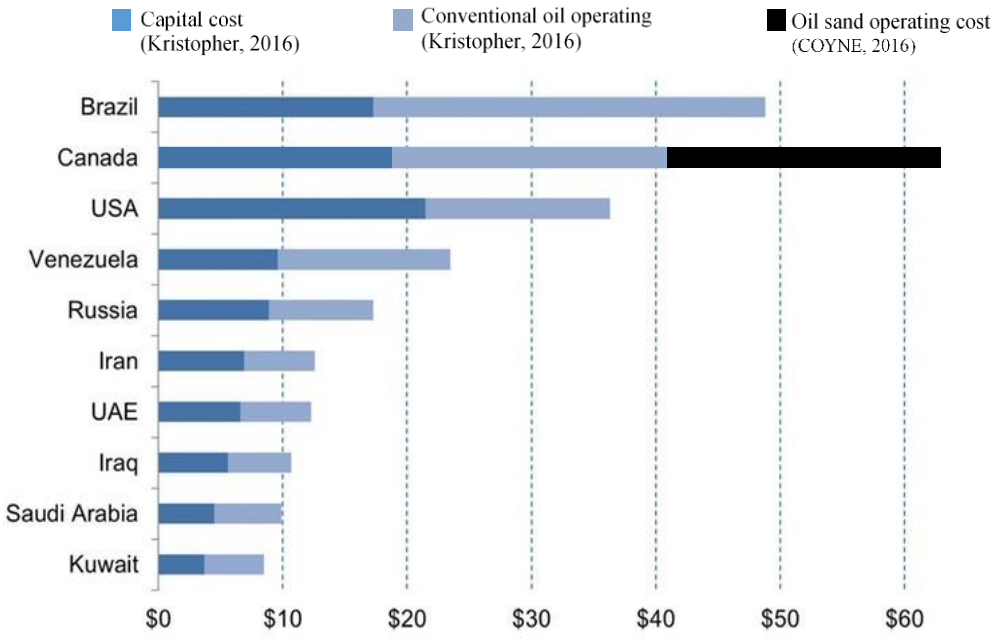

Figure 1.1 Oil production cost by country.

Alberta is taking a loss in their oil production but do continue to produce oil from oil sands "because they cannot just turn the switch off on a $20 billion project." Farouq Ali (COYNE, 2016).

The oil sector must find alternative technologies to produce the oil in which they dramatically reduce the cost per barrel production in order to make profit or at least break even. There is simply not enough profit to sustain the current oil production.

One of the biggest problems facing the heavy oil industry is the presence of asphaltenes, which are one of the most polar, densest and surface active fraction of heavy oil (Chianelli et al., 2007). Asphaltenes are usually responsible for clogging wells, plugging rock pores, changes in reservoir wettability and deposition at the bottom of the wells. It is the presence of asphaltenes that makes oil sand oil upgrading challenging and costly. It also has environmental impacts where it is a significant source of CO_2 emissions (Akbarzadeh et al., 2007).

It is essential to develop a cost-effective and environmental friendly technology for the extraction and exploration processes of oil sands. Therefore, removing the unstable asphaltenes or finding an inhibitor to prevent or delay their precipitation is of paramount importance. High selectivity adsorption techniques, focusing mainly on the removal of asphaltenes rather than on the whole bitumen will considerably improve oil upgrading and recovery efficiency.

Recently, nanotechnology for heavy oil upgrading by the removal of asphaltenes has been attractive to the oil producers due to their unique properties including: high surface area per mass unit, high dispersity, adsorption selectivity and catalytic activity (Nassar et al., 2011a).

To run over the challenges of the unstable polar heavy hydrocarbons, the Nassar's goup at the University of Calgary have recently integrated metal-based nanoparticles to develop the heavy oil quality through deasphalting the heavy oil with environmentally sound nanoadsorbents/catalysts (nanosrbcats). Our research group has established a solid foundation using other peer metal oxide

nanoparticles, such as Co_3O_4, MgO, TiO_2, ZrO_2, CeO_2, Al_2O_3 and CaO nanoparticles as nanoadsorbents, either for adsorption or catalysis towards asphaltene molecules (Franco et al., 2013a, Franco et al., 2013b, Franco et al., 2014, Nassar et al., 2011a, Nassar et al., 2011b, Nassar et al., 2011c, Nassar et al., 2014, Nassar et al., 2013). Other metal oxides were also tested such as Fe_3O_4 and NiO towards the removal of heavy hydrocarbons and catalytic thermal processing. The results were very intriguing (Nassar et al., 2013, Hassan et al., 2013, Nassar et al., 2011a).

In addition, different types of asphaltenes have been investigated in previous studies from different origins and different properties. Nevertheless, some model molecules have been used to mimic the asphaltenes reported structures (Devard et al., 2012, López-Linares et al., 2006). These model molecules represents the asphaltenes due to its similar structure and contents of alkyl chains, aromatic moieties and heteroatoms like sulfur, nitrogen and oxygen such as, Quinolin-65 and Violanthrone-79 (López-Linares et al., 2006). These model molecules represent an asphaltene of the continental type due to the presence of one significant large aromatic area plus side chains per molecule (López-Linares et al., 2006, Devard et al., 2012). Figure 1.2 shows proposed asphaltene molecular structures (a) and the structure of Quinolin-65 the asphaltene model molecule (b).

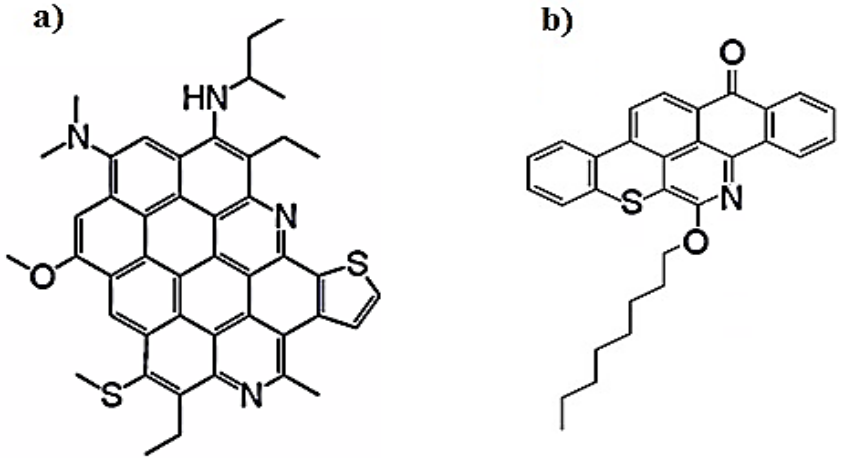

Figure 1.2 a) Proposed molecular structures for petroleum asphaltenes (Hashmi et al., 2012) b) Quinolin-65 chemical structure (López-Linares et al., 2006)

It was found that these model molecules can resemble the adsorption behavior of different asphaltene fractions over different adsorbents, and it is possible to use individual groups of model molecules to simulate adsorption behavior (Nassar et al., 2014, López-Linares et al., 2006).

Despite the great deal of interest in the use of nanoparticles as adsorbents and catalysts for enhancing heavy oil upgrading and recovery, the effect of nanoparticle size on their adsorption and catalytic behaviour towards visbroken heavy hydrocarbons still remains unclear. This study focuses on the effect of NiO nanoparticle size (ranging from 5-80 nm) on adsorption and post-adsorption catalytic oxidation of Quinolin-65 asphaltene model molecule and n-C_5 vis-broken asphaltenes.

1.2 Objectives

The primary objective of this study is to study the effect of nanosize on surface properties of NiO nanoparticles as (nanosorbcats) for adsorptive removal and post adsorption catalytic thermo-oxidative decomposition of heavy hydrocarbons. Specific objectives are as follows:

1. Prepare NiO with different nanosizes and characterize it to investigate the effect of size on its shape, topology, morphology and textural properties.
2. Use Quinolin-65 (Q-65) as a model-adsorbing compound for polar heavy hydrocarbons to investigate the nanosize effect of NiO nanoparticles on the adsorption of Q-65. Apply a mathematical model to describe the behavior of the adsorption process using Langmuir and Freundlich models.
3. Run computational modeling to get better insight on the nanosizes surface and the interaction between the Q-65 molecule and NiO nanoparticle surface.
4. Investigate the nanosize effect of NiO nanoparticles on the post-adsorption catalytic oxidation of the adsorbed species of Q-65 using thermogravimetric analysis and online evolved CO_2 gas analysis.
5. After using Q-65 as an asphaltene model molecule, study the effect of nanosize on original visbroken residue n-C_5 asphaltenes adsorptive removal and post-adsorption catalytic oxidation. Apply the Solid–Liquid Equilibrium (SLE) adsorption model to describe the behavior of the adsorption affinity and asphaltene aggregates.
6. Apply Kissinger-Akahira-Sunose (KAS) kinetics method to describe the effect of the nanosize on the oxidation mechanism and the reaction pathway. Consequently, estimate the transitional thermodynamic parameters of the oxidation reactions.

1.3 Thesis organization

This thesis consists of five chapters of a collection of three journal papers, one of which has already been published and the remaining ones are in the process of getting published. The first author, Nedal Marei, performed most of the experimental work and data analysis, and participated in interpreting the results and core part of writing. Nashaat Nassar is the Principal Investigator (PI), supervisor and the corresponding author. Gerardo Vitale helped in preparing and characterizing the nanoparticles as well as computational modeling performing and critical revision for the articles. Amjad El-Qanni contributed with modeling the asphaltene adsorption isotherms and FTIR data analysis. Maryam Hmoudah contributed with performing the kinetics modeling and data analysis. Azfar Hassan contributed with TGA-MS setup preparation and interpreting of TGA-MS results.

Chapter 1 provides a brief background, objectives and organization of thesis. A brief introduction has been included in this chapter since each chapter has a detailed introduction related to the subject of the paper.

Chapter 2 investigates the nanosize effect of NiO nanoparticles on the adsorption of Q-65. This chapter was published in the "Physical Chemistry Chemical Physics" (PCCP) journal with the title, "*The effect of the nanosize on surface properties of NiO nanoparticles for the adsorption of Quinolin-65*" (Marei et al., 2016a).

Chapter 3 studies the effect of nanosize of NiO nanoparticles on catalytic thermo-oxidative decomposition of adsorbed Q-65 using TGA/DTA and TGA-MS systems in a paper entitled "*Catalytic effect of nanosized NiO nanoparticles in thermo-oxidative decomposition of Quinolin-65"* (Marei et al., 2016b).

Chapter 4 demonstrates the nanosize effect of NiO nanoparticles on adsorption and post-adsorption catalytic oxidation of visbroken residue n-C_5 asphaltenes using thermogravimetric analyzer coupled with mass spectrometer. The title of this journal paper is "*Nanosize effects on NiO nanoparticles for adsorption and subsequent thermo-oxidative decomposition of visbroken residue asphaltenes"* (Marei et al., 2016c).

Finally, **Chapter 5** concludes this research and delivers recommendations for future studies. It should be noted that the present thesis is in part based on refereed papers that have already been published or are in their latest stages for publication. Necessarily, there will be some repetitions between the chapters particularly in the introduction part or in the sections to introduce the experimental procedure, materials and analysis.

References

AKBARZADEH, K., HAMMAMI, A., KHARRAT, A., ZHANG, D., ALLENSON, S., CREEK, J., KABIR, S., JAMALUDDIN, A. J., MARSHALL, A. G., RODGERS, R. P., MULLINS, O. C. & SOLBAKKEN, T. 2007. Asphaltenes-problematic but rich in potential. oilfield review, 22-43.

ALBERTA ENERGY. 2016. Oil Sands [Online]. Government of Alberta. Available: http://www.energy.alberta.ca/oilsands/oilsands.asp [Accessed March 14, 2016].

BRITISH PETROLEUM. 2016. What drives energy demand? [Online]. Available: http://www.bp.com/en/global/corporate/energy-economics/energy-outlook-2035/drivers-of-energy-demand.html [Accessed March 14, 2016].

CHIANELLI, R. R., SIADATI, M., MEHTA, A., POPLE, J., ORTEGA, L. C. & CHIANG, L. Y. 2007. Self-assembly of asphaltene aggregates: synchrotron, simulation and chemical modeling techniques applied to problems in the structure and reactivity of asphaltenes. In: MULLINS, O. C., SHEU, E. Y., HAMMAMI, A. & MARSHALL, A. G. (eds.) Asphaltenes, Heavy Oils, and Petroleomics. New York, NY: Springer New York.

COYNE, T. 2016. Is This The End Of The U.S. Oil Boom? Alberta Oil: The business of Energy. Alberta, Canada: Venture Publishing Inc.

DEVARD, A., PUJRO, R., DE LA PUENTE, G. & SEDRAN, U. 2012. Hydrocarbon yield structure in the conversion of heavy model molecules (quinolin-65) on fluidized catalytic cracking catalysts. Energy & Fuels, 26, 5015-5019.

FRANCO, C., PATIÑO, E., BENJUMEA, P., RUIZ, M. A. & CORTÉS, F. B. 2013a. Kinetic and thermodynamic equilibrium of asphaltenes sorption onto nanoparticles of nickel oxide supported on nanoparticulated alumina. Fuel, 105, 408-414.

FRANCO, C. A., MONTOYA, T., NASSAR, N. N., PEREIRA-ALMAO, P. & CORTÉS, F. B. 2013b. Adsorption and subsequent oxidation of Colombian asphaltenes onto nickel and/or palladium oxide supported on fumed silica nanoparticles. Energy & Fuels, 27, 7336-7347.

FRANCO, C. A., NASSAR, N. N., MONTOYA, T. & CORTÉS, F. B. 2014. NiO and PdO supported on fumed silica nanoparticles for adsorption and catalytic steam gasification of Colombian c_7-asphaltenes. In: AMBROSIO, J. (ed.) Handbook on Oil Production Research. Hauppauge, N.Y. USA: Nova Science Publishers, Inc.

GOVERNMENT OF ALBERTA 2009. Environmental Management of Alberta's Oilsands.

HASHMI, S. M., ZHONG, K. X. & FIROOZABADI, A. 2012. Acid-base chemistry enables reversible colloid-to-solution transition of asphaltenes in non-polar systems. Soft Matter, 8, 8778-8785.

HASSAN, A., LOPEZ-LINARES, F., NASSAR, N. N., CARBOGNANI-ARAMBARRI, L. & PEREIRA-ALMAO, P. 2013. Development of a support for a NiO catalyst for selective adsorption and post-adsorption catalytic steam gasification of thermally converted asphaltenes. Catalysis Today, 207, 112-118.

KRISTOPHER, G. 2016. Crude Oil Prices Fell by 17% in the Last 6 Trading Sessions [Online]. Market Realist. Available: http://marketrealist.com/2016/01/war-words-opec nations-crude-oil-market [Accessed March 10, 2016].

LÓPEZ-LINARES, F., CARBOGNANI, L., GONZÁLEZ, M. F., SOSA-STULL, C., FIGUERAS, M. & PEREIRA-ALMAO, P. 2006. Quinolin-65 and Violanthrone-79 as model molecules for the kinetics of the adsorption of C_7 athabasca asphaltene on macroporous solid surfaces. Energy & Fuels, 20, 2748-2750.

MAREI, N. N., NASSAR, N. N. & VITALE, G. 2016a. The effect of the nanosize on surface properties of NiO nanoparticles for the adsorption of Quinolin-65. Physical Chemistry Chemical Physics, 18, 6839-49.

MAREI, N. N., NASSAR, N. N., VITALE, G. & HASSAN, A. 2016b. Catalytic effect of nanosized NiO nanoparticles in thermo-oxidative decomposition of Quinolin-65. Submitted to Catalysis Science & Technology Journal, RSC.

MAREI, N. N., NASSAR, N. N., HOMUDAH, M., EL-QANNI, A., VITALE, G. & HASSAN, A. 2016c. Nanosize Effects on NiO nanoparticles for adsorption and subsequent thermo-oxidative decomposition of visbroken residue asphaltenes. Submitted to Fuel, Elsevier.

NASSAR, N. N., HASSAN, A. & PEREIRA-ALMAO, P. 2011a. Application of nanotechnology for heavy oil upgrading: catalytic steam gasification/cracking of asphaltenes. Energy & Fuels, 25, 1566-1570.

NASSAR, N. N., HASSAN, A. & PEREIRA-ALMAO, P. 2011b. Comparative oxidation of adsorbed asphaltenes onto transition metal oxide nanoparticles. Colloids and Surfaces A: Physicochemical and Engineering Aspects, 384, 145-149.

NASSAR, N. N., HASSAN, A. & PEREIRA-ALMAO, P. 2011c. Metal oxide nanoparticles for asphaltene adsorption and oxidation. Energy & Fuels, 25, 1017-1023.

NASSAR, N. N., HASSAN, A. & PEREIRA-ALMAO, P. 2013. Clarifying the catalytic role of NiO nanoparticles in the oxidation of asphaltenes. Applied Catalysis A: General, 462–463, 116-120.

NASSAR, N. N., HASSAN, A. & VITALE, G. 2014. Comparing kinetics and mechanism of adsorption and thermo-oxidative decomposition of Athabasca asphaltenes onto TiO_2, ZrO_2, and CeO_2 nanoparticles. Applied Catalysis A: General, 484, 161-171.

NATIONAL ENERGY BOARD 2016. Estimated production of canadian crude oil and equivalent.

OIL SANDS REVIEW 2016. Alberta oil sands industry quarterly | Winter 2016.

CHAPTER TWO: THE EFFECT OF THE NANOSIZE ON SURFACE PROPERTIES OF NiO NANOPARTICLES FOR THE ADSORPTION OF QUINOLIN-65

This Chapter is adapted from the following publication, after permission:

MAREI, N. N., NASSAR, N. N. & VITALE, G. 2016. The effect of the nanosize on surface properties of NiO nanoparticles for the adsorption of Quinolin-65. Physical Chemistry Chemical Physics, 18, 6839-6849.

2.1 Abstract

Using Quinolin-65 (Q-65) as a model-adsorbing compound for polar heavy hydrocarbons, the nanosize effect of NiO nanoparticles on adsorption of Q-65 was investigated. Different-sized NiO nanoparticles with sizes between 5 and 80 nm were prepared by controlled thermal dehydroxylation of $Ni(OH)_2$. The properties of the nanoparticles were characterized by XRD, BET, FTIR, HRTEM and TGA. The effects of the nanosize on the textural properties, shape and morphology were studied. The adsorption of Q-65 molecules onto different-sized nanoparticles was tested in toluene-based solutions. On a normalized surface area basis, the number of Q-65 molecules adsorbed per nm^2 of NiO surface was the highest for NiO nanoparticles of size 80 nm; while 5 nm size NiO nanoparticles was the lowest. Excitingly, the adsorption capacity of other NiO sizes varied from loading suggesting different adsorption behavior, which exhibits the significance of textural properties during adsorption of Q-65. Computational modeling of the interaction between the Q-65 molecule and NiO nanoparticle surface was carried out to get more understanding of its adsorption behavior. A number of factors contributing to the enhanced adsorption capacity of nanoscale NiO were determined. These include surface reactivity, topology, morphology and textural properties.

2.2 Introduction

Metal-based nanoparticles are emerging as a promising alternative for enhancing heavy oil upgrading and recovery and inhibition of formation damage (Hashemi et al., 2014), through the development of more efficient yet environmentally friendly processes with economical approaches (Nassar et al., 2011b, Adams, 2014, Nassar et al., 2012), Because of the 'non-bulk' physical and chemical properties of nanoparticles, nanoparticle surface morphology, structure and reactivity may play roles in different oil and gas processes, such as adsorption and catalysis (El-Qanni et al., 2016, Auffan et al., 2009, Jang et al., 2001, Yean et al., 2005). Actually, the interactions of nanoparticles with polar heavy hydrocarbon molecules have shown to play an important role in their subsequent processing such as adsorption (Adams, 2014, Nassar et al., 2011b), post-adsorption thermo-oxidative decomposition (Nassar et al., 2012, Hashemi et al., 2013), catalytic steam gasification (Hassan et al., 2015, Nassar et al., 2011a) and enhanced oil upgrading and recovery (Hashemi et al., 2013). Although there is a great deal of interest in the use of nanoparticles as adsorbents and catalysts for enhancing crude oil upgrading and recovery, stabilization of asphaltenes and inhibition of formation damage, the effect of nanoparticle size on their adsorptive and catalytic behavior towards polar heavy hydrocarbons is still unclear. Nanoparticle, defined as a particle that has a characteristic dimension between 1 and 100 nm and has unique properties that are different than the bulk particles with the same chemical composition (Auffan et al., 2009). We believe here that, despite this broadly accepted definition, within the specified size range of 1 to 100 nm, nanoparticle may undergo dramatic changes in surface properties, topology, morphology and textural properties which consequently impact its surface and interfacial reactivity. The central question here is this: do nanoparticles of size close to 100 nm behave similarly to the particle of size close to 1 nm, with the same chemical composition?

In this study we focus here on metal-based nanoparticles for which there is substantial interest in their application in oil and gas industry (Zhang et al., 2014, Bykova et al., 2012, Xu et al., 2003, Song, 2006, Liao et al., 2015). The objective of our study is to investigate the surface characteristics of NiO nanoparticles, which are typically used as adsorbents and catalysts in enhanced heavy oil upgrading and recovery processes (Hosseinpour et al., 2013, Kazemzadeh et al., 2015, Nassar et al., 2011b, Liu et al., 2015, Franco et al., 2013). The work aims to investigate the changes in NiO nanosizes and their effects on the properties of the particles itself, including; shape, topology, porosity and surface area. The NiO nanosize effect is demonstrated on the adsorption of model-adsorbing compound for polar heavy hydrocarbons (Quinolin-65), which has shown to be a good model for representing adsorption of asphaltenes (López-Linares et al., 2006, Nassar et al., 2014). This study provides new understandings on the nanosizes, at the range of 5 to 80 nm, and their effect on the adsorption of heavy hydrocarbons, it also may have important effects on the preparation of advanced nanostructured catalysts and other chemical materials.

2.3 Experimental Section

2.3.1 Materials

A model asphaltene molecule, Quinolin-65 (Q-65) ($C_{30}H_{29}NO_2S$, MW = 467.62 g.mol^{-1}, λ_{max} = 375 nm, dye content 80%) purchased from Sigma-Aldrich, Ontario, was used as an adsorbate and model asphaltene molecule. Figure1 shows the chemical structure of Q-65, as drawn with ChemDraw V14 (Guzmán et al., 2016). From Figure 2.1, it is observed that this model molecule contain molecular characteristics present in asphaltene fractions reported for Athabasca crude oil, like alkyl chains, aromatic moieties and heteroatoms like sulfur, nitrogen and oxygen. This model molecule represents an asphaltene of the continental type due to the presence of one significant

large aromatic area plus side chains per molecule. These facts were confirmed by different authors (Groenzin and Mullins, 2000, López-Linares et al., 2006, Mojelsky et al., 1992, Devard et al., 2012). Toluene HPLC grade obtained from Sigma-Aldrich, Ontario was used as a solvent. $Ni(NO_3)_2.6H_2O$ obtained from Sigma-Aldrich, Ontario and NaOH pellets obtained from VWR, Radnor, were used as precursors for NiO nanoparticles preparation. All chemicals were used as received without further purification.

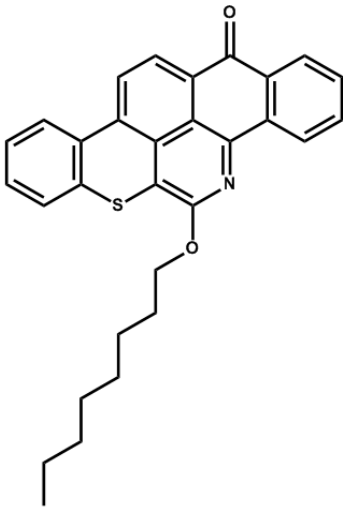

Figure 2.1 Q-65 molecular structure drawn with ChemDraw V14 (Guzmán et al., 2016). The resemblance with a asphaltene molecule can be seen by the archipielago aromatic region, the alkyl chain and the presence of heteroatoms like sulfur, nitrogen and oxygen.

2.3.2 NiO nanoparticles

Controlled thermal dehydroxylation of $Ni(OH)_2$ was used to prepare different sizes of NiO nanoparticles in the range of 5 to 80 nm. The first step was the preparation of the $Ni(OH)_2$ precursor under hydrothermal synthesis conditions. 19.47 g of nickel nitrate ($Ni(NO_3)_2.6H_2O$) was dissolved in deionized water and, after complete dissolution of the nickel salt, NaOH pellets were added pellet by pellet under magnetic stirring until a pH of 11 was reached to precipitate small nickel hydroxide particles ($Ni(OH)_2$). The final slurry mixture was homogenized for 15 min, and then

transferred to a polypropylene bottle that was sealed properly to avoid loss of water by evaporation. Then, the slurry was crystallized for 4 h at 373 K in an oven. After crystallization, the product was filtered, washed with distilled water and dried for 12 h at 373 K. The dried material was then calcinied with a ramp of 5 K/min for 2-3 h at different temperatures in the range of 573 to 973 K to get NiO nanoparticles by controlled dihydroxylation of $Ni(OH)_2$ with average crystalline domain sizes from 5 to 80 nm. The nanoparticle crystalline domain sizes increased with increasing the calcination temperature and time.

2.3.3 Characterization of the prepared NiO nanoparticles

2.3.3.1 X-ray diffraction

Dried powders of nanoparticles were characterized by X-ray diffraction using a Rigaku ULTIMA III X-ray diffractometer with Cu Kα radiation as the X-ray source. The scan was performed in the range 30–90º 2θ using a 0.02º step and a counting time of 1º/min. The crystalline domain sizes were measured using the Debye-Scherrer equation as implemented in the commercial software JADE(Nassar et al., 2015) (provided with the diffractometer), by calculating the full width at half-maximum (FWHM) of the peaks fitting the experimental profile to a pseudo-Voigt profile function.

2.3.3.2 Textural properties

The surface areas of the prepared nanoparticles were estimated following the Brunauer-Emmett-Teller (BET) method. This was achieved by performing nitrogen physisorption at 77 K, using a Micromeretics Tristar 3000 surface area analyzer, Norcross, GA. The samples were degassed at 423 K under N_2 flow overnight before analysis. An estimation of the particle size (assuming

spherical particles) was achieved by using the measured BET area as per eq (2.1) (Nassar et al., 2014)

$$d = \frac{6000}{\mathrm{SA} \times \rho_{NiO}} \qquad (2.1)$$

where d is the particle size in nm, SA is the experimentally measured specific surface area (m^2/g), and ρ_{NiO} is the NiO density (6.67 g/cm^3).

2.3.3.3 High resolution transmission electron microscopy (HRTEM)

High resolution transmission electron microscopy (HRTEM) was performed for the analysis of nanoparticle size, morphology and crystallinity. Around 0.5 mg of NiO nanoparticle sample was dispersed in 1 ml pure ethanol and sonicated for approximately 5 min. For analysis, a drop of this dispersion solution was deposited onto a Formvar/carbon copper grid sample holder. The drop was then allowed to dry depositing NiO nanoparticles on the grid holder. Observations were carried out using a FEI Tecnai F20 FEG TEM with an accelerating voltage of 200 kV.

2.3.3.4 Infrared analysis

Infrared spectroscopy was performed to study the framework infrared region of the NiO nanoparticles and identify the molecular bonds and functional groups. Approximately 5 mg of nanoparticles was mixed with 500 mg of KBr and the entire mixture was mounted in the DRIFTS sample holder. Analysis was carried out using a Nicolet 6700 FTIR instrument manufactured by Thermo Electron Corporation with a smart diffuse reflectance attachment to carry out DRIFTS (diffuse reflectance infrared Fourier transform spectroscopy). The obtained spectra were the

average of 128 scans that were taken for each sample in a range from 400 to 4000 cm^{-1} with a resolution of 2 cm^{-1}.

2.3.3.5 TGA analysis

Thermogravimetric analysis (TGA) was carried out to identify the hydroxyl group density on the surface of NiO nanoparticles. Approximately 4 mg of NiO nanoparticles were heated from 20 to 800 ºC in a thermogravimetric analysis/differential scanning calorimetry (TGA/DSC) analyzer (SDT Q600, TA Instruments, Inc., New Castle, DE) at an air flow rate of 100 cm^3/min and heating rate of 10 °C/min. The TGA instrument was calibrated for mass and heat changes using sapphire as a reference for heat calibration and zinc as a reference for temperature calibration. The surface hydroxyl groups density, σ (#OH/nm^2), of the NiO nanoparticles was calculated using the TGA weight loss between 400 to 800 ºC as follows (Ma, 2003, Mueller et al., 2003):

$$\sigma = 2\frac{W_C/MW}{W_{NP}SA}N_A \qquad (2.2)$$

where W_C is the weight loss (g) from 400-800 °C, W_{NP} is the initial weight of the NiO nanoparticle sample (g), SA is the BET surface area of each NiO nanoparticles (nm^2), the coefficient 2 is employed here since each two hydroxyl group start to condensate above 400 °C to produce a water molecule with molecular weight (MW) of 18.01528 (g/mol), and N_A is the Avogadro's constant.

2.3.4 Adsorption experiments

Batch adsorption experiments were carried out by exposing 100 mg of each specific NiO nanosize (5 to 80 nm) to a set of tightly sealed 25 mL vials containing final volume of 10 mL solution of Q-65 dissolved in toluene with different initial concentrations ranging from 0 to 0.86 mmol/L at 293 K. The stirring speed was kept constant at 200 rpm for all samples. Samples for

analysis were collected after 24 h adsorption, by allowing the nanoparticles containing the adsorbed Q-65 to settle and decanting the supernatant. Some experiments were performed by triplicate, and the standard deviations were calculated and presented. The residual Q-65 concentration in the supernatant was measured using UV-vis spectrophotometry (Evolution 260 Bio UV-Vis spectrophotometer, Thermo Scientific, USA) using a wavelength (λ_{max}) of 375 nm. A calibration curve of the UV−vis absorbance at 375 nm against the Q-65 concentration was established using standard model solutions with known concentrations prepared in-house. UV−vis spectra of the Q-65 solutions were selected based on the absorption linearity range (absorbance < 4.0). The adsorbed amount of Q-65 (molecule of Q-65/nm^2 of nanoparticles) was calculated as shown in eq (2.3)

$$Q = \frac{(C_o - C_e)N_A}{SA} V \qquad (2.3)$$

where C_o is the initial concentration of Q-65 in solution (mmol/L), C_e is the equilibrium concentration of Q-65 in the supernatant (mmol/L), V is the solution volume (L), and SA is the BET surface area of NiO nanoparticles (nm^2), N_A is the Avogadro's constant.

2.4 Computational modeling of the interaction of Q-65 molecules with NiO nanoparticles

Computational modeling was carried out to get some insights into the adsorption interaction of the Q-65 molecules with the surfaces of different sizes of NiO nanoparticles. NiO has the rock salt structure (similar to MgO, CaO, CoO and many other binary oxides) and it is of interest because of its relevance to gas sensors, electrochromic coatings, catalysis, and more recently to adsorptive removal of heavy polar hydrocarbons (Nassar et al., 2014, Hashemi et al., 2014, Hassan et al., 2013). NiO surfaces have been investigated by computer simulation focusing particularly on low

index planes including non-polar and polar surfaces (Mulheran, 1993, Yan et al., 1995, Taylor et al., 1999, Oliver et al., 1995, Barbier et al., 2000, Wander et al., 2003, Fisher, 2004).

Starting from the experimental structural data of NiO within BIOVIA Material Studio Database (Jørgensen et al., 2007) we created two model of nanoparticles based on the HRTEM images: (a) spherical-like and (b) tablet-like NiO nanoparticles, with similar dimension as those obtained experimentally, to carried out our studies of the Q-65 interaction with these nanoparticles. For our computational studies, we used the modules Forcite and Adsorption Locator included within the commercial modelling software BIOVIA Materials Studio V7.0 (BIOVIA, 2014). BIOVIA Forcite is an advanced classical molecular mechanics tool, designed to work with a wide range of forcefields, allowing fast energy calculations and reliable geometry optimizations of molecules and periodic systems. In our study, BIOVIA Discover module was also used to calculate infrared vibration modes for the NiO structure and BIOVIA Forcite was used to geometrically optimize the Q-65 molecule, to optimize the NiO unit cell and to relax the surface atoms of the created NiO nanoparticle prior to their use on the adsorption study. For the later task, we used BIOVIA Adsorption Location module which is based on simulated annealing (a metaheuristic algorithm for locating a good approximation to the global minimum of a given function in a large search space) (Kirkpatrick et al., 1983, Černý, 1985). Allowing in this way identification of the possible adsorption configurations by carrying out Monte Carlo searches of the configurational space of the nanoparticle of NiO-Q-65 system as the temperature is slowly decreased. To identify additional local energy minima, the process is repeated several times.

Atomistic simulations of inorganic-organic interfaces require accurate description of interatomic forces, and thus, in the present study we employed BIOVIA COMPASS forcefield as it can simulate not only organic molecules but also bulk metal oxides and interfaces between metal

oxides and organic molecules (2014, Zhao et al., 2007). The powerful COMPASS (Condensed-phase Optimized Molecular Potentials for Atomistic Simulation Studies) forcefield has been parameterized and validated by using condensed-phase properties in addition to various *ab initio* and empirical data for molecules in isolation enabling it to accurately and simultaneously make predictions of structural, conformational, vibrational, and thermophysical properties that exit for a broad range of organic and inorganic molecules in isolation and in condensed phases including interfaces and mixtures (Zhao et al., 2007, McQuaid et al., 2004). Currently, the coverage of this forcefield includes the most common organics, inorganic small molecules, polymers, some metal ions, metal oxides, and metals (BIOVIA, 2014).

2.4.1 Q-65 molecule

Q-65 molecule was built and optimized with BIOVIA Forcite before adsorbing it onto NiO nanoparticles. The quality of the Geometry Optimization in BIOVIA Forcite was set to Fine and the Forcefield to BIOVIA COMPASS as this forcefield is compatible with metal oxides (Kirkpatrick et al., 1983) and is used to study the interaction of Q-65 with NiO. The optimized Q-65 molecule is presented in Figure 2.2, where an almost flat configuration of the molecule can be noticed.

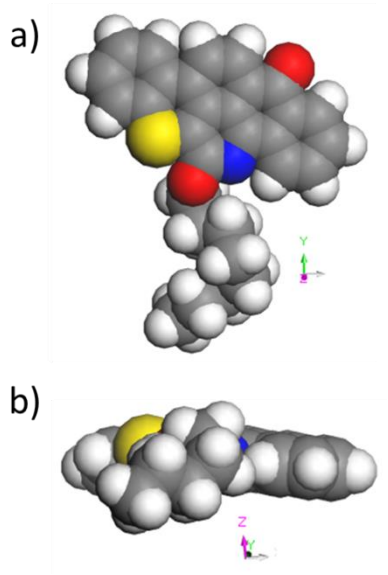

Figure 2.2 CPK representation of the optimized Q-65 molecule showing its optimized configuration (top and side views, respectively). Grey atoms represent carbon, blue atoms represent nitrogen, white atoms represent hydrogen, yellow atoms represent sulfur and red atoms represent oxygen.

2.4.2 NiO nanoparticles

The experimental structural data for NiO reported in the BIOVIA Materials Studio structural database(BIOVIA, 2014) was transferred to BIOVIA Materials Studio Builder module and the unit cell was geometrically optimized within BIOVIA Forcite. The quality of the Geometry Optimization in BIOVIA Forcite was set to Fine and the Forcefield to BIOVIA COMPASS as this forcefield is compatible with organic molecules, and thus, suitable for studying the interaction of molecules with the NiO surfaces (Zhao et al., 2007). The experimental unit cell value for NiO is 0.41684 nm(BIOVIA, 2014) and the optimized unit cell value obtained with Forcite and the COMPASS forcefield was 0.41680 nm which is very similar to the experimental one indicating the quality and the reliability of the employed forcefield. The optimized unit cell was then used within BIOVIA Builder module to create two nanoparticles from the optimized structural data

using BIOVIA nanostructure builder. The first one was a 5 nm spherical nanoparticle, for this case the internal coordinate atoms in this nanoparticle were fixed to their bulk values and the top layers of atoms (~0.5 nm) which will interact with the Q-65 molecule were allowed to relax under the geometric optimization carried out with BIOVIA Forcite with the BIOVIA COMPASS forcefield which has been parametrized for metal oxides and which is suitable to study interfaces between organics and inorganics (BIOVIA, 2014, Zhao et al., 2007) Figure 2.3 shows the surface relaxed of 5 nm NiO nanosphere. Three facet orientations can be observed in the nanosphere model shown in Figure 2.3a, the indices of these facets are the {100} , the {110} and the {111} which indicates there are three clear different possible surfaces for adsorption of the Q-65 molecule in the spherical nanoparticle.

The second model was a nanotablet with dimensions 3×5×15 nm and again the top layer of atoms (~0.5 nm) were allowed to relax while the internal atoms were constrained to their bulk values and the geometric optimization was carried out with BIOVIA Forcite with the BIOVIA COMPASS forcefield. Figure 2.3b shows the surface relaxed NiO nanotablet. For the case of the nanotablet, only the {100} facets are observed, and thus, only one type of surface orientation is available for the adsorption of Q-65 molecules.

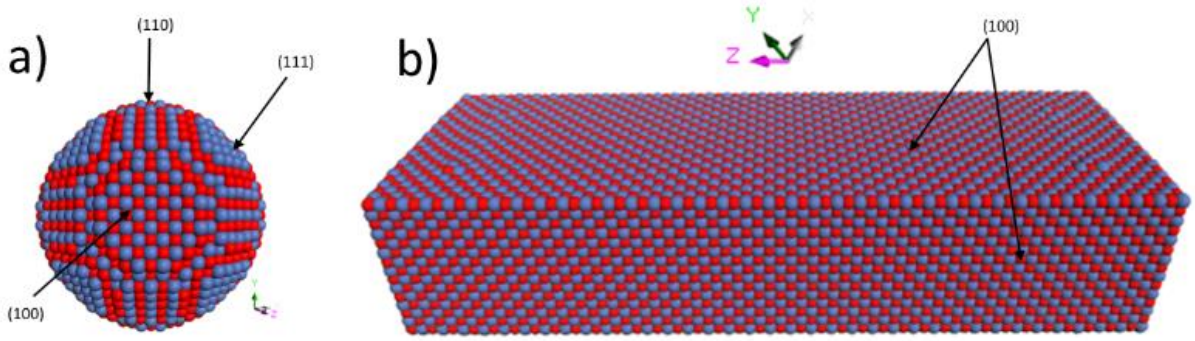

Figure 2.3 CPK representation, with a 45 degree perspective, of the surface relaxed NiO nanoparticles. (a) 5 nm NiO nanosphere and (b) 3×5×15 nm NiO nanotablet. Blue atoms represent nickel and red atoms represent oxygen.

2.4.3 Interaction of Q-65 molecule with NiO nanoparticles

BIOVIA Adsorption locator module was used to gain insights into the interaction of Q-65 molecule with the surfaces of the spherical- and tablet-like nanoparticles built before, which are more representative of the actual used nanoparticles (HRTEM images). The simulating annealing task in BIOVIA Adsorption Locator calculation was set to a quality of Fine (energy cutoff of 1.0 $\times 10^{-4}$ kcal/mol) using the Smart algorithm. The atom based summation method was used for the electrostatic and van der Waals with a cubic spline truncation and a cutoff distance of 1.55 nm. The forcefield selected was BIOVIA COMPASS, which is suitable to study interfaces between organics and inorganics (BIOVIA, 2014, Zhao et al., 2007) The top layer atoms (~0.5 nm) in the spherical and the tablet-like nanoparticle surfaces were selected for the interaction with Q-65 molecules, and the maximum adsorption distance value was 1.5 nm with a fixed energy window of 10 kcal/mol for sampling configurations which differ from the lowest configuration in that maximum amount. Several tests were carried out, one with loading a single Q-65 molecule and others with loading several Q-65 molecules on each nanoparticle surface.

2.5 Results and Discussion

2.5.1 Characterization studies

2.5.1.1 X-ray diffraction

X-ray diffraction analysis of the different sizes nanoparticles (Figure 2.4) confirmed that the correct structure was NiO, as all the XRD patterns match very well with the diffraction peaks of the NiO structure identified in the JADE program, using the database of Materials Data XRD Pattern Processing Identification & Quantification (PDF#01-075-0269). This indicates the preparation of pure NiO nanoparticles. Diffraction peaks around 37.2°, 43.3°, 62.9°, 75.39°, and 79.4° can be indexed as diffraction from (111), (200), (220), (311), and (222) planes of NiO with cubic structure, respectively. As seen, the peaks are very broad indicating that the prepared nanoparticles have indeed very small crystalline domain sizes (the domain sizes range from 5 to ~80 nm). In addition, the intensity and sharpness of the diffraction peaks were significantly increased as the nanosize of the particle increased. The crystalline domain sizes of the nanoparticles derived from the different diffraction planes using the Debye-Scherrer equation are shown in Table 2.1.

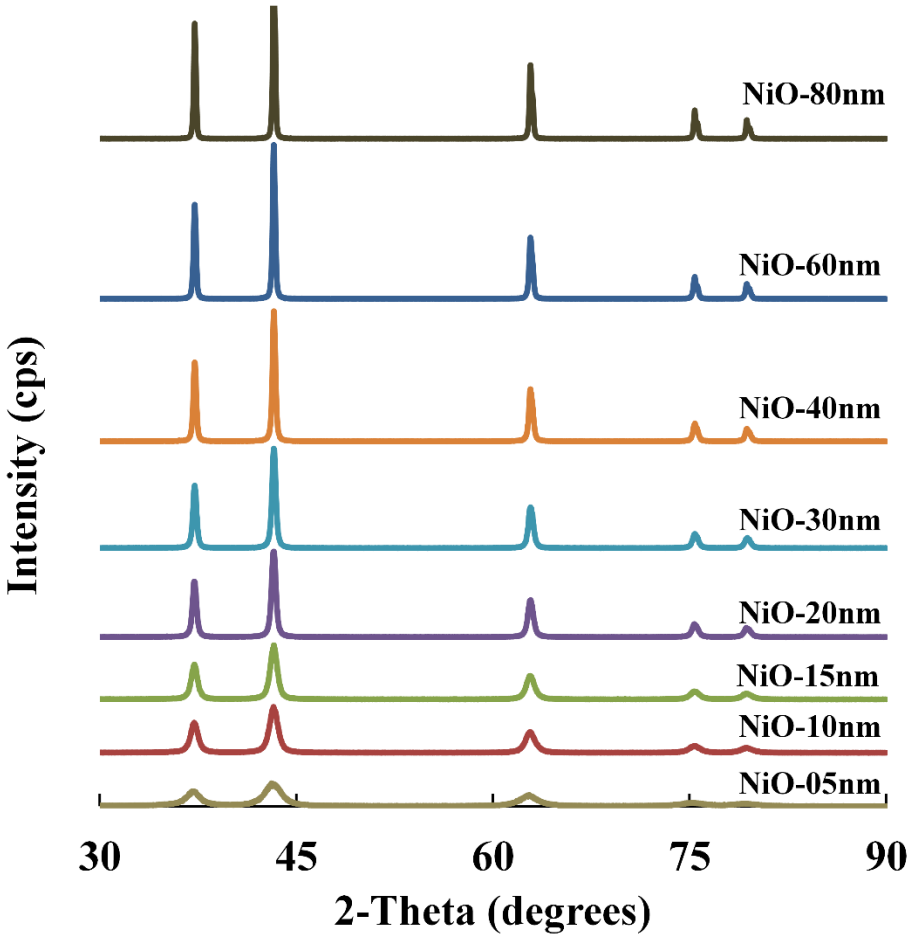

Figure 2.4 X-ray diffraction powder patterns in the region 30–90º of the prepared NiO nanoparticles at diameter size of 5, 10, 15, 20, 30, 40, 60 and 80 nm.

Table 2.1 NiO nanosizes calcination temperature and time, XRD crystalline size, BET surface areas and surface hydroxyl density results.

Calcination temperature (K)		573	673	723	773	823	873	873	973
Calcination time h		2	2	2	2	2	2	3	2
Nominal NiO size (nm)		5	10	15	20	30	40	60	80
X-ray Diffraction planes	**111**	5	12	15	26	30	43	58	84
	200	5	11	15	25	30	45	63	98
	220	5	10	12	22	26	38	52	73
	311	4	10	12	22	25	36	54	75
	222	4	9	12	21	24	35	48	64
Average crystalline domain size (nm)		5	10	13	23	27	39	55	78
Standard Deviation		0.5	1	2	2	3	4	6	13
Measured BET area (m^2/g)		158	58	42	20	17	11	7	3
Expected particle size by BET (nm) (by equation 1)		6	16	21	45	53	82	129	300
Surface hydroxyl density σ (#OH/nm^2)		8.5	6.3	6.0	6.3	5.9	1.8	1.9	1.1

2.5.1.2 Textural properties

Table 2.1 lists the used calcination temperatures and times, X-ray crystalline size and BET surface areas of the prepared NiO nanoparticles. As expected, the surface area of the nanoparticle decreased as the NiO nanosize increased. However, the expected surface area value for each nanoparticle, based on the X-ray crystalline domain sizes, is lower when compared to the ones obtained experimentally, suggesting a possibility of particle aggregation. Figure 2.5 shows the nitrogen physisorption isotherms for each nominal size of prepared NiO nanoparticles.

The International Union for Pure and Applied Chemistry (IUPAC) has classified the adsorption-desorption isotherms in six categories (*Types I to VI*) and the possible hysteresis loops in these isotherms in four categories: *Types H1 to H4* (Sing et al., 2008). According to these classifications, *Type IV* isotherm could be the most descriptive in case of all NiO nanosizes as presented in Figure 2.5.

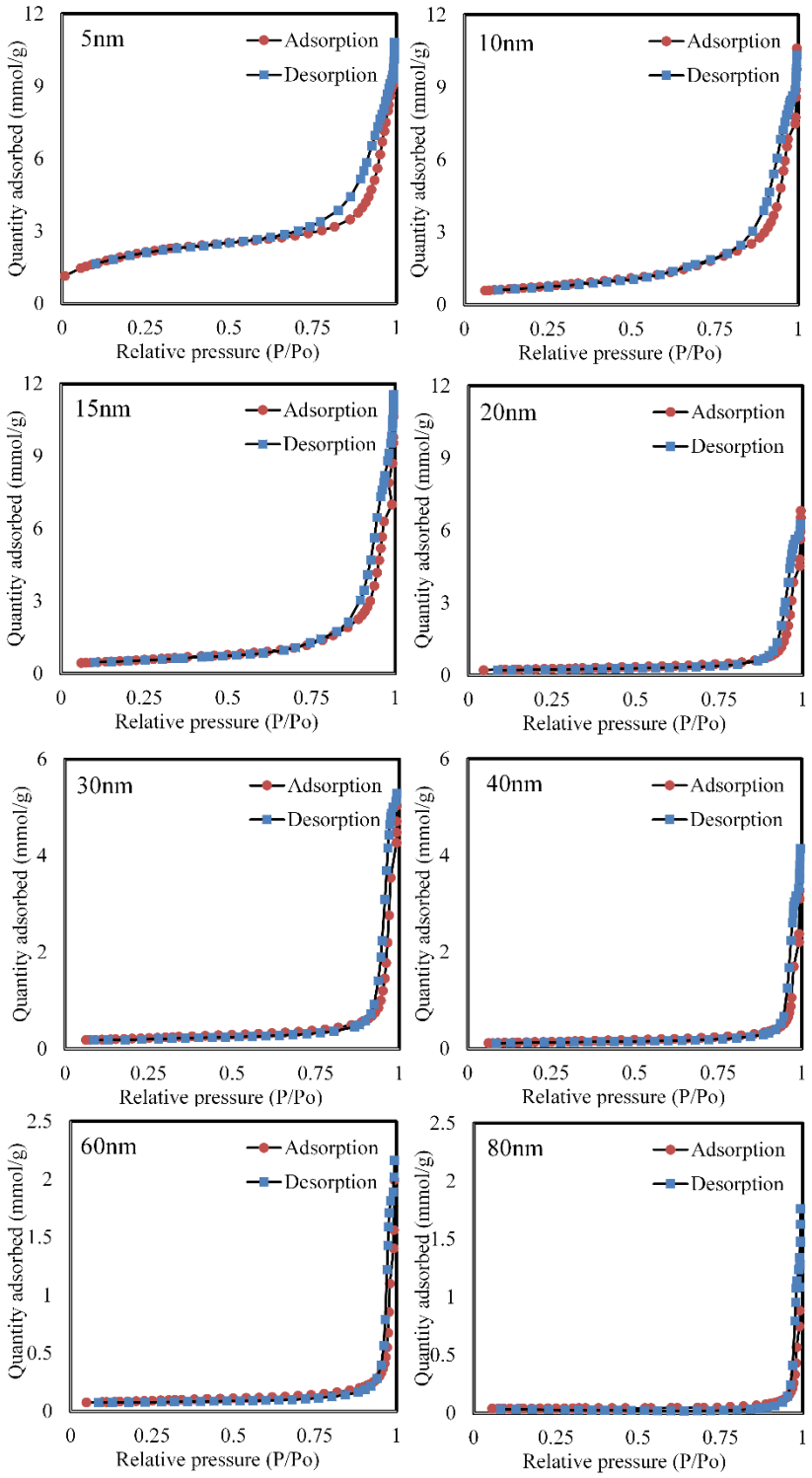

Figure 2.5 Nitrogen adsorption–desorption isotherms for NiO of different Nanosizes (5-80 nm).

It is known that NiO nanoparticle is a non-porous material, and thus, the presence of a hysteresis loop suggests that the small nanosizes are producing interparticle porosity which is observed by the hysteresis loop formation. Then, the real form of the isotherm should be the reversible *Type II* isotherm that is obtained with non-porous or macroporous adsorbents as in the case of NiO, however, the small sizes of the particles generate interparticle cavities of mesoporous sizes that produce capillary condensation which takes place in these mesoporous generated by the interparticle cavities. The *Type H3* loop is the one that best describe the hysteresis loop observed in the isotherms of the prepared NiO nanoparticles. The desorption of N_2 on NiO nanoparticles which does not exhibit any limiting adsorption at high p/p_o is normally observed with aggregates of plate-like particles which gives rise to slit-shaped pores. This feature begins to disappear with increasing the nanosize as there is no significant hysteresis loops in the case of 40, 60 and 80 nm (Figure 2.5). The last observation indicates that the largest particles begin to behave more similar to what is expected for a non-porous bulk NiO material, as the original small particles were fused to form the large ones that do not produce interparticle cavities of mesoporous dimensions (between 2 and 50 nm) only interparticle cavities of macroporous dimension (> 50 nm) which do not form hysteresis loops with N_2 physisorption (Sing, 2009).

2.5.1.3 Size and morphology of different crystal size of NiO

HRTEM was carried out to get insights into the morphology and sizes of the prepared NiO nanoparticles. Figure 2.6 shows HRTEM images of different sizes of NiO nanoparticles. As seen, small nanosizes (like 5, 10 and 15 nm) seem to be connected and aggregated forming rod-like morphology. However, the selected area electron diffraction pattern of these samples (Figure 2.7)

indicate that they are indeed composed of very small crystalline domains as these solids produce circular electron diffraction halos. Clear diffraction dots are observed in the selected area electron diffraction images as the crystalline domains get bigger.

In the case of the 20 and 30 nm size nanoparticle (Figure 2.6) they seem to be formed of flat thin sheets connected to each other, and thus, giving the Type *H3* hysteresis loop observed in the N_2-physisorption isotherms discussed previously. On the other hand, for bigger nanosizes (like 40, 60 and 80 nm), they seem to be formed of more likely sheets with different shapes, while the morphology of the 40 nm sample looks like cylinders, the 60 nm sample are single thicker sheets and the 80 nm sample clearly appear having hexagonal shapes. These observations also help to understand the hysteresis loops and their differences observed in the N_2-physisorption isotherms discussed before.

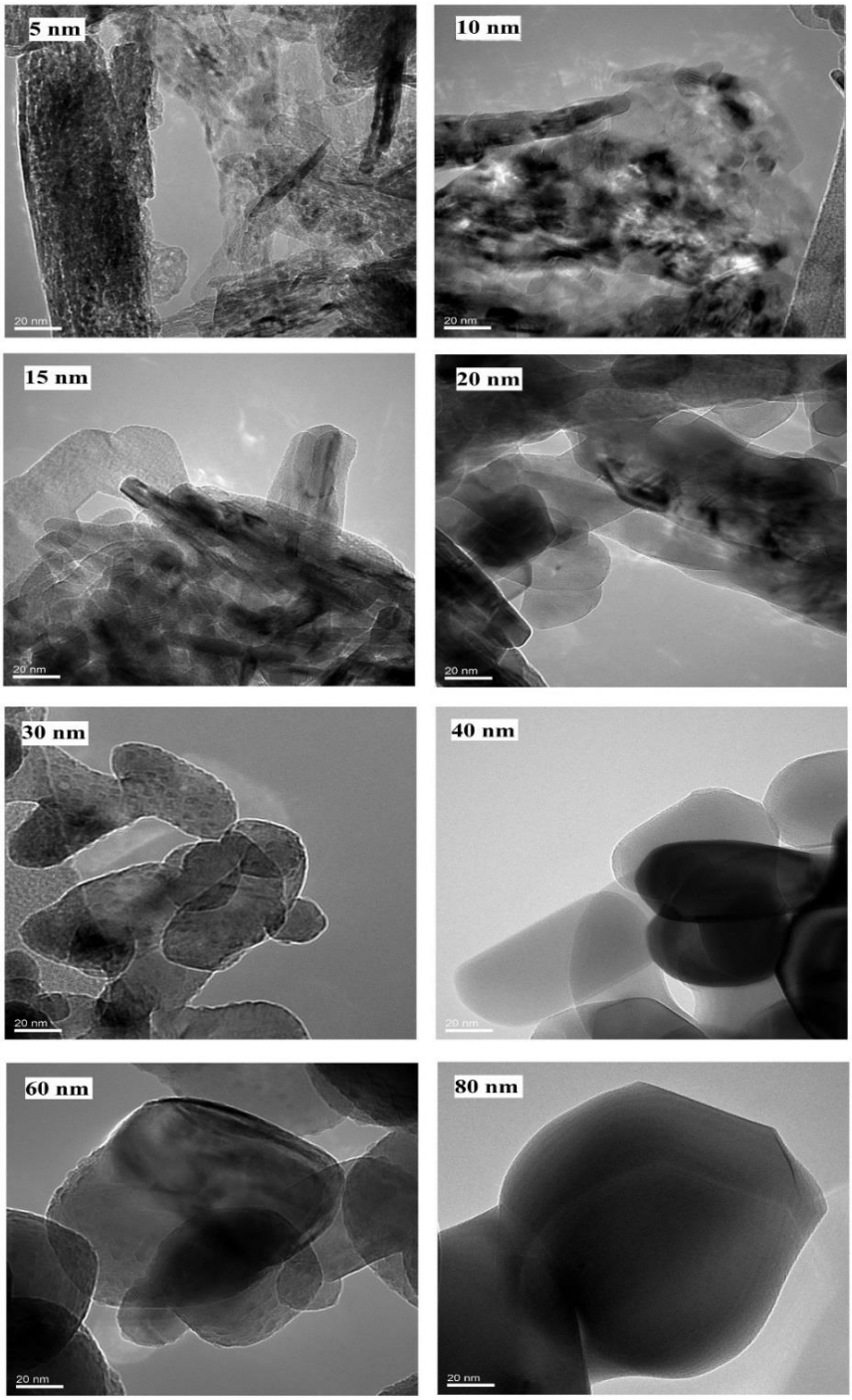

Figure 2.6 HRTEM images of NiO nanoparticles synthesized with nominal sizes from 5 to 80 nm (the scale mark is 20 nm for all the images)

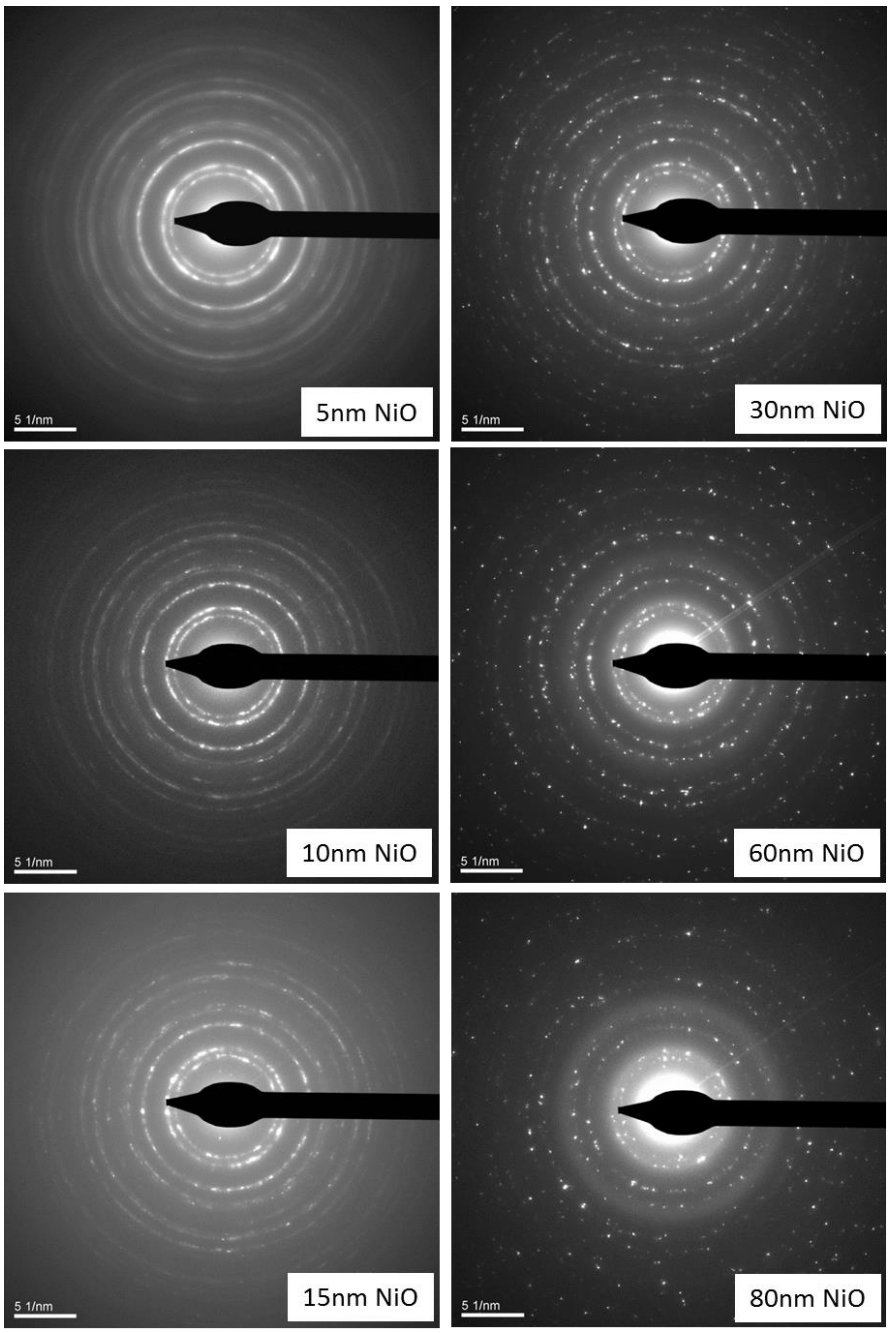

Figure 2.7 Selected Area Electron Diffraction of NiO nanoparticles synthesized with nominal sizes from 5 to 80 nm (the scale mark is 5 nm^{-1} for each image.

2.5.1.4 FTIR analysis

Figure 2.8 shows the FTIR spectra of NiO nanoparticles having different sizes in the framework region (Figure 2.8a) and in the hydroxyl stretching region (Figure 2.8b). The broad absorption band in the region of 400–600 cm^{-1} (framework vibration) is assigned to Ni–O stretching vibration mode; the broadness of the absorption band indicates that the NiO powders are nanocrystals (Biju and Khadar, 2003). Interestingly, it can be observed in Figure 2.8a that as the nanoparticles increase in size from 5 to 80 nm the main peak (centered at around 425 cm^{-1} very similar to the value of 422.7 cm^{-1} calculated with BIOVIA Discover module) becomes broader. This has been observed for NiO nanoparticles with sizes between 4 and 16 nm (Biju and Khadar, 2003). In the smaller nanoparticles, a shoulder around 550 cm^{-1} is observed, but as the nanoparticles increase in size this band becomes more intense, and in the case of the larger nanoparticles the intensity is similar to the band centered at around 425 cm^{-1}. These two bands together produce a broader band which is centered at around 467 cm^{-1}.

Besides the observed Ni–O vibration in Figure 2.8a, it is possible to see a broad band centered around 1400 cm^{-1} that should be assigned to –O–H bending vibrations modes. As expected, the smaller the nanoparticle, the more –OH present on its surface and consequently the larger the bending vibration, as observed for the 5 nm size NiO nanoparticles in Figure 2.8a. In support of this, Figure 2.8a shows the –OH stretching vibration which is more intense in the smaller NiO nanoparticle (5 nm). This high –OH density for the small 5 nm particles should affect their surface interaction with Q-65 molecule.

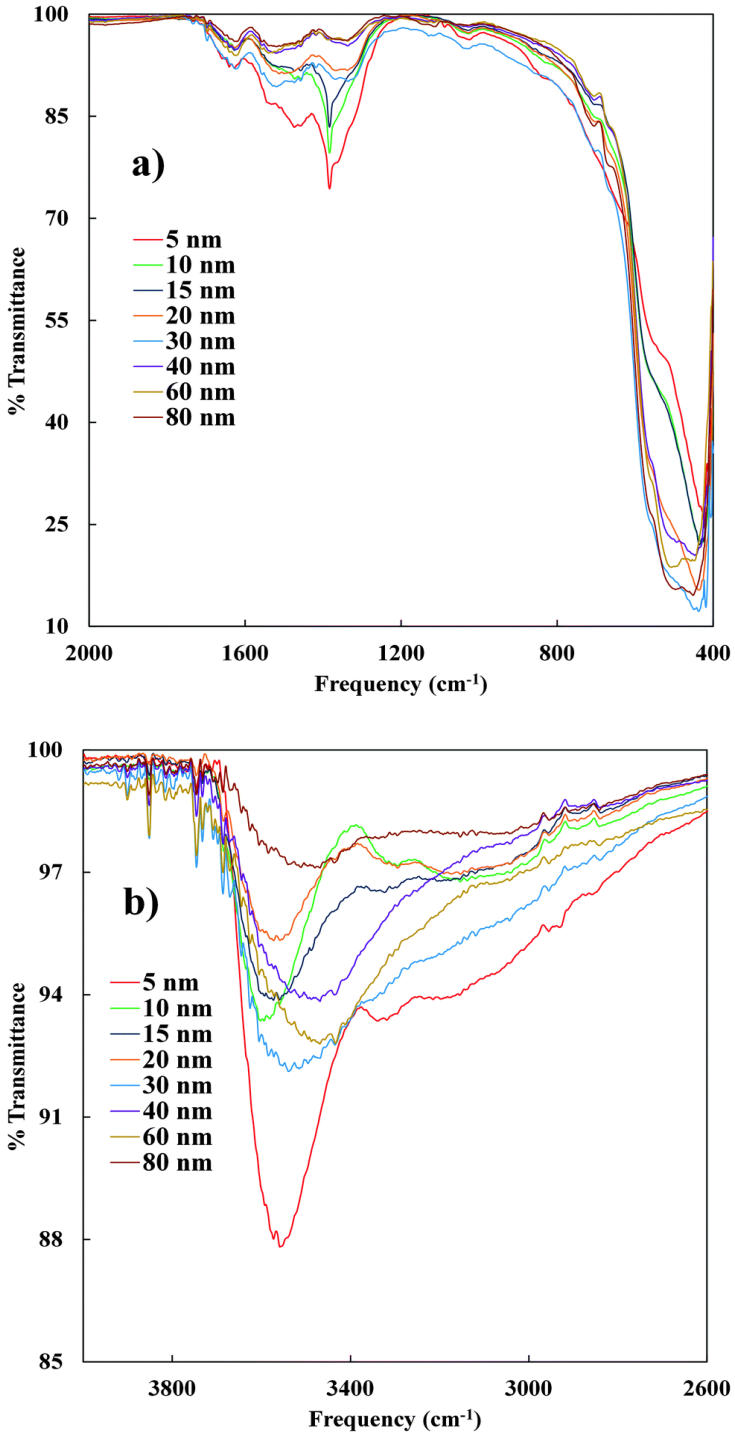

Figure 2.8 FTIR spectroscopy of the NiO nanoparticles 5-80 nm: a) framework region and b) hydroxyl region.

2.5.1.5 Surface hydroxyl density

To estimate the content of hydroxyl group on the surface of each sizes of nanoparticles, thermogravimetric analysis was carried out. Figure 2.9 shows the thermograms for the different sizes of NiO nanoparticles. The TGA curves were divided into three regimes (Ma, 2003, Sheng et al., 2008, Abboud et al., 1997): a) 25 °C to 100 °C, related to gas desorption; b) 100 °C to 400 °C, where the higher mass loss shown here due to the desorption of physically adsorbed water molecules; and c) 400 °C to 800 °C, linked to the dehydroxylation of adjacent –OH groups on the surface and their condensation as a water molecules, as shown in Figure 2.10. The weight loss of each NiO nanosizes, at regime c, was used to calculate the hydroxyl density using eq (2.2) and their values are summarized in Table 2.1. As seen in Figure 2.8b, Figure 2.9 and Table 2.1 the smallest nanoparticles, i.e. 5 nm, portray the highest hydroxyl surface density which was found to be 8.5 OH/nm^2, and this density tends to decrease with increasing the particle size up to 80 nm, having the lowest density value of 1.1 OH/nm^2. The quantitative hydroxyl density obtained for the different sizes of NiO agrees very well with the qualitative FTIR analysis discussed before. These observations support the evidence to the effect of high hydroxylation of the surface in the oxide nanostructure as the size gets smaller.

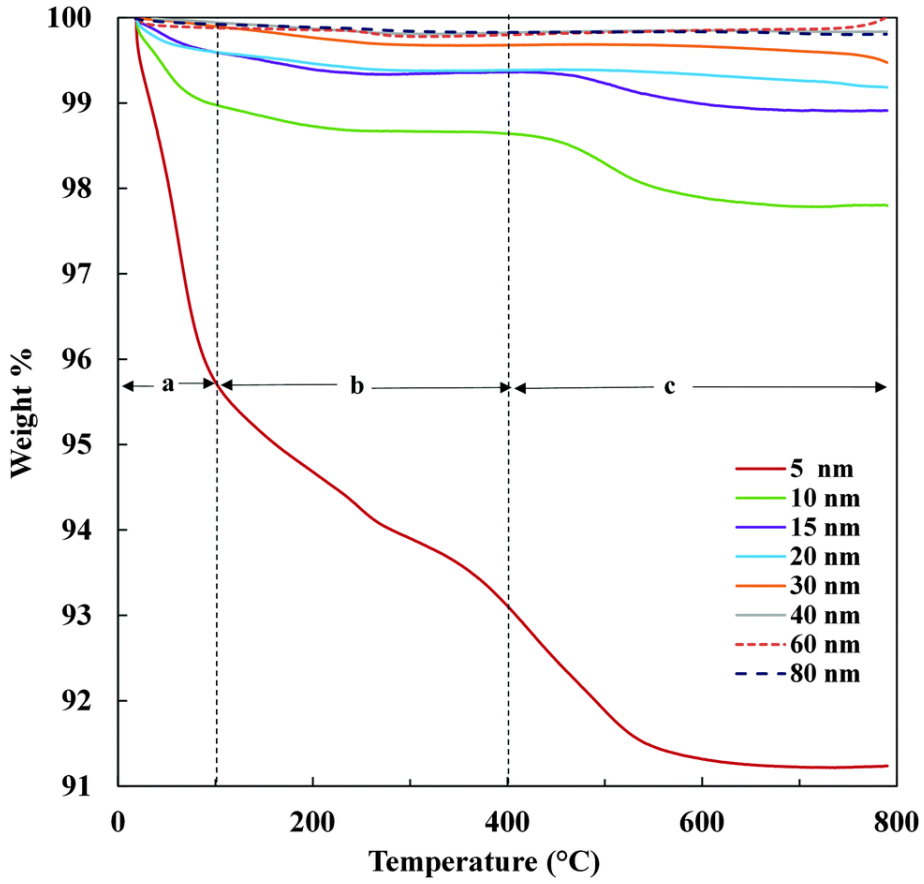

Figure 2.9 TGA thermograms of different sizes of NiO nanoparticles, with three mass regimes: a) gas desorption a) water molecules desorption a) dehydroxylation adjacent –OH groups.

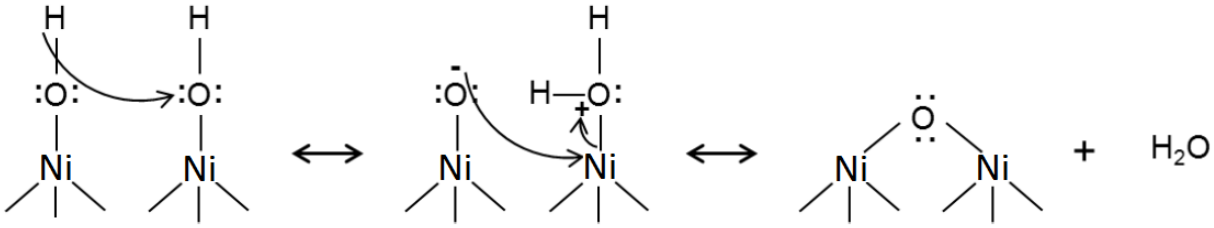

Figure 2.10 Pictorial representation of the dehydroxylation concept.

2.5.2 Computational modeling for adsorption of Q-65 molecules onto NiO nanoparticles

As described before, calculations of the adsorption of Q-65 molecules onto a 5 nm spherical NiO nanoparticle (closest to the actual size obtained experimentally for the real used small nanoparticles) were carried out to get some atomistic insight on the complex interaction of Q-65 molecules with the surfaces of NiO nanoparticles. Figure 2.11 illustrates the adsorption of one molecule (a), 10 molecules (b) and 80 molecules (c) of Q-65 onto the 5 nm spherical NiO nanoparticle. Figure 2.11a shows that the lowest configuration of one Q-65 molecule onto the spherical NiO nanoparticle is almost a flat one with the alkyl chain pointing upwards anchored by the interaction of the aromatic rings with the surface having the facet index {110} and having an adsorption energy of -433.2 kcal/mol.

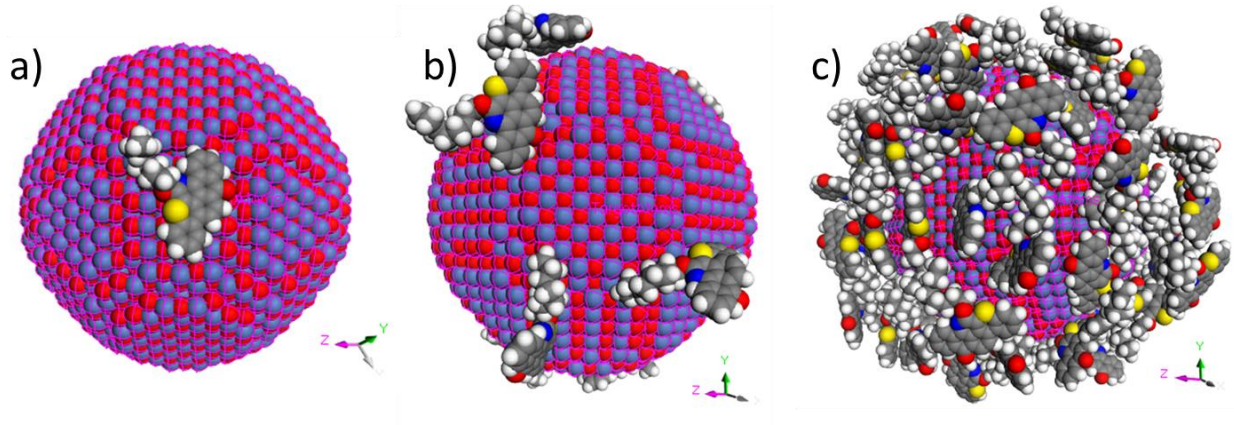

Figure 2.11 CPK images, with a 45 degree perspective, of the adsorption of Q-65 on the surfaces of a 5 nm NiO spherical nanoparticle. (a) adsorption of one molecule of Q-65 on the 5 nm NiO nanoparticle; (b) adsorption of 10 molecules of Q-65 on the 5 nm NiO nanoparticle; and (c) adsorption of 80 Q-65 molecules on the 5 nm spherical NiO nanoparticle. Bright blue atoms represent nitrogen, yellow atoms represent sulfur, gray atoms represent carbon, white atoms and the red atoms represent oxygen.

In Figure 2.11b, it is observed that as more Q-65 molecules are added (in this case 10), the vertical tilting of some of the Q-65 molecules is observed as compared when only one molecule of Q-65 is alone onto the nanoparticle surface. As more Q-65 molecules are adsorbed (80 molecules in Figure 2.11c), the lowest configuration order indicates that most of the molecules tend to be adsorbed in a vertical tilted form. This arrangement indicates that more Q-65 molecules can be adsorbed on the surface than it would be estimated by the flat configuration of the molecule, for this case, 1.1 molecules/nm^2 was estimated for the surface saturation in the spherical particle, pointing out the importance of surface morphology for Q-65 adsorption.

Following the findings above, and taking into account that the HRTEM images indicated that some NiO nanoparticles possessed a tablet-like morphology, hence the interaction of Q-65 molecules with a nanotablet of NiO (3 × 5 × 15 nm dimensions) were carried out and the lowest

energy configurations of Q-65 on this nanoparticle are presented in Figure 2.12. In the used nanotablet of NiO, in the lowest energy configuration found, one Q-65 molecule adsorbs on the only type of surface exposed {100} in an almost flat configuration with the alkyl chains pointing upwards as in the case of the nanosphere by interaction of the aromatic rings with the surface (Figure 2.12a); however, in this case the adsorption energy is -668.2 kcal/mol which is 235 kcal/mol lower than in the spherical nanoparticle. These results indicate that the morphology of the nanoparticles (exposed facets) will have an effect in the adsorption and catalytic behavior of the nanoparticles being composed of the same chemical elements (nickel and oxygen in this case). When a few more Q-65 molecules are added (10 molecules as observed in Figure 2.12b), the configuration of the molecules still resembles the almost flat one observed when only one molecule is adsorbed. This is different to the observation in the case of nanosphere where the vertical tilted configuration seems to be the dominant one, pointing out the importance of surface morphology for the adsorption of organic molecules. Adding 250 Q-65 molecules to the nanotablet makes the surface saturation with mostly flat oriented Q-65 molecules, but it is possible to observe very few Q-65 molecules with a vertical tilted configuration. Again, this indicates the importance of the surface morphology for guiding the adsorption of Q-65 molecules on the surface (Figure 2.11c). The surface saturation for this case is 0.9 molecules/nm^2 which is a slightly less than the one found for the spherical particle where tilted molecules are present (1.1 molecules/nm^2).

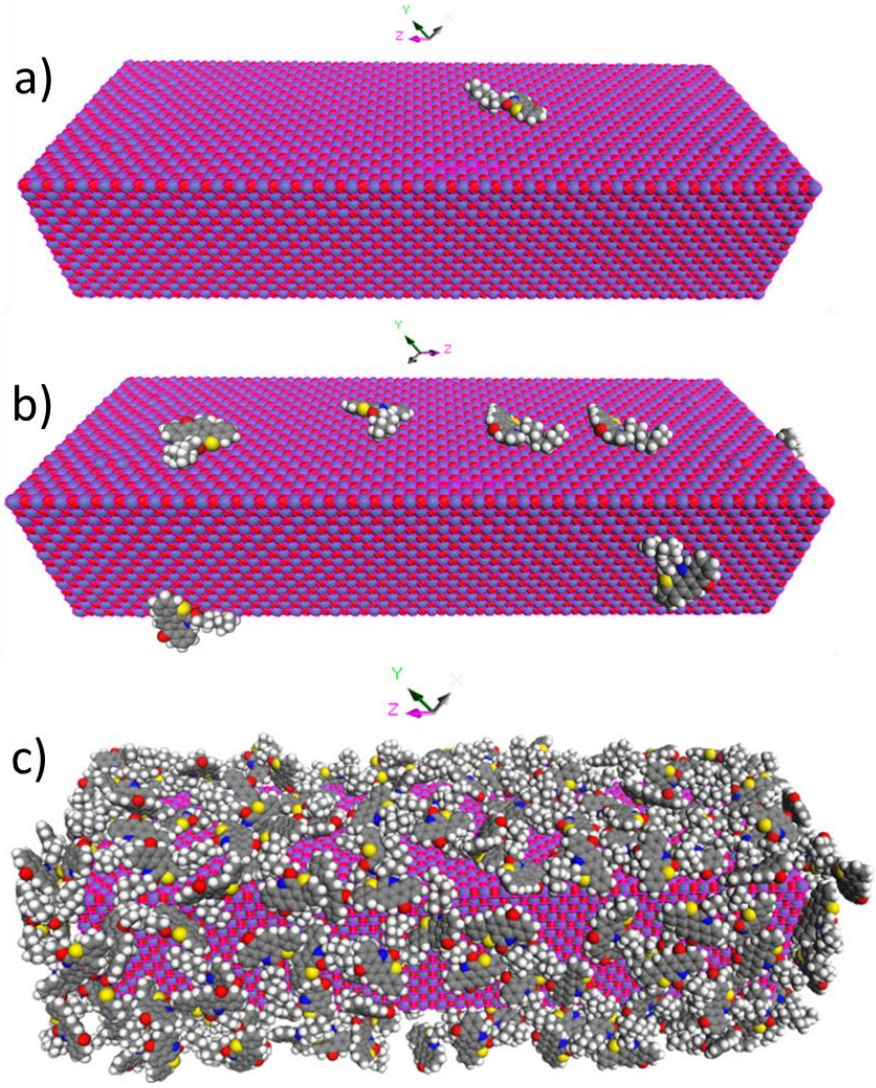

Figure 2.12 CPK images, with a 45 degree perspective, of the adsorption of Q-65 on the surfaces of a nanotablet (3x5x15 nm) of NiO. (a) adsorption of one molecule of Q-65 on the NiO nanotablet; (b) adsorption of 10 Q-65 molecules on the nanotablet of the NiO nanoparticle; and (c) adsorption of 250 Q-65 molecules on the nanotablet of NiO nanoparticle. Bright blue atoms represent nitrogen, yellow atoms represent sulfur, gray atoms represent carbon, white atoms represent hydrogen, red atoms represent oxygen, light blue atoms represent nickel and pink wireframe indicates the targeted atoms for the adsorption interaction on the surface.

2.5.3 Adsorption isotherms

To validate the findings of computational modeling and to better understand the adsorption of Q-65 molecules on different sizes of NiO nanoparticles, macroscopic solution phase adsorption

isotherms were performed to quantify surface coverage on these different-sized nanoparticles. The adsorption isotherms of Q-65 molecules onto different sizes of NiO nanoparticles are shown in Figure 2.13.

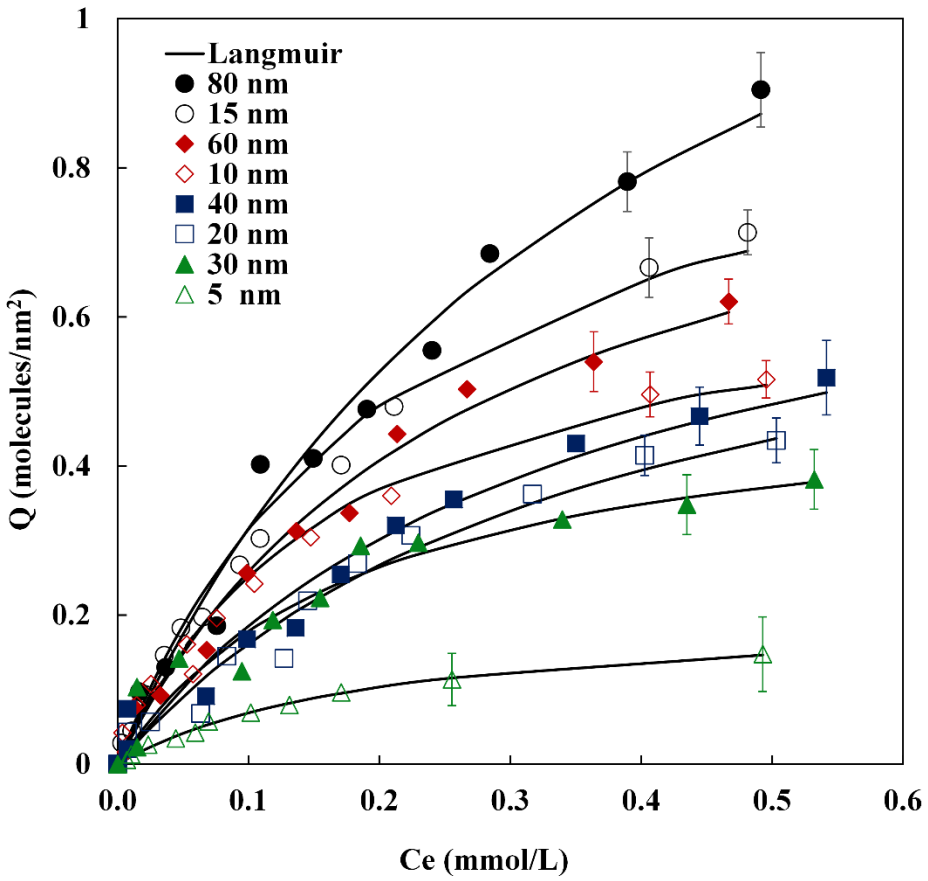

Figure 2.13 Effect of the NiO nanosize on Q-65 adsorptive removal. Experimental conditions are nanoadsorbent dose, 10 g L−1; shaking rate, 200 rpm; contact time = 24 h. The symbols are experimental data, and the solid lines are from the Langmuir model eq (2.4).

For all cases, the Langmuir and Freundlich adsorption models, represented by eqs 4 and 5, respectively (Langmuir, 1916, Freundlich, 1906), fit to the experimental data

$$Q_e = \frac{Q_{max} K_L C_e}{1 + K_L C_e} \qquad (2.4)$$

$$Q_e = K_F C_e^{1/n} \qquad (2.5)$$

where Q_e is the number of Q-65 molecules adsorbed onto the nanoparticles (molecule/nm^2), C_e is the solution phase equilibrium concentration (molecule/L), K_L is the Langmuir adsorption equilibrium constant related to the affinity of binding sites (L/molecule), Q_{max} is the maximum number of Q-65 molecules adsorbed for complete monolayer coverage (molecule/nm^2), and 1/n and K_F are Freundlich constants which are related to the adsorption affinity and adsorbed amount, respectively. Both Langmuir and Freundlich model parameters were estimated by minimization of the sum of squares of the differences between the experimental values and the predicted ones using the Solver features in Excel 2015. The non-linear Chi-square analyses, $\chi^2 = \sum \frac{(Q_e - Q_{eModel})^2}{Q_{eModel}}$ was used to evaluate the goodness of fitting results; where Q_e and Q_{eModel} are the adsorbed number of Q-65 molecules obtained experimentally and from modeling, respectively. The good fitting to the experimental data was indicated by the low Chi values. Table 2 lists the estimated values of the model parameters.

Table 2.2 Estimated Langmuir; K_L (L/molecule), Q_{max} (molecule/nm^2) and Freundlich parameters; 1/n (unit less), K_F [(molecule/nm^2)(L/molecule)$^{1/n}$] for Q-65 adsorption in solution at different NiO nanosizes.

	Langmuir			**Freundlich**		
Nominal NiO size (nm)	**$K_L \times 10^{15}$ (L/molecule)**	**Q_{max} (molecule/nm^2)**	**χ^2**	**$K_F \times 10^{10}$ [(molecule/nm^2)(L/molecule)$^{1/n}$]**	**1/n (unitless)**	**χ^2**
5	1.2810	0.2055	0.0020	0.0134	0.7303	0.0190
10	1.4630	0.6869	0.0010	1.3023	0.6317	0.0033
15	1.6072	1.0065	0.0013	0.3247	0.6797	0.0025
20	1.9168	0.7559	0.0068	0.9509	0.6317	0.0086
30	1.8223	0.4654	0.0017	1.7546	0.5156	0.0021
40	0.7552	0.8084	0.0016	1.2361	0.6273	0.0066
60	0.9384	0.9577	0.0037	0.9913	0.6431	0.0044
80	0.5141	1.9156	0.0042	0.0465	0.7417	0.0048

Clearly, for all NiO nanosizes, the Langmuir model presented a better fitting to the experimental data. This suggests that the selected nanoparticles portray saturation surface coverage. Furthermore, the data showed that, when normalized to BET surface area, there are significant differences in the adsorption of Q-65 molecules from toluene onto different-sized nanoparticles. Both Langmuir parameters (i.e., K_L and Q_{max}) differ with changing of particle size, indicating some differences in the adsorption of Q-65 molecules on the different-sized nanoparticles. Looking at Figure 2.13, it is evidently noted that the largest particle size has the highest uptake of Q-65 molecules under the tested conditions (1 molecule/nm^2 at the highest concentration tested). On the other hand, the smallest particle size has the lowest uptake, around 0.15 molecules/nm^2. For the other sizes, the uptake at the highest concentration of Q-65 in the solution seems to be between 0.35 and 0.7 molecules/nm^2, which are lower than the estimated values of 0.9-1.1 molecules/nm^2 obtained by the computational modeling. These experimental results confirm the importance of the nanoparticle surface topology and morphology on its adsorption of organic molecules. Variations on adsorption behavior of different-sized NiO nanoparticles towards Q-65 must then be expected, as different shapes and topologies are found in the particles forcing the adsorption of

less Q-65 molecules than theoretically expected. Infrared spectra (Figure 2.8b) and the TGA estimated density of hydroxyl groups showed that the smaller the nanoparticle the higher the hydroxyl density, thus, this chemical modification of the surface topology may also be contributing to the lower adsorption of Q-65 molecule on the surface of the smallest nanoparticles by changing the interaction of the particle with the organic molecule, and forcing less Q-65 molecules to be adsorbed. Larger flat surfaces seems to have the required adsorption sites to organize quite well big bulky molecules on their top. Hence, larger nanoparticles with extended flat surfaces can adsorb better more molecules. However, if the molecules are very small the trend may change, and thus, it is very important to understand not only the prepared nanoparticle size, topology and morphology, but also the selected molecule for their interaction.

2.6 Conclusion

This study is a first attempt to investigate the nanosize effect of nanoparticles toward adsorptive removal of asphaltene model molecule (like Quinolin-65, Q-65) from oil matrix. Different-sized NiO nanoparticles ranges from 5 to 80 nm were prepared in-house using the controlled thermal dehydroxylation method. The HRTEM images showed different shapes of the nanoparticles with different sizes. FTIR analysis identified the difference of the framework group and the hydroxyl density with different nanosizes. TGA analysis showed that the higher the nanosize the less the hydroxyl surface content, which provides more chances for the Q-65 molecules to be adsorbed and attached on the surface. The results of experimental adsorption isotherms support the characteristic studies and confirmed that NiO nanoparticles with 80 nm size have the highest adsorption capacity (molecule/nm^2), while 5 nm size particles have the lowest. Computational modeling was employed to get better insight on the Q-65 interaction with NiO nanoparticles with the assumption of

spherical or tablet-like shape nanoparticles. The results clearly indicate that, upon changing the nanosize between 5 and 80 nm, NiO nanoparticles undergo dramatic changes in surface properties, topology, morphology and textural properties which consequently impact their interfacial reactivity and adsorption behavior. We foresee that this size-dependent changes in morphology and textural properties will strongly affect the nanoparticle interfacial reactivity and its application in the oil and gas industry, particularly concerning their surface reactivity in enhancing crude oil upgrading and recovery and inhibition of formation damage.

2.7 References

ABBOUD, M., TURNER, M., DUGUET, E. & FONTANILLE, M. 1997. PMMA-based composite materials with reactive ceramic fillers. Part 1. Chemical modification and characterization of ceramic particles. Journal of Materials Chemistry, 7, 1527.

ADAMS, J. J. 2014. Asphaltene Adsorption, a Literature Review. Energy & Fuels, 28, 2831-2856.

AUFFAN, M., ROSE, J., BOTTERO, J. Y., LOWRY, G. V., JOLIVET, J. P. & WIESNER, M. R. 2009. Towards a definition of inorganic nanoparticles from an environmental, health and safety perspective. Nature Nanotechnology, 4, 634-41.

BARBIER, A., MOCUTA, C., KUHLENBECK, H., PETERS, K. F., RICHTER, B. & RENAUD, G. 2000. Atomic structure of the polar NiO(111)- p(2×2) Surface. Physical Review Letters, 84, 2897-2900.

BIJU, V. & KHADAR, M. A. 2003. Fourier transform infrared spectroscopy study of nanostructured nickel oxide. Spectrochim Acta A Mol Biomol Spectrosc, 59, 121-34.

BIOVIA Materials Studio Modeling and Simulation Software Version 7.0, Dassault Systemes, San Diego, California, USA, 2014. Home page: http://accelrys.com/products/materials-studio/.

BYKOVA, M. V., ERMAKOV, D. Y., KAICHEV, V. V., BULAVCHENKO, O. A., SARAEV, A. A., LEBEDEV, M. Y. & YAKOVLEV, V. A. 2012. Ni-based sol-gel catalysts as promising systems for crude bio-oil upgrading: Guaiacol hydrodeoxygenation study. Applied Catalysis B-Environmental, 113, 296-307.

ČERNÝ, V. 1985. Thermodynamical approach to the traveling salesman problem: An efficient simulation algorithm. Journal of Optimization Theory and Applications, 45, 41-51.

CHEMDRAW V14 STRUCTURAL DRAWING SOFTWARE, in: CambridgeSoft Corporation, a subsidiary of PerkinElmer, Inc, 2014.

DEVARD, A., PUJRO, R., DE LA PUENTE, G. & SEDRAN, U. 2012. Hydrocarbon Yield Structure in the conversion of heavy model molecules (Quinolin-65) on Fluidized Catalytic Cracking Catalysts. Energy & Fuels, 26, 5015-5019.

EL-QANNI, A., NASSAR, N. N., VITALE, G. & HASSAN, A. 2016. Maghemite nanosorbcats for methylene blue adsorption and subsequent catalytic thermo-oxidative decomposition: Computational modeling and thermodynamics studies. Journal of Colloid Interface Science, 461, 396-408.

FISHER, C. A. J. 2004. Molecular dynamics simulations of reconstructed NiO surfaces. Scripta Materialia, 50, 1045-1049.

FRANCO, C., PATINO, E., BENJUMEA, P., RUIZ, M. A. & CORTES, F. B. 2013. Kinetic and thermodynamic equilibrium of asphaltenes sorption onto nanoparticles of nickel oxide supported on nanoparticulated alumina. Fuel, 105, 408-414.

FREUNDLICH, H. M. F. 1906. Uber die adsorption in losungen. Zeitschrift fur Physikalische Chemie, 57, 385-470.

GROENZIN, H. & MULLINS, O. C. 2000. Molecular size and structure of asphaltenes from various sources. Energy & Fuels, 14, 677-684.

GUZMÁN, J. D., BETANCUR, S., CARRASCO-MARÍN, F., FRANCO, C. A., NASSAR, N. N. & CORTÉS, F. B. 2016. Importance of the adsorption method used for obtaining the nanoparticle dosage for asphaltene-related treatments. Energy & Fuels.

HASHEMI, R., NASSAR, N. N. & ALMAO, P. P. 2013. Enhanced heavy oil recovery by in situ prepared ultradispersed multimetallic nanoparticles: A study of hot fluid flooding for Athabasca bitumen recovery. Energy & Fuels, 27, 2194-2201.

HASHEMI, R., NASSAR, N. N. & PEREIRA ALMAO, P. 2014. Nanoparticle technology for heavy oil in-situ upgrading and recovery enhancement: Opportunities and challenges. Applied Energy, 133, 374-387.

HASSAN, A., CARBOGNANI-ARAMBARRI, L., NASSAR, N. N., VITALE, G., LOPEZ-LINARES, F. & PEREIRA-ALMAO, P. 2015. Catalytic steam gasification of n-C_5 asphaltenes by kaolin-based catalysts in a fixed-bed reactor. Applied Catalysis a-General, 507, 149-161.

HASSAN, A., LOPEZ-LINARES, F., NASSAR, N. N., CARBOGNANI-ARAMBARRI, L. & PEREIRA-ALMAO, P. 2013. Development of a support for a NiO catalyst for selective adsorption and post-adsorption catalytic steam gasification of thermally converted asphaltenes. Catalysis Today, 207, 112-118.

HOSSEINPOUR, N., KHODADADI, A. A., BAHRAMIAN, A. & MORTAZAVI, Y. 2013. Asphaltene adsorption onto acidic/basic metal oxide nanoparticles toward in situ upgrading of reservoir oils by nanotechnology. Langmuir, 29, 14135-14146.

JANG, H. D., KIM, S. K. & KIM, S. J. 2001. Effect of particle size and phase composition of titanium dioxide nanoparticles on the photocatalytic properties. Journal of Nanoparticle Research, 3, 141-147.

JØRGENSEN, J.-E., MOSEGAARD, L., THOMSEN, L. E., JENSEN, T. R. & HANSON, J. C. 2007. Formation of γ-Fe_2O_3 nanoparticles and vacancy ordering: An in situ X-ray powder diffraction study. Journal of Solid State Chemistry, 180, 180-185.

KAZEMZADEH, Y., ESHRAGHI, S. E., KAZEMI, K., SOURANI, S., MEHRABI, M. & AHMADI, Y. 2015. Behavior of asphaltene adsorption onto the metal oxide nanoparticle surface and its effect on heavy oil recovery. Industrial & Engineering Chemistry Research, 54, 233-239.

KIRKPATRICK, S., GELATT, C. D., JR. & VECCHI, M. P. 1983. Optimization by simulated annealing. Science, 220, 671-80.

LANGMUIR, I. 1916. The constitution and fundamental properties of solids and liquids Part I Solids. Journal of the American Chemical Society, 38, 2221-2295.

LIAO, P. Q., ZHANG, W. X., ZHANG, J. P. & CHEN, X. M. 2015. Efficient purification of ethene by an ethane-trapping metal-organic framework. Nature Communication, 6, 8697.

LIU, J., CHEN, P., DENG, L. H., HE, J., WANG, L. Y., RONG, L. & LEI, J. D. 2015. A Non-sulfided flower-like Ni-PTA catalyst that enhances the hydrotreatment efficiency of plant oil to produce green diesel. Scientific Reports, 5, 15576.

LÓPEZ-LINARES, F., CARBOGNANI, L., GONZÁLEZ, M. F., SOSA-STULL, C., FIGUERAS, M. & PEREIRA-ALMAO, P. 2006. Quinolin-65 and violanthrone-79 as model molecules for the kinetics of the adsorption of C_7 athabasca asphaltene on macroporous solid surfaces. Energy & fuels, 20, 2748-2750.

MA, D. 2003. Investigation into the dielectric behavior of titanium dioxide/polyethylene nanocomposites. Rensselaer Polytechnic Institute.

MCQUAID, M. J., SUN, H. & RIGBY, D. 2004. Development and validation of COMPASS force field parameters for molecules with aliphatic azide chains. Journal of Computational Chemistry, 25, 61-71.

MOJELSKY, T. W., IGNASIAK, T. M., FRAKMAN, Z., MCINTYRE, D. D., LOWN, E. M., MONTGOMERY, D. S. & STRAUSZ, O. P. 1992. Structural features of Alberta oil sand bitumen and heavy oil asphaltenes. Energy & Fuels, 6, 83-96.

MUELLER, R., KAMMLER, H. K., WEGNER, K. & PRATSINIS, S. E. 2003. OH surface density of SiO_2 and TiO_2 by thermogravimetric analysis. Langmuir, 19, 160-165.

MULHERAN, P. A. 1993. Structural Calculations of Oxide Surfaces at Finite-Temperature. Philosophical Magazine a-Physics of Condensed Matter Structure Defects and Mechanical Properties, 68, 799-808.

NASSAR, N. N., FRANCO, C. A., MONTOYA, T., CORTÉS, F. B. & HASSAN, A. 2015. Effect of oxide support on Ni-Pd bimetallic nanocatalysts for steam gasification of n-C_7 asphaltenes. Fuel, 156, 110-120.

NASSAR, N. N., HASSAN, A., CARBOGNANI, L., LOPEZ-LINARES, F. & PEREIRA-ALMAO, P. 2012. Iron oxide nanoparticles for rapid adsorption and enhanced catalytic oxidation of thermally cracked asphaltenes. Fuel, 95, 257-262.

NASSAR, N. N., HASSAN, A. & PEREIRA-ALMAO, P. 2011a. Application of nanotechnology for heavy oil upgrading: catalytic steam gasification/cracking of asphaltenes. Energy & Fuels, 25, 1566-1570.

NASSAR, N. N., HASSAN, A. & PEREIRA-ALMAO, P. 2011b. Metal oxide nanoparticles for asphaltene adsorption and oxidation. Energy & Fuels, 25, 1017-1023.

NASSAR, N. N., HASSAN, A. & VITALE, G. 2014. Comparing kinetics and mechanism of adsorption and thermo-oxidative decomposition of Athabasca asphaltenes onto TiO_2, ZrO_2, and CeO_2 nanoparticles. Applied Catalysis A: General, 484, 161-171.

OLIVER, P. M., WATSON, G. W. & PARKER, S. C. 1995. Molecular-dynamics simulations of nickel oxide surfaces. Phys Rev B Condens Matter, 52, 5323-5329.

SHENG, X., SCIENCE, I. S. U. M. & ENGINEERING 2008. Polymer nanocomposites for high-temperature composite repair, Iowa State University.

SING, K. S. W. 2009. Reporting physisorption data for gas/solid systems with special reference to the determination of surface area and porosity (Provisional). Pure and Applied Chemistry, 54, 2201-2218.

SING, K. S. W., EVERETT, D. H., HAUL, R. A. W., MOSCOU, L., PIEROTTI, R. A., ROUQUEROL, J. & SIEMIENIEWSKA, T. 2008. Reporting physisorption data for gas/solid systems. Handbook of heterogeneous catalysis. Wiley-VCH Verlag GmbH & Co. KGaA.

SONG, C. S. 2006. Global challenges and strategies for control, conversion and utilization of CO_2 for sustainable development involving energy, catalysis, adsorption and chemical processing. Catalysis Today, 115, 2-32.

TAYLOR, M. B., SIMS, C. E., BARRERA, G. D., ALLAN, N. L. & MACKRODT, W. C. 1999. Quasiharmonic free energy and derivatives for slabs: Oxide surfaces at elevated temperatures. Physical Review B, 59, 6742-6751.

WANDER, A., BUSH, I. J. & HARRISON, N. M. 2003. Stability of rocksalt polar surfaces: An \textit{ab initio} study of MgO(111) and NiO(111). Physical Review B, 68, 233405.

XU, B. Q., WEI, J. M., YU, Y. T., LI, Y., LI, J. L. & ZHU, Q. M. 2003. Size limit of support particles in an oxide-supported metal catalyst: Nanocomposite Ni/ZrO2 for utilization of natural gas. Journal of Physical Chemistry B, 107, 5203-5207.

YAN, M., CHEN, S. P., MITCHELL, T. E., GAY, D. H., VYAS, S. & GRIMES, R. W. 1995. Atomistic Studies of Energies and Structures of (Hk0) Surfaces in NiO. Philosophical Magazine a-Physics of Condensed Matter Structure Defects and Mechanical Properties, 72, 121-138.

YEAN, S., CONG, L., YAVUZ, C. T., MAYO, J. T., YU, W. W., KAN, A. T., COLVIN, V. L. & TOMSON, M. B. 2005. Effect of magnetite particle size on adsorption and desorption of arsenite and arsenate. Journal of Materials Research, 20, 3255-3264.

ZHANG, D. D., WEI, D. L., LI, Q., GE, X., GUO, X. F., XIE, Z. K. & DING, W. P. 2014. High performance catalytic distillation using CNTs-based holistic catalyst for production of high quality biodiesel. Scientific Reports, 4, 4021.

ZHAO, L. F., LIU, L. C. & SUN, H. 2007. Semi-ionic model for metal oxides and their interfaces with organic molecules. Journal of Physical Chemistry C, 111, 10610-10617.

CHAPTER THREE: CATALYTIC EFFECT OF NANOSIZED NiO NANOPARTICLES IN THERMO-OXIDATIVE DECOMPOSITION OF QUINOLIN-65

This Chapter is adapted from the following manuscript:

MAREI, N. N., NASSAR, N. N., VITALE, G. & HASSAN, A. 2016. Catalytic effect of nanosized NiO nanoparticles in thermo-oxidative decomposition of Quinolin-65. Submitted to Catalysis Science & Technology Journal, RSC.

3.1 Abstract

In a previous study, the effect of the nanosize on surface properties of NiO nanoparticles for the adsorption of Quinolin-65 (Q-65) from toluene-based solution has been clarified and well refuted. In this study, the effect of nanosize of NiO nanoparticles on catalytic thermo-oxidative decomposition of the adsorbed Q-65 was investigated using TGA/DTA and TGA-MS systems. It was shown that strong effects were observed for particle size in the range of 5 to 15 nm and weak effects in the range of 30-40 nm. Kissinger-Akahira-Sunose (KAS) was used to describe the oxidation mechanism and to confirm the validity of the catalytic effect of the different-sized NiO nanoparticles. Taken together, the kinetic triplets (i.e., the effective activation energy E_α, the pre-exponential factor A_α and the reaction function, $f(\alpha)$ are essential specifications to examine and allow meaningful comparisons of the catalytic activity of the different-sized NiO nanocatalysts. The gas analysis TGA-MS system and the thermodynamic parameters suggested that the smaller the particle size is the higher the catalytic activity and the faster CO_2 formation. The effect of the nanosize on the regeneration process has been studied as well. XRD and BET have been used to characterize the regenerated nanocatalysts.

3.2 Introduction

In recent years, metal-based nanoparticles have attracted herculean attention considering their extraordinary catalytic (Alizadeh-Gheshlaghi et al., 2012), photosensitive (Khaing Oo et al., 2011), electrical (Luo et al., 2006), and magnetic properties (Khoobi et al., 2015), as well as their potential application in several fields of energy (Fei Guo et al., 2014, Hashemi et al., 2012), environment (Masciangioli and Zhang, 2003, Zhang), engineering and science (Jain et al., 2008, Franke et al., 2006). Last few years, many extensive research efforts have been performed on employing metal-based nanoparticles as adsorbent and catalysts in oil upgrading and recovery processes (Nassar et al., 2015, Nassar et al., 2014, Guzmán et al., 2016, Hassan et al., 2015, Hashemi et al., 2014b). Over the years, asphaltene existence in crude oil matrix has been a major problem in the oil industry (Kamran Akbarzadeh, 2007) due to the presence of heteroatoms in its structure, which are mostly contained in the aromatic rings. These heteroatoms can polarize the aromatic ring systems and subsequently the charge separation induced by heteroatoms cause the centers of neighboring asphaltene molecules to stick to each other (Adams, 2014, Kamran Akbarzadeh, 2007). Accordingly, asphaltenes exhibit a self–associating feature that promotes aggregation and subsequently increases the viscosity of crude oil (Adams, 2014). This would negatively influence the entire production chain, starting from the well where asphaltenes can reduce oil recovery and consequently decrease the productivity index by changing reservoir wettability, rock pore plugging, and deposition of asphaltene within wells (Adams, 2014, Kamran Akbarzadeh, 2007). High selectivity adsorption techniques, focusing mainly on the removal of asphaltenes rather than on the whole crude oil matrix will considerably improve efficiency. However, using the traditional adsorption process would result in massive solid waste hydrocarbons that need special treatment

and/or disposal. Our alternative proposition is to separate the unstable, seed to coke formation, heavy polar hydrocarbons by adsorbing them onto a solid adsorbent-catalyst and, consequently, upgrade these heavy fractions into light utilizable distillates. Nevertheless, deactivation (i.e., fouling (Rase, 2013). Poisoning (Bartholomew, 2001) and sintering (Wanke and Flynn, 1975) of conventional heterogeneous catalysts are omnipresent problem that causes loss catalytic activity of the classical catalyst. In this context, nanoparticle technology is emerging as a promising alternative for enhancing heavy oil upgrading and recovery (Hashemi et al., 2014b). Given the molecular characteristics of bitumen or heavy oil and the limitations of conventional porous catalysts, metal-based nanoparticles have unique features that make them suitable candidates for enhancing upgrading and recovery processes (Esfandyari Bayat et al., 2014, Nassar et al., 2011d). These features include small particle size, dispersability, easy tunable surface functionalities, chemical and thermal stability and high surface area to volume ratio (Kim and Kwak, 2007, Nassar, 2012). Recent researches were targeting the use of metal-based nanocatalysts for heavy oil quality improvement and problematic heavy hydrocarbons removal (Nassar et al., 2014, Franco et al., 2013, Nassar et al., 2011d, Adams, 2014, Hashemi et al., 2014a, Franco et al., 2015, Hashemi et al., 2013). In fact, the ability of nanoparticles to interact with polar heavy hydrocarbon molecules has shown to play an important role in their consequent processing such as adsorption (Nassar et al., 2011d, Guzmán et al., 2016, Hosseinpour et al., 2013), post-adsorption thermo-oxidative decomposition (Nassar et al., 2014, Alizadeh-Gheshlaghi et al., 2012), catalytic steam gasification (Nassar et al., 2015, Hassan et al., 2015), and enhanced oil upgrading and recovery (Hashemi et al., 2014b), Different types of supported and unsupported nanoparticles have been employed for adsorptive removal of asphaltenes from an oil matrix (Hassan et al., 2013, Nassar et al., 2011a). Asphaltene adsorption onto different surfaces of metal oxide nanoparticles showed that the

adsorption is strongly dependent on the type of nanoparticles and its surface acidity as well as asphaltene origin and adsorption conditions. These factors were believed to influence the catalytic activity of the nanoparticles toward post-adsorption asphaltene decomposition. On the surface area-normalized basis, nano-alumina showed higher adsorption capacity for asphaltene than micro-alumina particles, while the latter were found to be more catalytically active than the former (Nassar et al., 2011c). Further, basic alumina particles were found to be more catalytically active compared to acidic alumina particles, while more asphaltenes were adsorbed on the latter than the former (Nassar et al., 2011b). These differences in adsorption capacity and catalytic activity of the surfaces could be related to the type of active sites and faces exposed, as asphaltene adsorption may only occur at specific sites. It is worth noting here that, it was only recently recognized that nanozise of metal oxide nanoparticles play a vital role in controlling their surface properties, shape, functionality, and morphology (Marei et al., 2016). However, the nanosize effect on the catalytic properties of metal oxide nanoparticles towards heavy hydrocarbon thermal decomposition is as yet unclear. Many researchers have attributed the different surface area of different nanosize particles as the only reason for different catalytic activity (Strizhak, 2013). Inappropriately, to blame the surface for such a various catalytic activity, is not really a fair comparison to compare different sizes of catalyst on surface area basis only. Meanwhile, other researchers were very honest to say "the origin of the size effect is not yet understood" (Henry et al., 1997), and questioned "how much of this effect is due to the particle size" (Ozkan, 2009).

More recently, our research group has proven that nanosize has a significant impact not only on the surface area but on many other factors (Marei et al., 2016). It is evident that changing the nanoparticle size, in this case NiO, between 5 to 80 nm, drastically changes the surface topology, morphology and textual properties which consequently impact the interfacial reactivity as well as

the overall adsorption behavior. This stresses the need to revisit the previous factors taking the nanosize effect into account and highlights the effect of different nanoparticle sizes towards heavy hydrocarbon post-adsorption catalytic thermal decomposition, using Q-65 as an asphaltene model molecule (Devard et al., 2012, López-Linares et al., 2006, Marei et al., 2016). To evaluate the validity of our findings and perform a reasonable fair comparison of different nanosizes on Q-65, we dealt with the adsorption uptake as molecule/nm^2. Herein, this study continues our previous work and it aims at investigating the effect of nanosize of NiO nanoparticle on the catalytic thermo-oxidative decomposition of the adsorbed Q-65 molecules by using a thermogravimetric analyzer coupled with an online mass spectrometer. This is also achieved by analyzing the evolved CO_2 gas to determine the CO_2 impact from the Q-65 post-adsorption oxidation. The Kissinger-Akahira-Sunose (KAS) method was used here to estimate the kinetic triplets like effective activation energy, pre-exponential factor, and reaction model of the oxidation reaction.

3.3 Experimental work

3.3.1 NiO nanoparticles

NiO nanoparticles with nominal size ranges between 5 and 80 nm were prepared by the controlled thermal dehydroxylation of $Ni(OH)_2$, as described in our previous study (Marei et al., 2016). In brief, a specified amount of nickel nitrate ($Ni(NO_3)_2.6H_2O$), obtained from Sigma-Aldrich, was dissolved in deionized water and, subsequently NaOH pellets, obtained from VWR, was added pellet by pellet under magnetic stirring until a pH of 11 was attained to precipitate small nickel hydroxide particles ($Ni(OH)_2$). 100 °C. The dried material was then calcinied with a ramp of 5 K/min for 2-3 h at temperatures in the range of 300 °C to 700 °C to get different-sized NiO nanoparticles by controlling the calcination variables i.e., temperature and time. The obtained different-sized nanoparticles were employed to adsorb Quinolin-65 (Q-65) ($C_{30}H_{29}NO_2S$, MW = 467.62 $g.mol^{-1}$, λ_{max} = 375 nm, dye content 80%) purchased from Sigma-Aldrich, Ontario. Q-65 was used as an adsorbate and model asphaltene molecule as detailed in the previous study and the adsorption isotherms have been obtained (Marei et al., 2016). Figure 3.1 (shows the chemical structure of Q-65. Table 3.1 shows the characteristics of the in-house prepared different-sized NiO nanoparticles and the Langmuir adsorption isotherm constants. Detailed information about these characteristics and adsorption parameters can be found in our previous study (Marei et al., 2016). Worth noting here that the different-sized nanoparticles portray different shapes and surface topologies. Accordingly, they have shown different surface area and consequently different mechanism and configuration of interactions with the Q-65 molecules. This expected to impact the surface catalytic activity during the thermo-oxidative reaction of the adsorbed Q-65 molecules.

Table 3. 1 Characteristics of the selected NiO nanoparticles (Marei et al., 2016).

Nominal size (nm)	5	15	30	40
Average crystal size (nm)	4.6	13.2	27	39.4
BET surface area (m^2/g)	158	42	17	11
Shape	Connected and aggregated forming a rod-like morphology	Connected and aggregated forming a rod-like morphology	Flat thin sheets connected to each other	Cylindrical sheet
Q-65 configuration	Vertical tilted form	Vertical tilted form	Flat with the alkyl chain pointing upwards. Aromatic rings attracted to the surface	Flat with the alkyl chain pointing upwards. Aromatic rings attracted to the surface
Adsorption maximum uptake Q (molecule/nm^2)	0.21	1.01	0.47	0.81
Adsorption maximum uptake Q (mg/g)	18.1	23.3	5.0	4.4
Langmuir constant K_L (L/molecule)	1.3	1.1	1.8	0.8

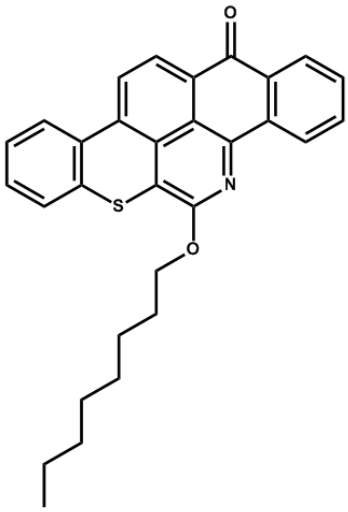

Figure 3.1 Q-65 molecular structure drawn with ChemDraw V14. The resemblance with a asphaltene molecule can be seen by the archipielago aromatic region, the alkyl chain and the presence of heteroatoms like sulfur, nitrogen and oxygen.

3.3.2 Evaluation of different-sized NiO nanoparticle as catalysts

The dried prepared different-sized NiO nanoparticles with adsorbed Q-65 molecules were subjected to catalytic thermal oxidation tests using a simultaneous thermogravimetric analysis/differential scanning calorimetry (TGA/DSC) analyzer (SDT Q600, TA Instruments, Inc., New Castle, DE). In a typical experiment, and to avoid mass transfer limitation small amount (e.g., 5 mg) of NiO containing adsorbed Q-65 is oxidized at a set heating program from 25 to 700 °C at three different heating rates of 5, 10, and 20 °C/min, in separate experiments, in an air atmosphere. The airflow was kept at 100 cm^3/min during the experiments. Evolved gas analysis (EGA) was also carried out by an online mass spectrometer (MS) (Pfeiffer Vacuum GSD 301 O_2, Omnistar, Deutschland) attached to the TGA/DSC system to detect CO_2 production. For EGA experiments, a sample mass of 10 mg, airflow of 30 cm^3/min and a heating rate of 10°C/min was used. The TGA instrument was calibrated for mass and heat changes using sapphire as a reference for heat calibration and zinc as a reference for temperature calibration. Thermal analysis of original Q-65 solid was also performed for comparison purposes and to get more insight about the catalytic effect of different-sized nanoparticles on adsorbed Q-65 oxidation.

3.3.3 Regeneration of spent different-sized NiO nanoparticles

In practice, catalysts cost and performance will be dependent on its recyclability. Hence, to test the reusability of the different-sized nanoparticles, in this sets of experiments the spent different-sized NiO nanoparticles were regenerated by oxidizing the adsorbed Q-65 with TGA. The regeneration was accomplished using 30 mg of the dried sample in each run, at heating rate of 40 °C/min to reach 600 °C and air flow 100 cm^3/min. Then, the recycled nanoparticles were washed with deionized water and vacuum dried at 60 ◦C for 24 h and re-used for the subsequent adsorption-

oxidation cycle. Three cycles of consecutive adsorption–oxidation–regeneration were carried out to validate the reusability of different-sized NiO nanoparticles as adsorbents and catalysts for the removal and conversion of Q-65 molecules.

X-ray diffraction (Rigaku ULTIMA III X-ray diffractometer) with Cu Kα radiation was used to identify the structure and crystal size of the spent nanoparticles. The scan was performed in the range 30–90º 2θ using a 0.02º step and a counting time of 1º/min. The crystalline domain sizes were measured using the Debye-Scherrer equation as implemented in the commercial software JADE (JADE V 7.5.1 XRD) (provided with the diffractometer), by calculating the full width at half-maximum (FWHM) of the peaks fitting the experimental profile to a pseudo-Voigt profile function. The surface areas of the prepared and spent nanoparticles were estimated following the Brunauer-Emmett-Teller (BET) method. This was reached by applying nitrogen physisorption at 77 K, using a Micromeretics Tristar 3000 surface area analyzer, Norcross, GA. The samples were degassed at 150 °C under N_2 flow overnight before analysis.

3.4 Results and Discussion

3.4.1 TGA-MS for Q-65 adsorbed on different-sized NiO nanoparticles

Figure 3.2a shows the rate of mass loss for the catalytic oxidation of Q-65 on different-sized NiO nanoparticles. As seen, for the original Q-65 oxidation, without nanocatalysts, the mass loss occurs in two temperature regions, a low temperature oxidation between 250-400 °C and a high temperature oxidation between 450-650 °C. However, the rate of mass loss shows a significant shift in the presence of NiO nanosizes. Mass loss rate was shown to be started earlier with presence of 5 nm followed by 15, 30 and 40 nm. Moreover, Figure 3.2b shows the heat profile of Q-65 oxidation. The main exothermic peak depicting high temperature oxidation of Q-65 takes place beyond 550 °C meanwhile with presence of NiO the main heat flow peaks appears to be less than 350 °C following the same trend of mass loss rate (Figure 3.1a). Figure 3.1b shows that the amount of heat evolved during the oxidation of adsorbed Q-65 is least for 30 and 40 nm NiO nanoparticles and almost the same for 5 and 15 nm nanoparticles. The amount of heat eveloved during oxidation is proportional to the amount of Q-65 adsorbed over NiO surface (Marei et al., 2016). Therefore, this data shows that adsorption over 30 and 40 nm NiO particle is the least. Oxidation of adsorbed Q-65 over 5 and 15 nm NiO nanoparticles gives close values for heat loss during the oxidation process; showing that they have close amounts of Q-65 adsorbed over the surface which agrees with the adsorption capacity (mg/g) values shown in Table 3.1.

Figure 3.2c shows the conversion degree (α) with the temperature calculated as per eq (3.1) (Vyazovkin, 2011a)

$$\alpha = \frac{m_o - m_t}{m_o - m_f} \qquad (\mathbf{3.1})$$

where, m_0, m_f and m_t are the initial sample mass, the sample mass at a given time and the final mass of the sample, respectively.

As seen, original Q-65 conversion graph shows two main mass loss stages. First stage, where α is between 0 and 0.28. This is attributed to the loss of the olefin chain, as it is equivalent to 28% by weight of the whole Q-65 molecule. The second stage, where α is between 0.35 and 1, depicts the oxidation of the aromatic rings (Nassar et al., 2011d). In the region where α is between 0.3 and 0.35, it appears that the total reaction effect is the same and independent of the heating rate within this region. This suggests the consecutive reaction sequence and the oxidation of aromatic ring (the second stage, resembled by the second peak in the TGA profile) must be always after the oxidation of olefin chain (the first stage, resembled by the first peak in the TGA profile). Hence, the loss of olefin chain is the rate-limiting step for the reaction of origin Q-65.

In the presence of nanoparticle, at a fixed temperature, α increases as the nanopartile size decreases. This suggests the lower the particle size the faster is the oxidation reaction. As seen in Figure 3.1a, when adsorbed into different-sized NiO nanoparticles, Q-65 oxidation occurs at much lower temperature. The mass loss profiles are different for each size of NiO nanoparticles. This suggests that the mechanism of oxidation of adsorbed Q-65 changes with the size of nanoparticles. For instance, T_{max} for the oxidation reaction in the presence of different-sized NiO nanoparticles in the heat loss profile can be divided into low (below 300 °C) and high (above 300 °C) temperature oxidation zones. For the case of 30 and 40 nm particle size, low temperature oxidation zone is not very difinitive perhaps because of the low amounts of Q-65 adsorbed (Table 1). However, in the case of 5 and 15 nm particles the low temperature oxidation zone appears to have a disctinct peak. Evolved gas analysis by mass spectrometry is shown in Figure 3.1d. The CO_2 peak (m/e =44) obeserved by mass spectrometer shows clearly the effect of NiO particle size on

Q-65 oxidation. It can be seen that the smaller the particle size the quicker (lower temperature) is the CO_2 formation; depiction higher catalytic activity which supports the findings in Figure 3.2a,b and c. For sure the differences are small but they are signifcant enough to validate the particle size effect. The amount of CO_2 evolved is another way of seeing the amount of Q-65 adsorbed on NiO surface. Amount of CO_2 released during oxidation of adsorbed Q-65 on 30 and 40 nm particle is very low (m/e 44 peak intensity plotted on secondary axis) depicitng litlle adsorption over the surface.

Let us start organizing the things here. Its not surprising to see that the smaller the size the higher surface area and the higher the adsorption capacity per mass (mg/g). What is really surprising is when we are looking on the adsoprtion capacity (molecule/nm^2) of each nanopartilce separatley which appears to be less on the smaller nanosizes and more on the bigger nanosizes. Followed by TGA-MS that shows the smaller the nanosize the faster Q-65 oxidation reaction. These results show the dependency of the catalytic activity of the oxidation reaction on the nanosize which consequently affect on the morpoholgy, shape and topology. The change in nanoparticle sizes, causes changes in the coordination numbers of the atoms on the catalyst surface and affects on the population of the facets, the concentration of defects, modifies the work function of metals and change the chemisorption energy (Yoo et al., 2010, Zhou et al., 2006, Hammer and Nørskov, 2000). As the nanosize decreases the average coordination number of atoms decreases, which results in a size-dependent degree of surface bond contraction and reconstruction, lattice strain increases, basically as a result of this surface bond contraction. The populations of the various crystal facets increase, consequence of a change in the lowest energy arrangement of atoms. The concentration of surface defects increases, the work function of the metal increases and the ability

to activate O_2 for oxidation reaction increases (Zhou et al., 2006, Schnippering et al., 2007, Campbell, 2013).

Consequently, the adsorption configuration reported in the previous study (Marei et al., 2016) and summarized in Table 3.1 shows the different Q-65 computational configuration on the different NiO nanosizes, since the smaller nanoparticles tend to adsorb Q-65 molecules in a vertical tilted form. On the other hand, the bigger nanoparticles show more flat from the aromatic rings side, with lower adsorption energy than smaller nanoparticles which mean stronger adsorption. Therefore, strongly enough adsorption for the adsorbed molecules to react occurs on the surface of smaller nanoparticles. But not too strong as the big nanoparticles, while the adsorbed molecules will stick strongly on the surface and cannot break down, also any product might tend to remain adsorbed on the surface instead of fully oxidized (Clark, 2000, Marei et al., 2016).

Taken together, all the aforementioned factors allow meaningful comparisons of the catalytic activity of the different-sized NiO nanocatalysts and support that the lower the particle size the higher the catalytic activity.

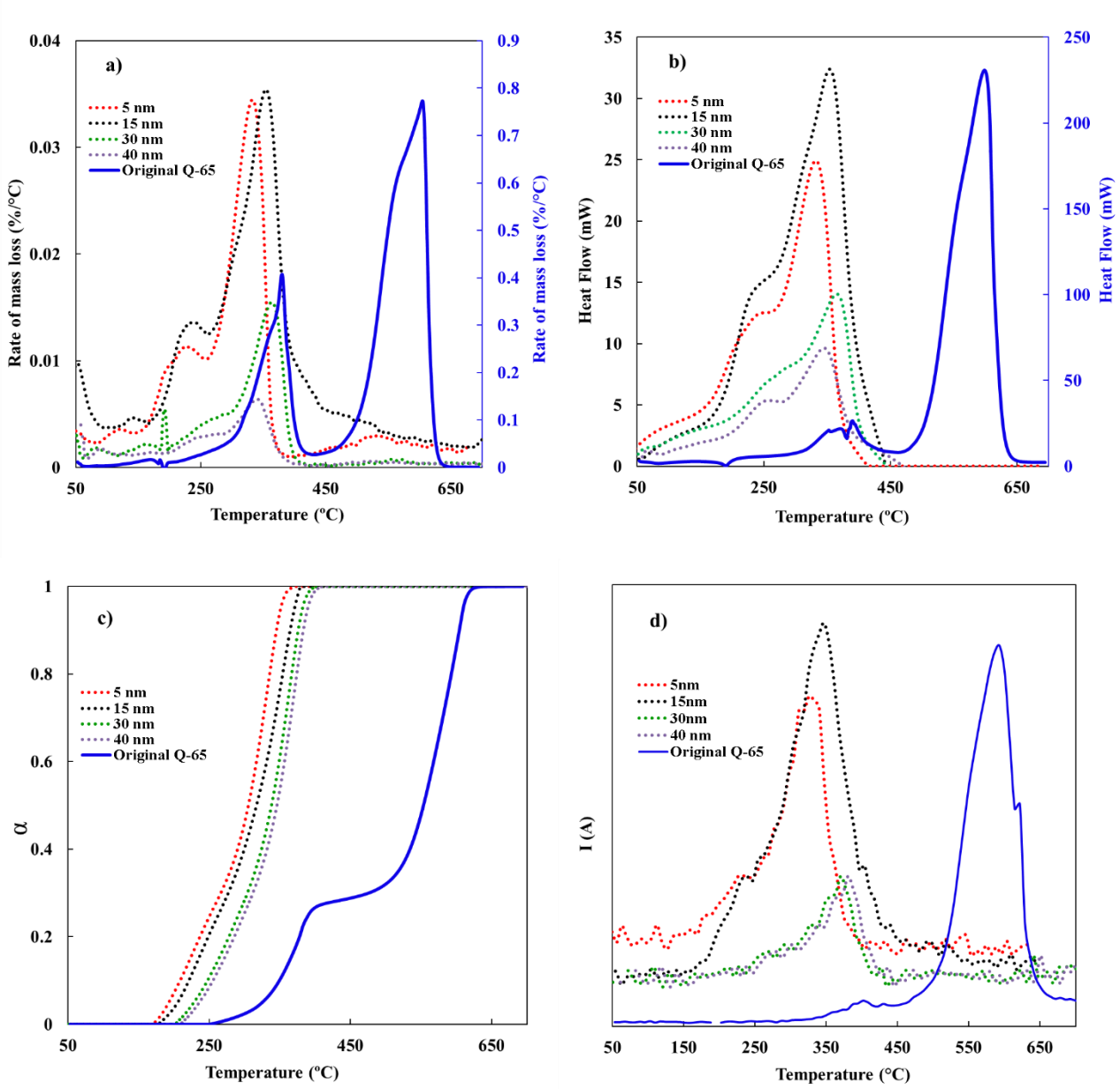

Figure 3.2 TGA-MS plots of Q-65 oxidation. a) Rate of mass loss for Q-65 catalytic oxidation in the absence and presence of NiO different nanosizes, b) Plot of heat changes as a function of temperature, c) Percent conversion and d) Evolution of the production of CO_2. Heating rate = 10°C/min; air flow, 30 cm^3/min.

3.4.2 Estimation of effective activation energy

To understand the oxidation kinetics of Q-65 in presence and absence of different NiO nanoparticle sizes. Nonlinear procedures in isoconversional computations of the effective activation energy of nonisothermal reactions was used to describe the oxidation mechanism of Q-65 before and after adsorption onto different-sized NiO nanoparticles, and to confirm the validity of the catalytic effect of the different particle sizes of NiO nanoparticles on the basis of the kinetic triplets (i.e., effective activation energy trends, preexponential factor, and reaction model) (Vyazovkin et al., 2011, Nassar et al., 2013, Vyazovkin, 2015).

The solid reaction kinetics are usually described as eq (3.2) (Vyazovkin and Dollimore, 1996, Vyazovkin, 2011)

$$\frac{d\alpha}{dt} = K(T) \times f(\alpha) \qquad (\mathbf{3.2})$$

$f(\alpha)$ is the reaction model, α is the extent of reaction, K(T) is the Arrhenius rate constant which is temperature dependent factor, T is the temperature, t is the time. Values of the conversion degree (α) ranges from 0-1 with the time is dependent on K(T) rate of the reaction and the reaction model $f(\alpha)$ to get dα/dt in eq (3.2)

By representing the rate constant using Arrhenius law with isoconversionl basis we get:

$$\mathrm{K(T)} = A_\alpha \exp\left(\frac{-E_\alpha}{RT}\right) \qquad (\mathbf{3.3})$$

where Eα is the activation energy depending on the conversion α, Aα is the preexponential factor describing the degree of conversion, and R is the ideal gas constant. In case of isothermal process. For nonisothermal conditions where temperature varies with time with a constant heating rate β=dT/dt, the following rule is defined:

$$\frac{d\alpha}{dT} = \frac{dt}{dT} \times \frac{d\alpha}{dt} \qquad (\mathbf{3.4})$$

where dα/dT, is the isothermal reaction rate, dα/dt, is the non-isothermal reaction rate and is the inverse of heating rate ($1/\beta$), and by combining the eqs (3.2), (3.3) and (3.4) we end up with eq (3.5) as follows:

$$\frac{d\alpha}{dT} = (A_\alpha/\beta)\exp\left(\frac{-E_\alpha}{RT}\right) f(\alpha) \qquad (\mathbf{3.5})$$

By integrating eq (3.5) one can get:

$$g(\alpha) = \int_0^\alpha \frac{d\alpha}{f(\alpha)} = (A_\alpha/\beta)\int_0^T \exp\left(\frac{-E_\alpha}{RT}\right) dT \qquad (\mathbf{3.6})$$

This is a none solvable integration by the analytical method (Coats and Redfern, 1964) and can be simplified using $x = -\frac{E_\alpha}{RT}$, and hence

$$g(\alpha) = \int_0^\alpha \frac{d\alpha}{f(\alpha)} = \frac{A_\alpha E_\alpha}{\beta R}\int_0^\infty \frac{e^{-x}}{x^2}\, dx \qquad (\mathbf{3.7})$$

taking $p(x) = \int_0^\infty \frac{e^{-x}}{x^2}\, dx$, eq (3.7) becomes

$$g(\alpha) = \frac{A_\alpha E_\alpha}{\beta R} p(x) \qquad (\mathbf{3.8})$$

An umber of isoconversional methods have been used in literature for solving eq (3.8) (Vyzovkin et al, 2011a, Nassar et al, 2013). Here we followed the isoconversional equation of Kissinger-Akahira-Sunose (KAS) to estimate the effective activation energies (E_α) needed for the oxidation of Q65 and asphaltenes. This method an approximate function for *p(x)*, where $p(x) \cong e^{-x}/x^2$. Thus, after introducing the *p(x)* and performing some rearrangement, eq (3.8) becomes:

$$ln\left(\frac{\beta_i}{T_{\alpha,i}^2}\right) = \ln\left(-\frac{A_\alpha R}{E_\alpha}\right) - \ln g(\alpha) - \left(\frac{E_\alpha}{RT_{\alpha,i}}\right) \qquad (\mathbf{3.9})$$

Therefore, the effective activation energy can be estimated from the plot of the left side of Eq. (3.9) against $1/T_{a,i}$ at constant α for β_i, where the slope of the best-fit-line equals $-E_\alpha/R$.

Figure 3.3a shows the estimated effective activation energy as a function of conversion. It is well known that a constant value of effective activation energy, at various values of α, is an indication of a single-step reaction, while a change of activation energy with an increase in α is an indication of a complex reaction mechanism (Vyazovkin, 2015). Clearly, the E_α profile in the figure shows that oxygen tend to initiate low activation energy reaction. The increasing of the activation energy shows a multi-step reaction mechanism (high temperature oxidation region), as different effective activation energies are obtained at various stages of the oxidation process (Moukhina, 2012, Vyazovkin et al., 2011b). At this context, E_α exhibited two distinct trends of variation. For low α region, E_α appears almost constant showing a single step reaction mechanism confirming cracking of olefin chain. During the region $\alpha = 0.35$ to 0.9, oxidative cracking of aromatic as well as formed coke is occurring with gradual decrease in E_α, an indication that the presence of oxygen at high temperature alters the reaction mechanism and facilitates its rate (Chenoweth et al., 2008). It is worth to mention here that for the original Q-65, E_α were not estimated due to the overlapping of the conversion profiles at different heating rates (See Appendix A.1)

However, the presence of the NiO nanoparticles shows significant effect on the activation energy as shown in Figure 3.3a since all NiO nanosizes show lower effective activation energies.

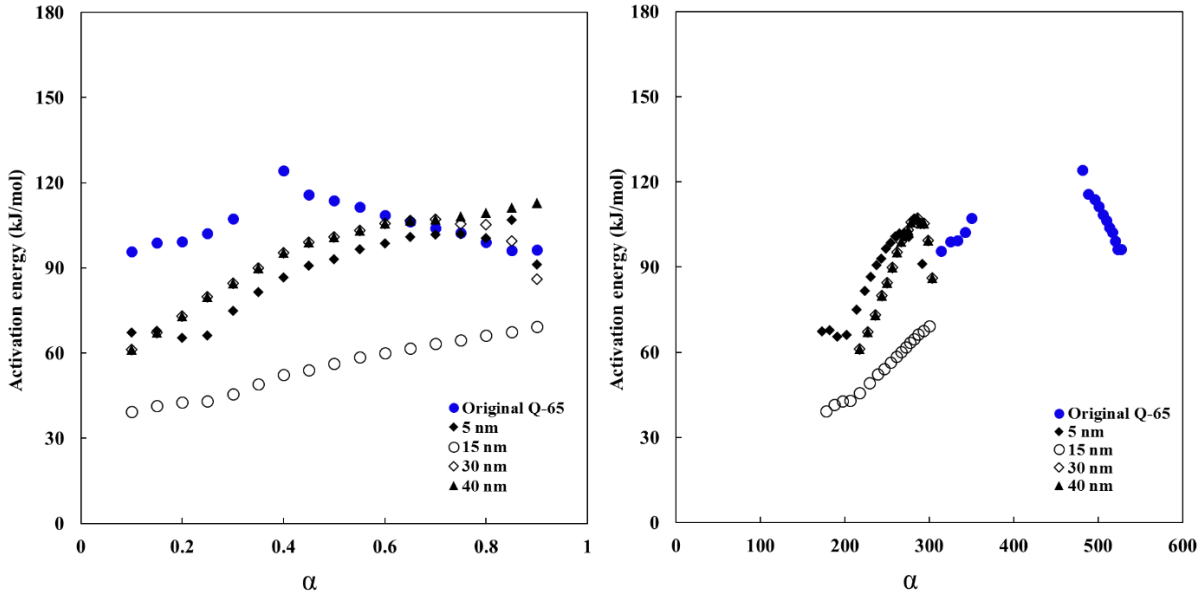

Figure 3.3 Dependencies of E_α on: a) α and b) temperature, for thermo-oxidative decomposition of Q-65 in presence and absence of NiO nanoparticles studied by thermogravimetry in air. Heating rate 5°C/min and air flow 100 cm^3/min.

It is also shown that the second step of the adsorbed Q-65 starts at α= 0.28 which is the end of the olfenic chain oxidation level. Due to the different adsorption coordinations of the adsorbed Q-65 speices, the effective activation energy shows different tren. However, due to their different surface morphology 15 nm shows higher adsorption affinity than 5 and 40 nm and close 30 nm, which is helping the reaction to initiate at lower E_α. These findings show agreement with Nassar et al. study that states the higher the adsorption affinity, the higher the catlytic activity (Nassar et al., 2014).

As seen in Figure 3.3b for the dependency of activation energy on temperature, the main differences between theQ-65 adsorbed NiO nanoparticles and original Q-65 are observed at the initial and final thermal oxidation stages. The small nanoparticles 5 nm and 15 nm shows faster catalytic processing starting at 165 and 175 °C and finishing at 270 °C and 300 °C, respectively.

While the the bigger nanoparticles 30 and 40 nm start at 240 C° and finish at 315 C°. These findings show good agreement with CO_2 evolved gas analysis that smaller the nanosize 5 nm is the faster the oxidation. This shows good agreement with the MS CO_2 detection results, since the smaller sizes start and finish earlier than the bigger sizes.

3.4.3 Estimation of pre-exponential factor (A_α)

The general equation of Sestak and Berggren (Šesták and Berggren, 1971) was employed here to determine the reaction mechanism and calculate the reaction order and pre-exponential factor from the previously determined effective activation energies. Accordingly, upon considering different reaction model as proposed by Sestak and Berggren (Šesták and Berggren, 1971)

$$g(\alpha) = \alpha^m(1-\alpha)^n(-\ln(1-\alpha))^p \qquad (\mathbf{3.10})$$

where, m, n, and p are constants for a particular model. Therefore, by assigning certain values to these three terms, any mathematical model can be generated. By plotting $\ln(g(\alpha))$ against $ln\left(\frac{\beta_i}{T_{\alpha,i}^2}\right)$ following eq (3.9), and using a linear regression of the least squares method, the most probable reaction mechanism is determined (See Appendix A.2). If the considered reaction mechanism complies with the specified $g(\alpha)$ function, then the linear correlation coefficient of the best-fit-line (R^2) should be close to 1.0 and the slope close to −1.0 (Nassar et al. 2014). T_p was chosen at α = 0.6 at a heating rate 5°C/min, for the calculation of most probable mechanism functions following the procedure of previous work (El-Qanni et al., 2016, Hashemi et al., 2014a). For this, α was obtained at specified Tp for all three heating rates (i.e., 5, 10 and 20 ^oC/min) of each sample (original Q-65 and Q-65 adsorbed on NiO nanoparticles. The results are shown in Table 3.2. The results shown in Table 3.2 suggesting the most probable mechanism of original Q-65 oxidation to be three quarters order mechanism function, while 5 nm shows one and half order mechanism and

the other sizes shows second order reaction mechanisms. This shows that different-nanosized NiO have different reaction mechanisms and pathways towards Q-65 oxidation confirming the different particle size effect of NiO nanoparticles.

Table 3.2 Most probable mechanism functions, slopes, and the linear regression coefficients at α= 0.6 at heating rate 5 °C/min.

	Function	***g*(*α*)**	***f*(*α*)**	**R^2**	**Slope**
Original Q-65	Three-quarters	$1-(1-\alpha)^{1/4}$	$4(1-\alpha)^{3/4}$	0.89	-0.91
5 nm	One and a half order	$(1-\alpha)^{-1/2}-1$	$2(1-\alpha)^{3/2}$	0.95	-0.89
15 nm	Second order	$(1-\alpha)^{-1}-1$	$(1-\alpha)^2$	0.89	-0.88
30 nm	Second order	$(1-\alpha)^{-1}-1$	$(1-\alpha)^2$	0.93	-0.95
40 nm	Second order	$(1-\alpha)^{-1}-1$	$(1-\alpha)^2$	0.96	-0.95

The increase in the reaction order with the presence of NiO could be attributed to an increase in the reaction rate due to the existence of these nanoparticles (Fogler, 2006).

After calculating the effective activation energies and the most probable mechanism function, the pre-exponential factor (A_α) is estimated from the intercept of the best-fit-line of the plot of $ln\left(\frac{\beta_i}{T_{\alpha,i}^2}\right)$ against $\frac{1}{T_{\alpha,i}}$, where the intercept equals $\ln\left(-\frac{A_\alpha R}{g_\alpha E_\alpha}\right)$ as per eq (3.9). The obtained pre-exponential factors are shown in Figure 3.4a with conversion and Figure 3.4b with the temperature. As seen, to some extent, the A_α trend followed that of the activation energy, especially in the high temperature oxidation zone. This can be explained by the fact that the pre-exponential factor reflects the nature of the transition state. In other words, a loose transition state will convey a higher A_α value. Because of the different types of transition states involved in the Q-65 thermal oxidation, the changes in A_α values can be rationalized.

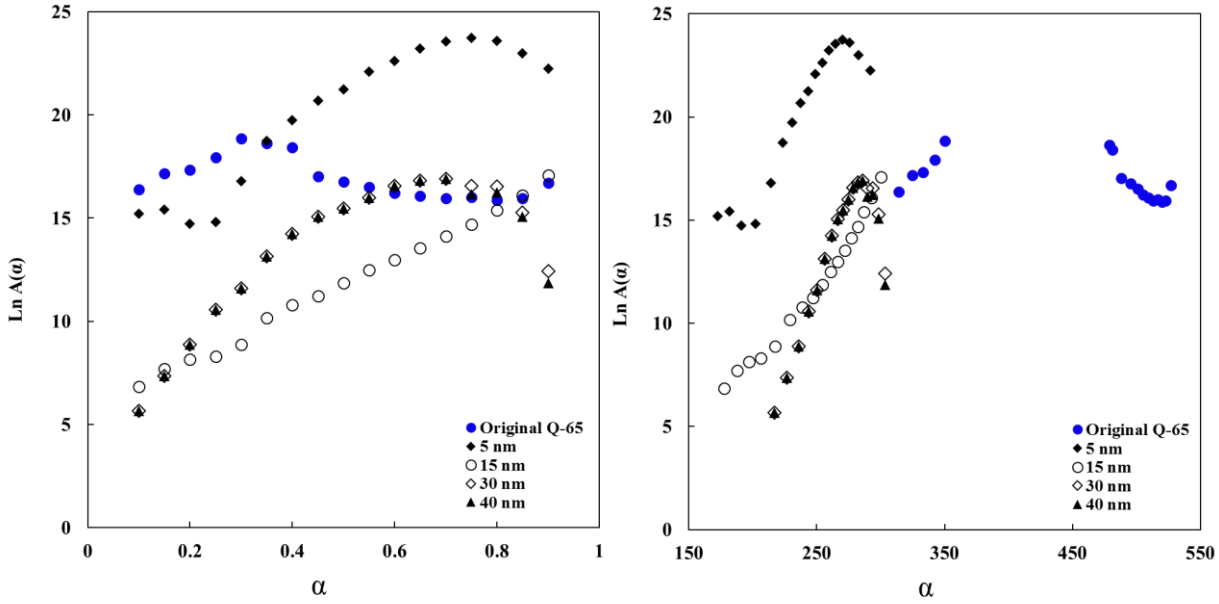

Figure 3.4 Dependencies of A_α: a) α and b) on temperature, for thermo-oxidative decomposition of Q-65 in presence and absence of NiO nanoparticles studied by thermogravimetry in air. Experimental conditions: heating rate = 5 ºC/min; air flow, 100 cm^3/min.

Moreover, the increasing of A_α suggesting an increase of the reaction rate. From Figure 3.4a it is shown that 5 nm has the highest A_α values indicating higher catalytic activity and this agree with TGA-MS analysis in Section 3.4.2. However, the lower values of A_α in the presence of the other sizes could be explained due to the interaction between the nanoparticles and the volatile products of the oxidation process (Mofokeng and Luyt, 2015). Looking at Figure 3.4b we can easily notice that the smaller nanoparticles 5 nm followed by 15 nm start the oxidation process earlier than 30 and 40 nm, supporting the fact that the smaller nanosizes the faster the oxidation, the better the catalyst. This agrees with the results of mass loss, CO_2 production profile and the activation energy trends.

The previous kinetic triplets E_α, A_α and $f(\alpha)$, examine and allow meaningful comparisons of the catalytic activity of the different-sized nanoparticle, in addition to the CO_2 production profile. It is

clearly noticed that the activation energy is not the only reason neither the only explanation for the different catalytic behaviours that been presented.

As seen, even with the fact that the effective activation energy of Q-65 thermo-oxidative decomposition is the main reason that determines that catalytic activity of nanoparticles; it is not the only reason. Catalytic activity of the nanoparticles, or the change in reaction rate and pathway can be associated with a change in the preexponential factor. Therefore, engaged together, the kinetic triplets, namely E_α, A_α and $f(\alpha)$ can provide a kinetic prediction and subsequently catalytic activity of nanoparticles. Furthermore, the thermogravimetric analysis with the associated gas analysis, could give a solid evidence of the catalyst behavior.

3.4.4 Estimation of thermodynamic transition state parameters

The thermodynamic parameters of the transition state functions, namely, changes in Gibbs free energy of activation ($\Delta G^{\ddagger}$), enthalpy of activation ($\Delta H^{\ddagger}$), and entropy of activation ($\Delta S^{\ddagger}$) were estimated to measure the extent of catalytic oxidation of different-sized NiO nanoparticles on the oxidation of Q-65. These thermodynamics parameters were estimated at the Tp that corresponds to α = 60% at a heating rate 5 ˚C/min as follows (Atkins and Paula, 2006, Nassar et al., 2014):

$$\Delta G^{\ddagger} = \Delta H^{\ddagger} - Tp\Delta S^{\ddagger} \qquad (\mathbf{3.11})$$

$$\Delta H^{\ddagger} = {E_p}^{\ddagger} - RTp \qquad (\mathbf{3.12})$$

$$\Delta S^{\ddagger} = R\, ln\left(\frac{A_P h}{e\kappa k_B Tp}\right) \qquad (\mathbf{3.13})$$

where ${E_p}^{\ddagger}$ is the activation energy and A_P is the pre-exponential factor, e is the Neper number (=2.7183), κ is the transmission coefficient (≈1.0), k_B is the Boltzmann's constant (=1.3806 × 10^{-23} J/K), h is the Planck's constant (=6.6261 × 10^{-34} Js), and R is the universal ideal gas constant

(=8.314 J/mol K). The results of these parameters are shown in Table 3.3. As observed for all cases, $\Delta S^{\ddagger}$ values are negative which means that the activated state is less disordered compared to the Q-65, also shows entropy of the initial product at the transition state, is lower than that of the reactants (Nassar et. al, 2014, Badran et al., 2016).

Table 3.3 Values of $\Delta S^{\ddagger}$, $\Delta H^{\ddagger}$, and $\Delta G^{\ddagger}$ for the thermos-oxidative decomposition of Q-65 in the presence and absence of nanoparticles at α = 60%.

	Tp (K)	$\Delta S^{\ddagger}$ $(\mathbf{J/mol\ K})$	$\Delta H^{\ddagger}$ $(\mathbf{kJ/mol})$	$\Delta G^{\ddagger}$ $(\mathbf{kJ/mol})$
Original Q-65	778	-126	102	200
5 nm	527	-69	94	131
15 nm	540	-150	55	137
30 nm	552	-121	82	148
40 nm	554	-123	80	151

The positive values of $\Delta G^{\ddagger}$ indicate that the oxidation processes are not spontaneous and not favorable. Also looking to the exact values of $\Delta G^{\ddagger}$ at different nanosizes, one can notice that adsorbed Q-65 oxidation with the different sizes are lower than the origin Q-65, indicating the catalytic effect of NiO nanoparticles. However, 5 nm is shows the lowest $\Delta G^{\ddagger}$ value suggesting more favorable reaction than the original Q-65 with and without the other nanosizes. The $\Delta H^{\ddagger}$of the original Q-65 seems to have the higher value, while the oxidation process with presence of NiO seems to have lower values, decreasing with the increase of nanoparticle sizes. This could be endorsed to the presence of NiO nanoparticles which caused a drop in the values of the thermodynamic parameters, and hence the promising catalytic effect of NiO nanoparticles is confirmed.

The activation enthalpy, $\Delta H^{\ddagger}$ for all nanosizes is less than that of Q-65. However, the values of $\Delta H^{\ddagger}$ of the nanosizes are very close to each other, but still less than that of Q-65, indicating different reaction paths with lower energy needed for the reaction.

3.4.5 Regeneration

Table 3.2 shows the average crystalline domain sizes, the BET surface areas and the amount of Q-65 adsorbed on the four tested different nano-sized NiO nanoparticle. As seen, three of the tested nanoparticles, i.e. 15, 30 and 40 nm, demonstrated their abilities to be regenerated and reused (at least twice) without affecting their original properties. The average crystalline domain sizes, the BET surface area and the Q-65 adsorbed quantities remain similar after using them for the first time and regenerating and using them two more times making them promising adsorbent-catalysts for removal of heavy hydrocarbons and oxidation of them.

Table 3.4 NiO nanosizes regeneration characteristics

	Average crystal size (nm)			**BET (m^2/g)**			**Q (molecule/nm^2)**		
	Original	**Cycle 1**	**Cycle 2**	**Original**	**Cycle 1**	**Cycle 2**	**Original**	**Cycle 1**	**Cycle 2**
5 nm	4.6	14.2	16.2	158	43	40	0.2055	0.9891	0.9909
15 nm	13.2	15.4	16.4	42	40	41	1.0065	1.0080	0.9915
30 nm	27	27.4	26	17	19	16	0.4654	0.4371	0.4141
40 nm	39.4	38.2	37.9	11	12	11	0.8084	0.8190	0.8034

In the case of the sample with original size of 5 nm, its preparation was carried out by careful dehydroxylation of $Ni(OH)_2$ at 300 °C for 2 h (Marei et al., 2016), but the oxidation reaction of the adsorbed Q-65 was carried out by increasing the temperature to 500 °C with ramp of 5 °C/min with presence of air. Hence, an increase in the average crystalline domain size for this case is expected, as the temperature of reaction was higher than the preparation temperature of this

nanoparticles. We demonstrated in our earlier study (Marei et al., 2016) that at 450 °C for 2 h in air we can produce a material with twice the average crystalline domain size (15 nm); however, under the oxidation reaction at 500 °C the particle growth was larger (15 nm). Oxidation reactions are exothermic reactions, and thus, this additional heat seemed to be enough in our studied conditions to mimic the production of the 15 nm nanoparticles that required 450 °C for their production in pure air. The higher density of –OH groups together with the extra heat from the oxidation reaction seem to induce the production of the 15 nm nanoparticles. After this size is produced under the oxidation reaction, then, the behavior is similar to the 15 nm particle that was prepared at 450 °C. This result indicates that the local released heat during the oxidations in the other nanoparticles did not affect the properties as they were already in structural equilibrium under the studied reaction conditions.

3.5 Conclusions

In this study, the effect of nanosize of NiO nanoparticles on catalytic thermo-oxidative decomposition of adsorbed Q-65 was investigated using TGA/DTA and TGA-MS systems to get the rate of mass loss, heat flow and CO_2 evolution profiles.

Kissinger-Akahira-Sunose (KAS) was used to describe the oxidation mechanism and to confirm the validity of the catalytic effect of the different-sized NiO nanoparticles by giving a valid prediction of the kinetic triplets, (i.e., the effective activation energy (E_α), the pre-exponential factor (A_α) and the reaction function *f(α)*. The rate of mass loss and CO_2 evolution profiles combined with the kinetic triplets as well as the transitional thermodynamic parameters, namely $\Delta S^{\ddagger}$, $\Delta H^{\ddagger}$, and $\Delta G^{\ddagger}$ shown the different behavior of different NiO nanosize on the catalytic thermo-oxidative decomposition of adsorbed the Q-65. It was noticed that the smaller nanosize 5 nm has the faster oxidative ability (faster CO_2 production) followed by the bigger nanoparticles 15, 30 and 40 nm, respectively.

Moreover, the reusability of the different-sized nanoparticles was tested by oxidizing the adsorbed Q-65 with TGA. Also XRD and BET have been used to characterize the regenerated nanocatalysts. The study showed the stability of NiO nanoparticles at different regeneration cycles without affecting its properties, except the 5 nm which its size increased to 15 nm in the first cycle, but it did not change in the second cycles, and that's due its original preparation procedure at lower temperature.

This piece of works shows the role of nanosize in post-adsorption catalytic thermo-oxidative decomposition of Q-65. This study expands our understanding of the metal-based nanoparticles properties in heavy oil applications.

3.6 References

CHEMDRAW V14 STRUCTURAL DRAWING SOFTWARE, in: CambridgeSoft Corporation, a subsidiary of PerkinElmer, Inc, 2014.

ADAMS, J. J. 2014. Asphaltene Adsorption, a Literature Review. Energy & Fuels, 28, 2831-2856.

ALIZADEH-GHESHLAGHI, E., SHAABANI, B., KHODAYARI, A., AZIZIAN-KALANDARAGH, Y. & RAHIMI, R. 2012. Investigation of the catalytic activity of nano-sized CuO, Co_3O_4 and $CuCo_2O_4$ powders on thermal decomposition of ammonium perchlorate. Powder Technology, 217, 330-339.

ATKINS, P. & PAULA, J. 2006. Atkin's Physical Chemistry, Oxford, Oxford University Press.

BADRAN, I., NASSAR, N. N., MAREI, N. & HASSAN, A. 2016. Theoretical and thermogravimetric study of the thermo-oxidative decomposition of Quinolin-65: an asphaltene model molecule. Fuel (Under Review).

BARTHOLOMEW, C. H. 2001. Mechanisms of catalyst deactivation. Applied Catalysis A: General, 212, 17-60.

CAMPBELL, C. T. 2013. The Energetics of supported metal nanoparticles: Relationships to sintering rates and catalytic activity. Accounts of Chemical Research, 46, 1712-1719.

CHENOWETH, K., VAN DUIN, A. C. & GODDARD, W. A. 2008. ReaxFF reactive force field for molecular dynamics simulations of hydrocarbon oxidation. The Journal of Physical Chemistry A, 112, 1040-1053.

CLARK, J. 2000. Calculations in A-level Chemistry, Harlow, United Kingdom, Pearson Education Limited.

COATS, A. W. & REDFERN, J. P. 1964. Kinetic Parameters from Thermogravimetric Data. Nature, 201, 68-69.

DEVARD, A., PUJRO, R., DE LA PUENTE, G. & SEDRAN, U. 2012. hydrocarbon yield structure in the conversion of heavy model molecules (Quinolin-65) on fluidized catalytic cracking catalysts. Energy & Fuels, 26, 5015-5019.

EL-QANNI, A., NASSAR, N. N., VITALE, G. & HASSAN, A. 2016. Maghemite nanosorbcats for methylene blue adsorption and subsequent catalytic thermo-oxidative decomposition: Computational modeling and thermodynamics studies. Journal of Colloid and Interface Science, 461, 396-408.

ESFANDYARI BAYAT, A., JUNIN, R., SAMSURI, A., PIROOZIAN, A. & HOKMABADI, M. 2014. Impact of metal oxide nanoparticles on enhanced oil recovery from limestone media at several temperatures. Energy & Fuels, 28, 6255-6266.

ESPENSON, J. H. 2002. Chemical kinetics and reaction mechanisms, McGraw-Hill.

FEI GUO, C., SUN, T., CAO, F., LIU, Q. & REN, Z. 2014. Metallic nanostructures for light trapping in energy-harvesting devices. Light Sci Appl, 3, e161.

FRANCO, C. A., NASSAR, N. N., MONTOYA, T., RUÍZ, M. A. & CORTÉS, F. B. 2015. Influence of asphaltene aggregation on the adsorption and catalytic behavior of nanoparticles. Energy & Fuels, 29, 1610-1621.

FRANCO, C. A., NASSAR, N. N., RUIZ, M. A., PEREIRA-ALMAO, P. & CORTÉS, F. B. 2013. Nanoparticles for inhibition of asphaltenes damage: adsorption study and displacement test on porous media. Energy & Fuels, 27, 2899-2907.

FRANKE, M. E., KOPLIN, T. J. & SIMON, U. 2006. Metal and metal oxide nanoparticles in chemiresistors: Does the nanoscale matter? Small, 2, 36-50.

FOGLER, H. S. 2006. Elements of Chemical Reaction Engineering, Prentice Hall PTR.

GUZMÁN, J. D., BETANCUR, S., CARRASCO-MARÍN, F., FRANCO, C. A., NASSAR, N. N. & CORTÉS, F. B. 2016. Importance of the adsorption method used for obtaining the nanoparticle dosage for asphaltene-related treatments. Energy & Fuels.(In press)

HAMMER, B. & NØRSKOV, J. K. 2000. Theoretical surface science and catalysis-calculations and concepts. Advances in Catalysis. Academic Press.

HASHEMI, R., NASSAR, N. N. & PEREIRA-ALMAO, P. 2012. Transport behavior of multimetallic ultradispersed nanoparticles in an oil-sands-packed bed column at a high temperature and pressure. Energy & Fuels, 26, 1645-1655.

HASHEMI, R., NASSAR, N. N. & PEREIRA ALMAO, P. 2013. Enhanced heavy oil recovery by in situ prepared ultradispersed multimetallic nanoparticles: A study of hot fluid flooding for Athabasca bitumen recovery. Energy & Fuels, 27, 2194-2201.

HASHEMI, R., NASSAR, N. N. & PEREIRA ALMAO, P. 2014a. In situ upgrading of Athabasca bitumen using multimetallic ultradispersed nanocatalysts in an oil sands packed-bed column: Part 2. Solid analysis and gaseous product distribution. Energy & Fuels, 28, 1351-1361.

HASHEMI, R., NASSAR, N. N. & PEREIRA ALMAO, P. 2014b. Nanoparticle technology for heavy oil in-situ upgrading and recovery enhancement: Opportunities and challenges. Applied Energy, 133, 374-387.

HASSAN, A., CARBOGNANI-ARAMBARRI, L., NASSAR, N. N., VITALE, G., LOPEZ-LINARES, F. & PEREIRA-ALMAO, P. 2015. Catalytic steam gasification of n-C_5 asphaltenes by kaolin-based catalysts in a fixed-bed reactor. Applied Catalysis A: General, 507, 149-161.

HASSAN, A., LOPEZ-LINARES, F., NASSAR, N. N., CARBOGNANI-ARAMBARRI, L. & PEREIRA-ALMAO, P. 2013. Development of a support for a NiO catalyst for selective adsorption and post-adsorption catalytic steam gasification of thermally converted asphaltenes. Catalysis Today, 207, 112-118.

HENRY, C. R., CHAPON, C., GIORGIO, S. & GOYHENEX, C. 1997. Size Effects in Heterogeneous Catalysis. In: LAMBERT, R. M. & PACCHIONI, G. (eds.) Chemisorption and reactivity on supported clusters and thin films: towards an understanding of microscopic processes in catalysis. Dordrecht: Springer Netherlands.

HOSSEINPOUR, N., KHODADADI, A. A., BAHRAMIAN, A. & MORTAZAVI, Y. 2013. Asphaltene adsorption onto acidic/basic metal oxide nanoparticles toward in situ upgrading of reservoir oils by nanotechnology. Langmuir, 29, 14135-14146.

JADE V 7.5.1 XRD, P. P. I. Q., MATERIALS DATA INC. 2005.

JAIN, P. K., HUANG, X., EL-SAYED, I. H. & EL-SAYED, M. A. 2008. Noble metals on the nanoscale: Optical and photothermal properties and some applications in imaging, sensing, biology, and medicine. Accounts of Chemical Research, 41, 1578-1586.

KAMRAN AKBARZADEH, A. H., ABDEL KHARRAT, DAN ZHANG, STEPHAN ALLENSON, JEFFERSON CREEK, SHAH KABIR, A. JAMALUDDIN, ALAN G. MARSHALL, RYAN RODGERS, OLIVER C. MULLINS, TROND SOLBAKKEN 2007. Asphaltenes-problematic but rich in potential. Oil Field Review, 22-43.

KHAING OO, M. K., CHANG, C.-F., SUN, Y. & FAN, X. 2011. Rapid, sensitive DNT vapor detection with UV-assisted photo-chemically synthesized gold nanoparticle SERS substrates. Analyst, 136, 2811-2817.

KHOOBI, M., DELSHAD, T. M., VOSOOGHI, M., ALIPOUR, M., HAMADI, H., ALIPOUR, E., HAMEDANI, M. P., SADAT EBRAHIMI, S. E., SAFAEI, Z., FOROUMADI, A. & SHAFIEE, A. 2015. Polyethyleneimine-modified superparamagnetic Fe_3O_4 nanoparticles: An efficient, reusable and water tolerance nanocatalyst. Journal of Magnetism and Magnetic Materials, 375, 217-226.

KIM, D. S. & KWAK, S.-Y. 2007. The hydrothermal synthesis of mesoporous TiO_2 with high crystallinity, thermal stability, large surface area, and enhanced photocatalytic activity. Applied Catalysis A: General, 323, 110-118.

LÓPEZ-LINARES, F., CARBOGNANI, L., GONZÁLEZ, M. F., SOSA-STULL, C., FIGUERAS, M. & PEREIRA-ALMAO, P. 2006. Quinolin-65 and violanthrone-79 as model molecules for the kinetics of the adsorption of C_7 athabasca asphaltene on macroporous solid surfaces. Energy & fuels, 20, 2748-2750.

LUO, X., MORRIN, A., KILLARD, A. J. & SMYTH, M. R. 2006. application of nanoparticles in electrochemical sensors and biosensors. Electroanalysis, 18, 319-326.

MAREI, N. N., NASSAR, N. N. & VITALE, G. 2016. The effect of the nanosize on surface properties of NiO nanoparticles for the adsorption of Quinolin-65. Physical Chemistry Chemical Physics, 18, 6839-6849.

MASCIANGIOLI, T. & ZHANG, W.-X. 2003. peer reviewed: environmental technologies at the nanoscale. Environmental Science & Technology, 37, 102A-108A.

MOFOKENG, J. P. & LUYT, A. S. 2015. Morphology and thermal degradation studies of melt-mixed poly(lactic acid) (PLA)/poly(ε-caprolactone) (PCL) biodegradable polymer blend nanocomposites with TiO2 as filler. Polymer Testing, 45, 93-100.

MOUKHINA, E. 2012. Determination of kinetic mechanisms for reactions measured with thermoanalytical instruments. Journal of Thermal Analysis and Calorimetry, 109, 1203-1214.

NASSAR, N. 2012. Iron oxide nanoadsorbents for removal of various pollutants from wastewater: An Overview In: BHATNAGAR, A. (ed.) Application of Adsorbents for Water Pollution Control. Portugal: Bentham e Books.

NASSAR, N. N., FRANCO, C. A., MONTOYA, T., CORTÉS, F. B. & HASSAN, A. 2015. Effect of oxide support on Ni-Pd bimetallic nanocatalysts for steam gasification of n-C_7 asphaltenes. Fuel, 156, 110-120.

NASSAR, N. N., HASSAN, A., LUNA, G. & PEREIRA-ALMAO, P. 2013. Kinetics of the catalytic thermo-oxidation of asphaltenes at isothermal conditions on different metal oxide nanoparticle surfaces. Catalysis Today, 207, 127-132.

NASSAR, N. N., HASSAN, A. & PEREIRA-ALMAO, P. 2011a. Application of nanotechnology for heavy oil upgrading: catalytic steam gasification/cracking of asphaltenes. Energy & Fuels, 25, 1566-1570.

NASSAR, N. N., HASSAN, A. & PEREIRA-ALMAO, P. 2011b. Effect of surface acidity and basicity of aluminas on asphaltene adsorption and oxidation. Journal of Colloid and Interface Science, 360, 233-238.

NASSAR, N. N., HASSAN, A. & PEREIRA-ALMAO, P. 2011c. Effect of the Particle Size on Asphaltene Adsorption and Catalytic Oxidation onto Alumina Particles. Energy & Fuels, 25, 3961-3965.

NASSAR, N. N., HASSAN, A. & PEREIRA-ALMAO, P. 2011d. Metal oxide nanoparticles for asphaltene adsorption and oxidation. Energy & Fuels, 25, 1017-1023.

NASSAR, N. N., HASSAN, A. & VITALE, G. 2014. Comparing kinetics and mechanism of adsorption and thermo-oxidative decomposition of Athabasca asphaltenes onto TiO_2, ZrO_2, and CeO_2 nanoparticles. Applied Catalysis A: General, 484, 161-171.

OZKAN, U. S. 2009. Design of heterogeneous catalysts, Wiley.

RASE, H. F. 2013. Fixed-bed reactor design and diagnostics: gas-phase reactions, Elsevier Science.

SCHNIPPERING, M., CARRARA, M., FOELSKE, A., KOTZ, R. & FERMIN, D. J. 2007. Electronic properties of Ag nanoparticle arrays. A Kelvin probe and high resolution XPS study. Physical Chemistry Chemical Physics, 9, 725-730.

ŠESTÁK, J. & BERGGREN, G. 1971. Study of the kinetics of the mechanism of solid-state reactions at increasing temperatures. Thermochimica Acta, 3, 1-12.

STRIZHAK, P. E. 2013. Nanosize effects in heterogeneous catalysis. Theoretical and Experimental Chemistry, 49, 2-21.

VLAEV, L., NEDELCHEV, N., GYUROVA, K. & ZAGORCHEVA, M. 2008. A comparative study of non-isothermal kinetics of decomposition of calcium oxalate monohydrate. Journal of Analytical and Applied Pyrolysis, 81, 253-262.

VYAZOVKIN, S. 2015. Isoconversional Kinetics of Thermally Stimulated Processes, Springer International Publishing.

VYAZOVKIN, S., BURNHAM, A. K., CRIADO, J. M., PÉREZ-MAQUEDA, L. A., POPESCU, C. & SBIRRAZZUOLI, N. 2011a. ICTAC Kinetics Committee recommendations for performing kinetic computations on thermal analysis data. Thermochimica Acta, 520, 1-19.

VYAZOVKIN, S. & DOLLIMORE, D. 1996. Linear and nonlinear procedures in isoconversional computations of the activation energy of nonisothermal reactions in Solids. Journal of Chemical Information and Computer Sciences, 36, 42-45.

WANKE, S. E. & FLYNN, P. C. 1975. The sintering of supported metal catalysts. Catalysis Reviews, 12, 93-135.

YOO, S. J., JEON, T.-Y., LEE, K.-S., PARK, K.-W. & SUNG, Y.-E. 2010. Effects of particle size on surface electronic and electrocatalytic properties of Pt/TiO_2 nanocatalysts. Chemical Communications, 46, 794-796.

ZHANG, W.-X. Nanoscale iron particles for environmental remediation: An Overview. Journal of Nanoparticle Research, 5, 323-332.

ZHOU, W. P., LEWERA, A., LARSEN, R., MASEL, R. I., BAGUS, P. S. & WIECKOWSKI, A. 2006. Size effects in electronic and catalytic properties of unsupported palladium nanoparticles in electrooxidation of formic acid. The Journal of Physical Chemistry B, 110, 13393-13398.

CHAPTER FOUR: NANOSIZE EFFECTS ON NiO NANOPARTICLES FOR ADSORPTION AND SUBSEQUENT THERMO-OXIDATIVE DECOMPOSITION OF VISBROKEN RESIDUE ASPHALTENES

This Chapter is adapted from the following manuscript:

MAREI, N. N., NASSAR, N. N., HOMUDAH, M., EL-QANNI, A., VITALE, G. & HASSAN, A. 2016. Nanosize Effects on NiO nanoparticles for adsorption and subsequent thermo-oxidative decomposition of visbroken residue asphaltenes. Submitted to Fuel, Elsevier.

4.1 Abstract

In this study, the nanosize effect of NiO nanoparticles on adsorption and post-adsorption catalytic oxidation of visbroken residue n-C_5 asphaltenes was investigated using a UV-Vis spectrophotometer and thermogravimetric analyzer coupled with mass spectrometer. Different-sized NiO nanoparticles with sizes between 5 and 80 nm were employed. Batch adsorption experiments were carried out for the considered asphaltene in toluene solutions, monitored via UV-vis spectrophotometry. The adsorption isotherms were described by the solid-liquid equilibrium (SLE) model. The findings showed that thermally cracked n-C_5 asphaltenes interact to different extents with different-sized NiO nanoparticles. On a normalized surface area basis, the amount of n-C_5 asphaltene adsorbed per nm^2 of NiO surface was the highest for NiO nanoparticles of size 80 nm; while 5 nm size NiO nanoparticles was the lowest. Thermogravimetric analysis of visbroken n-C_5 asphaltenes was also performed and the reaction products were probed by a mass spectrometer. Kissinger-Akahira-Sunose (KAS) was used to describe the oxidation mechanism and to confirm the validity of the catalytic effect of the different particle sizes of NiO nanoparticles. The catalytic activity comparison suggested that the smallest NiO nanoparticles has highest catalytic activity than the biggest NiO nanoparticles. These findings exhibit the significance of textural properties of nanoparticles during adsorption and thermal catalytic processing of asphaltenes.

4.2 Introduction

Heavy polar compounds, like asphaltenes, are responsible for many of the undesirable behaviors of crude oil (Adams, 2014, Akbarzadeh et al., 2007). These undesirable behaviors are more significant in heavy oil and bitumen since there exist higher percentages of heavy molecules in their atomic structure (Ortega et al., 2015). Actually, the presence of unstable polar heavy hydrocarbons like asphaltenes in the oil matrix would negatively influence the entire production chain, starting from the well where they can reduce oil recovery and consequently decrease the productivity index by changing reservoir wettability, rock pore plugging, and deposition of asphaltenes within wells (Pernyeszi et al., 1998, Hashemi et al., 2013, Hashemi et al., 2014a, Hashemi et al., 2014b, Spiecker et al., 2003a, Spiecker et al., 2003b). Hence, removing the unstable asphaltenes or finding an inhibitor to prevent or delay their precipitation is of paramount importance. High selectivity adsorption techniques, focusing mainly on the removal of asphaltenes rather than on the whole bitumen will considerably improve oil upgrading and recovery efficiency. Asphaltene adsorption onto traditional adsorbents has been widely reported in literature. Various solid surfaces have been employed for asphaltene adsorption; including metallic (Nassar et al., 2011b, Nassar et al., 2014), mineral (Marlow et al., 1987, Menon and Wasan, 1987, Bantignies et al., 1998, Gaboriau and Saada, 2001, Pernyeszi and Dékány, 2001), silica (Kumar et al., 2005, Acevedo et al., 2000, Saada et al., 1995), carbon (Sakanishi et al., 2004) and glass (Akhlaq et al., 1997). However, using the traditional adsorption process would result in massive solid waste hydrocarbons that need special treatment and/or disposal. Our alternative proposition is to separate the unstable, seed to coke formation, heavy polar hydrocarbons by adsorbing them onto a solid adsorbent-catalyst and, consequently, upgrade these heavy fractions into light utilizable distillates (Hassan et al., 2015).

To overcome the challenges of the unstable polar heavy hydrocarbons, the Nassar's at the University of Calgary have recently employed metal-based nanoparticles to improve the heavy oil quality through deasphalting with environmentally sound nanoadsorbents/catalysts (Franco et al., 2013a, Franco et al., 2013b, Franco et al., 2014, Nassar et al., 2011a, Nassar et al., 2011b, Nassar et al., 2011e, Nassar et al., 2014, Nassar et al., 2013b). Thus making this type of energy resource a better feedstock for refining and consequently reducing emissions (Hassan et al., 2013, Adams, 2014, Hashemi et al., 2014a, Hassan et al., 2015). This could be accomplished by separating the asphaltenes from oil through adsorbing them onto adsorbent-catalyst nanoparticles, which can subsequently promote the subsequent treatment process (e.g., oxidation, steam gasification, hydroprocessing, thermal cracking, etc) of the adsorbed species. We refer to this unique class of functional nanomaterials as "nanosorbcats" (El-Qanni et al., 2016). Deasphalting heavy oil through adsorption followed by catalytic treatment processes can provide a number of benefits. Firstly, as asphaltene hinders the transportation and processing of oil, this process will reduce the capital cost and increase process performance and efficiency. Secondly, catalytic processing (e.g., oxidation, steam gasification, hydroprocessing, thermal cracking, etc) will enhance asphaltene properties to form useable light distillates at significantly lower temperatures than the conventional processes (e.g., thermal cracking, coking, etc) (Hassan et al., 2015). Asphaltene adsorption onto different surfaces of metal oxide nanoparticles showed that the adsorption is strongly dependent on the type of nanoparticles (Nassar et al., 2014, Nassar et al., 2013a, Hosseinpour et al., 2013, Nassar et al., 2011c). For on-site application, these adsorbed asphaltenes could be converted into valuable commodity chemicals, like synthetic gas (Hassan et al, 2013, Hassan et al., 2015, Nassar et al., 2015a). For subsurface application, for the purpose of recovery enhancement, in-situ adsorption of asphaltenes within the well by nanoparticles has been demonstrated as a way to

upgrade oils to enhance liquid yields while reducing clogging of rock pores, viscosity, and formation damage (Adams, 2014).

Due to asphaltene complex chemical structure, polarizability and amphiphilic behavior, it exhibit a self–associating feature that promotes aggregation (Mittal and Shah, 2002, Prausnitz et al., 1998, Spiecker et al., 2003a, Spiecker et al., 2003b, Witthayapanyanon et al., 2008). Hence the use of classical adsorption isotherms such as Langmuir (Langmuir, 1918) and Freundlich (Freundlich, 1906) or even the Dubinin-Ashtakhov (DA) model based on the Polanyi theory (Polanyi, 1914) are not appropriate to describe the mechanism of the adsorption of auto–associative molecules such as asphaltenes, particularly at low loads and when considering a uniformly dense region at moderate loads. Therefore, we have recently developed a novel three-parameters solid-liquid equilibrium (SLE) model for describing the behavior of the adsorption of self-associating asphaltene molecules onto solid surfaces based on the self-association theory (Montoya et al., 2014). In addition to predict the adsorption affinity and capacity of asphaltenes onto the nanoparticle surfaces, this novel SLE model provides, at the macro level, insight into the extent of the asphaltene aggregates on the nanoparticle surface. This is very important as the changes in the colloidal state of asphaltenes can impact the catalytic activity of the nanoparticle surfaces after adsorption (Franco et al., 2013c). The catalytic activity of nanoparticles was typically confirmed on the basis of a shift in mass loss peak that is associated with an exothermic peak using thermogravimetric analysis, as well as the quality of the emitted gases during the catalytic steam gasification process or oxidation process (Hassan et al., 2015, Nassar et al., 2014, Franco et al., 2014, Nassar et al., 2013b, Franco et al., 2013b). This catalytic role of nanoparticles was further confirmed for other types of asphaltenes reported by other researchers (Mirzayi and Shayan, 2014, Hassan et al., 2013).

Using Quinolin-65 (Q-65) as a model-adsorbing compound for asphaltenes, recent study of our group has shown that the nanosize of NiO nanoparticles play significant role on their adsorption and catalytic behavior (Marei et al., 2016a, Marei et al., 2016b). This was attributed to the dramatic changes in surface properties, topology, morphology and textural properties of NiO nanoparticles upon undergoing down in the nanoscale.

This work continues our previous work and it aims at employing different-sized NiO nanoparticles for the adsorption and subsequent catalytic thermal cracking of visbroken (mild thermally cracked) *n*-C_5 asphaltenes. Visbroken asphaltenes were selected as representatives for the expected materials typically remained within partially depleted reservoirs exposed to thermal treatments (López-Linares et al., 2009, Ortega et al., 2015), like steam assisted gravity drainage. Hence, understanding the impact of the nanosize effect on the adsorption and subsequent catalytic decomposition of hydrocarbon fraction remaining after a production process is of primary importance not only in the upgrading scheme, but also for proper selection of feasible nanocatalysts for further processing of this material.

4.3 Experimental work

4.3.1 Materials

n-Pentane (99%) was used for asphaltene extraction and toluene HPLC grade was used as a solvent for heavy oil model solution preparation, both solvents are obtained from Sigma-Aldrich, Ontario. $Ni(NO_3)_2.6H_2O$ obtained from Sigma-Aldrich, Ontario and NaOH pellets obtained from VWR, Radnor, were used as precursors for NiO nanoparticle preparation. All chemicals were used as received without further purification. Solid visbroken n-C_5 asphaltenes extracted from Athabasca visbroken residue was used as representatives for the expected materials typically remained within partially depleted reservoirs exposed to thermal treatments.

4.3.2 NiO nanoparticles

NiO nanoparticles with nominal size ranges between 5 and 80 nm were prepared by the controlled thermal dehydroxylation of $Ni(OH)_2$, as described in our previous study (Marei et al., 2016). In brief, a specified amount of nickel nitrate ($Ni(NO_3)_2.6H_2O$) was dissolved in deionized water and, subsequently NaOH pellets was added pellet by pellet under magnetic stirring until a pH of 11 was attained to precipitate small nickel hydroxide particles ($Ni(OH)_2$). Then the precipitate was homogenized for 15 min and transferred to a tightly sealed polypropylene bottle and crystallized for 4 h at 100 °C in an oven. After crystallization, the product was filtered, washed with distilled water and dried for 12 h at 100 °C. The dried material was then calcinied with a ramp of 5 °C/min for 2-3 h at temperatures in the range of 300 to 700 °C to get different-sized NiO nanoparticles by controlling the calcination temperature and time. Table 4.1 shows the characteristics of the in-house prepared different-sized NiO nanoparticles.

Table 4.1 Characteristics of the selected different-sized NiO nanoparticles

Nominal size (nm)	5	10	15	20	30	40	60	80
Average crystal size (nm)	4.6	10.4	13.2	23.2	27	39.4	55	78.8
BET surface area (m^2/g)	158	58	42	20	17	11	7	3

Surface area of the nanoparticles was measured by the surface area and porosity analyzer (TriStar II 3020, Micromeritics Corporate, Norcross, GA) by performing N_2-physisorption at -196 °C. The samples were degassed at 150 °C under N_2 flow overnight before analysis. Surface areas were calculated using Brunauer–Emmet–Teller (BET) equation. An estimation of the particle size (assuming spherical particles) was accomplished by using the measured specific surface area BET and the derived equation $d = 6000/(SA \times \rho_{NiO})$; where d is the particle size in nm, SA is the experimentally measured specific surface area (m^2/g), and ρ_{NiO} is the NiO density (6.67 g/cm^3).

Dried powders of nanoparticles were characterized by X-ray diffraction using a Rigaku ULTIMA III X-ray diffractometer with Cu Kα radiation as the X-ray source. The scan was performed in the range 30–90º 2θ using a 0.02º step and a counting time of 1º/min. The crystalline domain sizes were measured using the Debye-Scherrer equation as implemented in the commercial software JADE (provided with the diffractometer), by calculating the full width at half-maximum (FWHM) of the peaks fitting the experimental profile to a pseudo-Voigt profile function.

To get further insights into the morphology and shape of the NiO nanoparticles used in this work, high resolution transmission electron microscopy (HRTEM) was carried out. A very small quantity of the powdered NiO samples were dispersed in pure ethanol. The HRTEM images were collected on a FEI Tecnai F20 FEG TEM using an accelerating voltage of 200 kV (See Figure S1 in Supporting Information). Small nanosizes (like 5, 10 and 15 nm) seem to be connected and aggregated forming rod-like morphology. In the case of the 20 and 30 nm size nanoparticle they seem to be formed of flat thin sheets connected to each other. On the other hand, for bigger

nanosizes, 40 nm sample looks like cylinders, the 60 nm sample are single thicker sheets and the 80 nm sample shown hexagonal shapes. Detailed NiO nanoparticle characteristics can be found in our previous study (Marei, et. al, 2016).

4.3.3 Preparation of visbroken residue n-C_5 asphaltenes

Solid n-C_5 asphaltenes were extracted from visbroken Athabasca vacuum residue which was twisted following standard procedures (ASTM D2892 and ASTM D5236) (Ortega et al., 2015). n-C_5 asphaltenes were isolated from the visbroken Athabasca vacuum residue by slowly pouring 300 g of sample fluidized at 100 °C into a 5 L round bottomed flask which is filled by 4 L of n-Pentane, while stirring was continuously applied. Elemental analyzer 2400 series *II* (Perkin Elmer, Canada) was used to quantify C, H and N content in the extracted n-C_5 asphaltenes. Elemental analysis revealed that the prepared visbroken n-C_5 asphaltenes have 80.4 wt% carbon, 6.5 wt% hydrogen, 4.2 wt% sulfur, 1.5 wt% nitrogen and 6.99 wt% oxygen.

4.3.4 Evaluation of NiO nanosizes as adsorbents and catalysts

4.3.4.1 Batch adsorption experiments

Adsorption experiments were performed at temperature of 25 ºC by preparing solutions of visbroken n-C_5 asphaltenes dissolved in toluene at different initial concentrations. Around 100 mg of each prepared NiO nanoparticles was placed in a set of 25-mL vials containing final volume of 10-mL solution of n-C_5 asphaltenes dissolved in toluene with different initial concentrations ranging from 5 to 4000 mg/L. The vials were sealed firmly to avoid toluene evaporation. Adsorption was allowed to take place by shaking the vials for 24 h on a Wrist Action shaker (Burrel, Model 75-BB) assuring that the equilibrium was attained. Then, the samples were allowed

to settle overnight. Afterwards, the supernatant was decanted and tested using Evolution™ 260 UV-Vis Spectrophotometer using toluene as a blank. The calibration curve was built at a wavelength of 289 nm. Selected experiments were spiked and repeated twice, to confirm their reproducibility. The adsorbed amount of n-C_5 asphaltenes, Q (mg/m^2), was calculated based on mass balance analysis as shown in eq (4.1).

$$Q = \frac{(C_0 - C_e)}{S_A m} V \qquad (\mathbf{4.1})$$

where C_0 is the initial concentration of n-C_5 asphaltenes in solution (mg/L), C_e is the equilibrium concentration of n-C_5 asphaltenes in the supernatant (mg/L), V is the solution volume (L), S_A is the BET surface area of the prepared NiO nanoparticles (m^2/g), and m is the mass of the nanoparticles (g).

4.3.4.2 Infrared spectroscopy (FTIR)

A Nicolet 6700 FT-IR instrument manufactured by Thermo Electron Corporation with a smart diffuse reflectance attachment to carry out diffuse reflectance infrared Fourier transform spectroscopy (DRIFTS) analysis was used to study the binding geometry and molecular bonds of the adsorbed visbroken n-C_5 asphaltenes and have an up-close view on the hydroxyl functional group region to have a deeper insight into n-C_5 asphaltene adsorption onto the different-sized NiO nanoparticles. Around 2.5 mg of the sample was mixed with 500 mg of KBr and the entire mixture was mounted in the DRIFTS sample holder. The spectra were recorded from 400 to 4000 cm^{-1} with a resolution of 2 cm^{-1} and each spectrum is the average of 128 scans.

4.3.4.3 Thermogravimetric Analysis (TGA)

TGA was carried out using a simultaneous thermogravimetric analysis/differential scanning calorimetry (TGA/DSC) analyzer (SDT Q600, TA Instruments, Inc., New Castle, DE). In a typical experiment, approximately 5 mg of dried NiO nanoparticle containing adsorbed n-C_5 asphaltenes were heated up at three different heating rates of 5, 10, and 20 °C/min in separate experiments. The airflow was kept at 100 cm^3/min during the experiments. The experiments were performed under ambient pressure. Evolved gas analysis (EGA) was also carried out by an online mass spectrometer (MS) (Pfeiffer Vacuum GSD 301 O_2, Omnistar, Deutschland) attached to the TGA/DSC system to detect CO_2 production. For EGA experiments, a sample mass of 10 mg, airflow of 30 cm^3/min and a heating rate of 10°C/min was used. The TGA instrument was calibrated for mass and heat changes using sapphire as a reference for the heat calibration and zinc as a reference for the temperature calibration.

4.4 Results and discussion

4.4.1 Adsorption isotherms

Adsorption isotherms of n-C_5 asphaltenes over different-sized NiO nanoparticles ranging between 5 and 80 nm were performed in a series of batch adsorption experiments. Figure 4.1 shows the experimental amount of n-C_5 asphaltenes adsorbed onto different-sized NiO nanoparticles at 25 ºC along with the solid–liquid-equilibrium (SLE) model. This model is based on the chemical theory, and thus, it enhances the understanding of asphaltene aggregation and interactions with the solid surface at equilibrium (Montoya et al., 2014, Nassar et al., 2015b, Franco et al., 2015). The model is expressed as:

$$C_E = \frac{\psi H}{1 + K\psi}\, exp\left(\frac{\psi}{q_m A}\right) \qquad (\mathbf{4.2})$$

where $\psi = \frac{-1+\sqrt{1+4K\xi}}{2K}$, $\xi = \left(\frac{q_m q}{q_m - q}\right) A$, and q (mg/m^2) and q_m (mg/m^2) are the amount of n-C_5 asphaltenes adsorbed onto the nanoparticles surface and the maximum adsorption capacity of the nanoparticles, respectively. A (m^2/mg) is the measured BET surface area per mass of nanoparticles and C_E (mg/g) is the equilibrium concentration of n-C_5 asphaltenes. The SLE parameters K (g/g) and H (mg/g) are the adsorption constants related to the degree of n-C_5 asphaltene self-association over the nanoparticles surface and the inverse of the common Henry's law constant related to the preference of the n-C_5 asphaltenes in the liquid or adsorbed phase, respectively (Montoya et al., 2014).

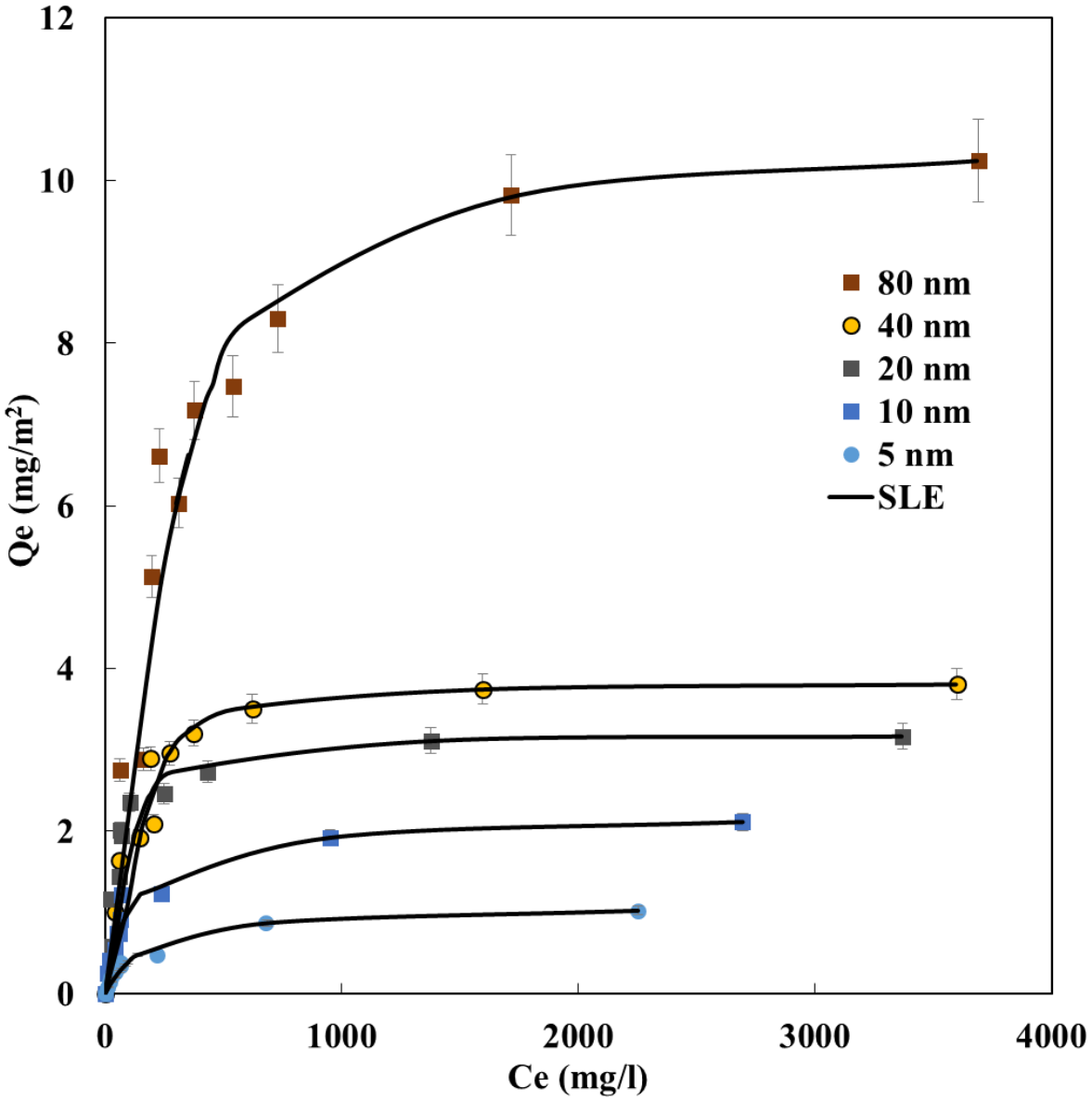

Figure 4.1 Adsorption isotherms of n-C_5 asphaltenes onto different-sized NiO nanoparticles. Nanoparticles dose: 10 g/L; shaking rate: 200 rpm; contact time: 24h and temperature: 25 °C.

The lower the *H* value, the higher the affinity of asphaltenes towards the adsorbed phase rather than the liquid phase. However, the degree of aggregation of the n-C_5 asphaltenes on the adsorption site is higher when *K* value increases. All SLE model parameters were estimated using DataFit

software program (version 8.2.79, Oakdale Engineering, Oakdale, PA, USA) and listed in Table 4.2.

Table 4.2 SLE isotherm parameters for the adsorption of n-C_5 asphaltenes over different-sized NiO nanoparticles at a temperature of 25 °C.

Particle Size (nm)	**SLE Model Parameters**			
	H (mg/g)	**K (g/g)**	**q_m (mg/m^2)**	χ^2
5	1.09	2.94	1.21	0.48
10	0.84	2.82	2.46	0.98
20	4.95	4.26	3.25	0.21
40	15.68	9.47	3.89	0.59
80	18.92	5.98	10.89	0.71

As seen in Figure 1, for all selected nanosizes, NiO succeeded in removing n-C_5 asphaltenes from the toluene based solutions with different degrees on both adsorption affinity and capacity, confirming the capability of NiO nanoparticles in removing asphaltenes molecules in the first place as also proven in many previous studies of our research group NiO (Nassar et al., 2011b, Nassar et al., 2011e, Franco et al., 2013b).

Despite the fact that adsorption is expressed by a normalized surface area basis, the largest particle size (80 nm) showed a higher adsorption capacity in comparison to the smaller different-sized NiO nanoparticles as indicated by the position of plateau in Figure 4.1 and the q_m value in Table 4.1. This indicates that the adsorption behavior of n-C_5 asphaltenes over different-sized NiO nanoparticles goes beyond the increase or decrease in the surface areas and involves other factors, such as dispersion ability, intrinsic reactivity, asphaltenes self-association and subsequent aggregation, and the nanoparticles surface topology and morphology (Marei et al., 2016, Nassar et al., 2011d).

Our findings here show that n-C_5 asphaltene adsorption increases with an increase in the size of NiO nanoparticles, showing the highest uptake for 80 nm and the lowest uptake for 5 nm,

indicating a significant effect of different-sized NiO nanoparticles on the adsorption capacity towards n-C_5 asphaltenes. This could be attributed to the different shapes and topologies that might be found when the particles size changes. In addition, it is well known that asphaltenes could be adsorbed onto surfaces as molecules, nano-aggregates, micelles, dimers and monomers (Mullins et al., 2012). The type and strength of the interactions between asphaltenes and surface sites depend on the orientation of various functional groups present in the structure of asphaltenes and its nano-aggregates and the chemistry of the adsorbent surfaces (Hmoudah et al., 2016, Nassar et al., 2012). The interaction between NiO nanoparticles surfaces with the heteroatoms (N, O, and S) exist in the n-C_5 asphaltenes might be attributed to hydrogen bonds, dispersion forces, induction forces, electrostatic forces, and the intermolecular π-π interactions in the solid film of n-C_5 asphaltenes (Spiecker et al., 2003a, Spiecker et al., 2003b, Witthayapanyanon et al., 2008) which would facilitate asphaltene interaction, nucleation and growth and enhance the subsequent formation of colloidal nanoaggregates (2-5 nm) in size (Acevedo et al., 2000, Mullins et al., 2012, Sheu et al., 2007). Thus, the bigger the particle size of NiO, the better relaxation of asphaltene molecules aggregates on the surface, taking into consideration its shape and morphology, resulting in higher uptake (Figure 4.1). Indeed, these results are in excellent agreement with the case of Q-65 model molecule selected to mimic asphaltenes to address the adsorption behavior of asphaltenes onto the same prepared different-sized NiO nanoparticles, not only experimentally but also computationally (Marei et al., 2016). Both studies confirm the importance of the nanoparticle surface topology and morphology on its adsorption of organic molecules (Marei et al., 2016). Thus, variations on adsorption behavior of different-sized NiO nanoparticles towards Q-65 and n-C_5 asphaltenes must then be expected.

To further understand the adsorption behavior, the experimental isotherm data are fitted to the SLE model as mentioned earlier. As previously seen in Figure 4.1 and indicated by the values of the non-linear Chi-square analyses (χ^2) in Table 1, the SLE model fits the experimental data well. The results in Table 1 also show that the adsorption capacity of different-sized NiO nanoparticles, represented by q_m, followed the order 80 nm >> 40 nm > 20 nm > 10 nm > 5 nm. While the differences in ranking the other SLE model parameters; H and K amongst the different-sized NiO nanoparticles can be credited to the different degree of interactions between the nanoparticle surface and the n-C_5 asphaltenes molecules or aggregates. Recalling the SLE model assumptions highlights that the adsorption process is mainly divided into three regions (Montoya et al., 2014); (i) the first region, which corresponds to low uptake; the adsorption will likely occur in the high-energy sites and n-C_5 asphaltenes molecules would be possibly adsorbed as monomers, (ii) the second region corresponds to medium uptake; the n-C_5 asphaltenes will form aggregates around the high-energy sites, and (iii) the last region corresponds to high uptake; in this region, it is assumed that the finite volume available for adsorption will become crowded with n-C_5 asphaltenes molecules, which are expected to be in the form of isomers, nanoaggregates, etc. However, one may ask: if the bigger nanoparticle sizes are better adsorbent, why do we need nanosize?. Well! NiO nanoparticles of 110 and 120 nm size were prepared and tested during this study. However, those big particles were unable to adsorb the asphaltenes molecules.

These findings can give an insight indication about the optimum size of NiO nanoparticles as nanoadsorbents. However, large n-C_5 asphaltenes aggregates might block some of the active sites of the nanoparticles, and, hence, they could impact the catalytic activity in the case of any catalytic application (Franco et al., 2015), especially the thermo-oxidative decomposition of the adsorbed

asphaltenes over NiO as nanocatalysts. Thus, a careful optimization should be considered when it comes in designing NiO as a solid nanosorbcats.

4.4.2 FTIR analysis for visbroken n-C_5 asphaltenes before and after adsorption on NiO nanoparticles

Figure 4.2 shows the infrared spectra of the used visbroken n-C_5 asphaltenes and the different-sized NiO nanoparticles before and after adsorption experiments. The spectra of pure different-sized NiO nanoparticles (Figure 4.2a) and visbroken n-C_5 asphaltenes (Figure 4.2b) are clearly different than the spectra of visbroken n-C_5 asphaltenes adsorbed onto different-sized NiO nanoparticles (Figure 4.2b) confirming the interactions by its adsorption. The infrared bands of the visbroken n-C_5 asphaltenes that are very clear in the region 1400 to 530 cm^{-1} in Figure 4.2b are no longer visible when n-C_5 asphaltenes were adsorbed onto different-sized NiO nanoparticles. On the other hand, the clear bands in the region of 2960 to 2850 cm^{-1} (Figure 4.2b) as well as of the framework region of the different-sized NiO nanoparticles (1690 to 510 cm^{-1} in Figure 4.2b) are modified by bands clearly corresponding to n-C_5 asphaltenes upon its adsorption onto different-sized NiO nanoparticles (bands around 2960 to 2850 cm^{-1} are assigned to C-H sp^3 stretching vibration, 1600-1400 and 1305 cm^{-1} are assigned to aromatic C=C stretching vibration, the bands around 1150 cm^{-1} are assigned to C-H in-plane stretching vibration, and the bands around 1690 to 1630 are assigned to carbonyl groups; C=O stretching vibration). Furthermore, the significant effect of different-sized NiO nanoparticles on adsorption towards visbroken n-C_5 asphaltenes can be clearly distinguished by looking at the O-H- bands (3650-3200 cm^{-1}) in both Figures 4.2a and b. As seen, when the nanosize get bigger (5 to 40 nm) the O-H- bands get flatter until almost disappeared in spectrum of 80 nm (Figure 4.2b), indicating more visbroken n-C_5 asphaltenes

attached to the surface of 80 nm, and thus, emphasizing the particle size effect and ensuring the highest uptake as seen previously in the adsorption isotherm (Figure 4.1).

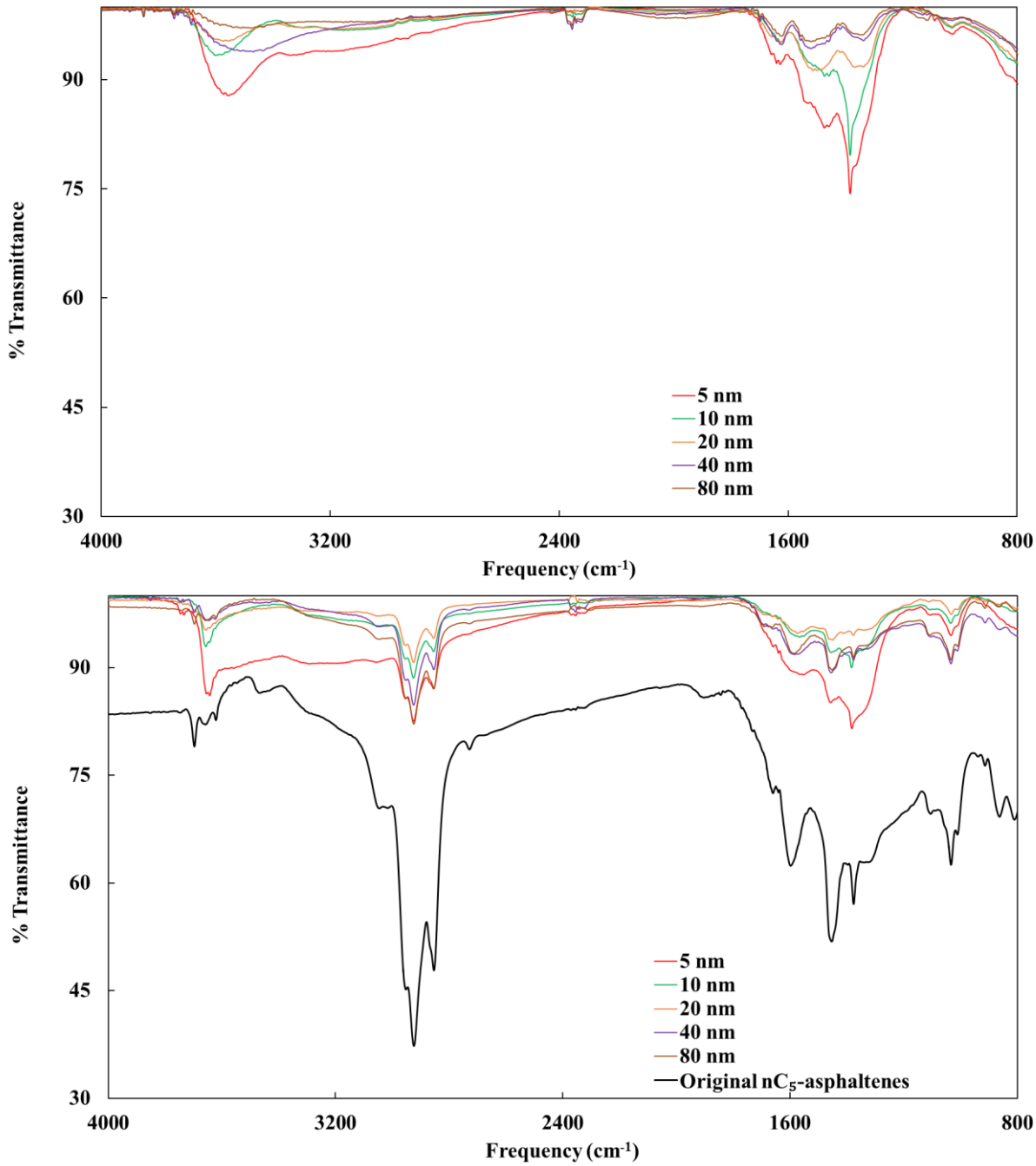

Figure 4.2 FTIR spectra for: (a) different-sized NiO nanoparticles, and (b) visbroken n-C_5 asphaltenes and the experimental adsorbed n-C_5 asphaltenes onto different-sized NiO nanoparticles.

4.4.3 TGA/DSC and gas evolution profiles

Figure 4.3a-d show the thermo-oxidative profiles for visbroken n-C_5 asphaltenes in air before and after adsorption over different-sized NiO nanoparticles obtained using online TG/DTA-MS. Figure 4.3a and b show the mass loss and heat flow profiles, respectively. Figure 4.3c shows the conversion (α) profile obtained from the mass loss data and Figure 4.3d shows the EGA obtained using online MS. As seen, oxidation of visbroken residue n-C_5 asphaltenes on its own occurs beyond 400°C. Rate of mass loss is maximum somewhere around 500°C (Figure 4.3a). The exothermic peak for the corresponding mass loss (Figure 4.3b) confirms the oxidation of visbroken n-C_5 asphaltenes. When adsorbed onto the NiO nanoparticle surface, the mass loss and heat flow peaks for visbroken n-C_5 asphaltene oxidation shifts to a lower temperature. This lowering of the oxidation temperature shows the catalytic effect of different-sized NiO nanoparticles. It is interesting to note that this lowering in oxidation temperature is also dependent on the particle size of the NiO nanoparticles. The smaller the particle size, the lower the oxidation temperature. Both the mass loss rate and heat flow show that the onset of oxidation on the smallest size 5 nm is at the lowest temperature followed by 10, 20, 40 and 80 nm. This means that the smaller the particle size the greater is the catalytic effect towards visbroken n-C_5 asphaltenes oxidation. Also, the conversion degree α (obtained from the mass loss data plotted in Figure 4.3a) was calculated as per eq 4.3 for each particle size in order to see the differences more clearly as shown in Figure 4.3c.

$$\alpha = \frac{m_o - m_t}{m_o - m_f} \qquad (\mathbf{4.3})$$

where, m_0, m_f and m_t are the initial sample mass, the sample mass at a given time and the final mass of the sample, respectively.

The conversion degree profile (Figure 4.3c) gives another evidence to the fact of the nanosize effect towards asphaltene oxidation. In order to further support the TG/DTA results, evolved gas analysis by mass spectrometry is shown in Figure 4.3d. The CO_2 peak (m/e =44) observed by MS (Figure 4.3d) shows clearly the effect of NiO particle size on n-C_5 asphaltenes oxidation. It can be seen that the smaller the particle size the quicker (lower temperature) is the CO_2 formation; depiction higher catalytic activity for oxidation (Nassar et al., 2014). However, the shape of the bigger nanoparticles has been found to be more toward separated tablets, and adsorption results shown the bigger flat surfaces give the impression to have the necessary adsorption sites to organize pretty well big bulky molecules on their top. These big nanotablets shown lower adsorption energy means higher adsorption strength, as result we need more energy to oxidize the adsorbed material on its surface. While the smaller sizes shown more connected sheets and spheres which shown lower adsorption capacity and higher adsorption energy which could be the reason why it is the quicker to oxidize the adsorbed asphaltenes (Marei et al., 2016).

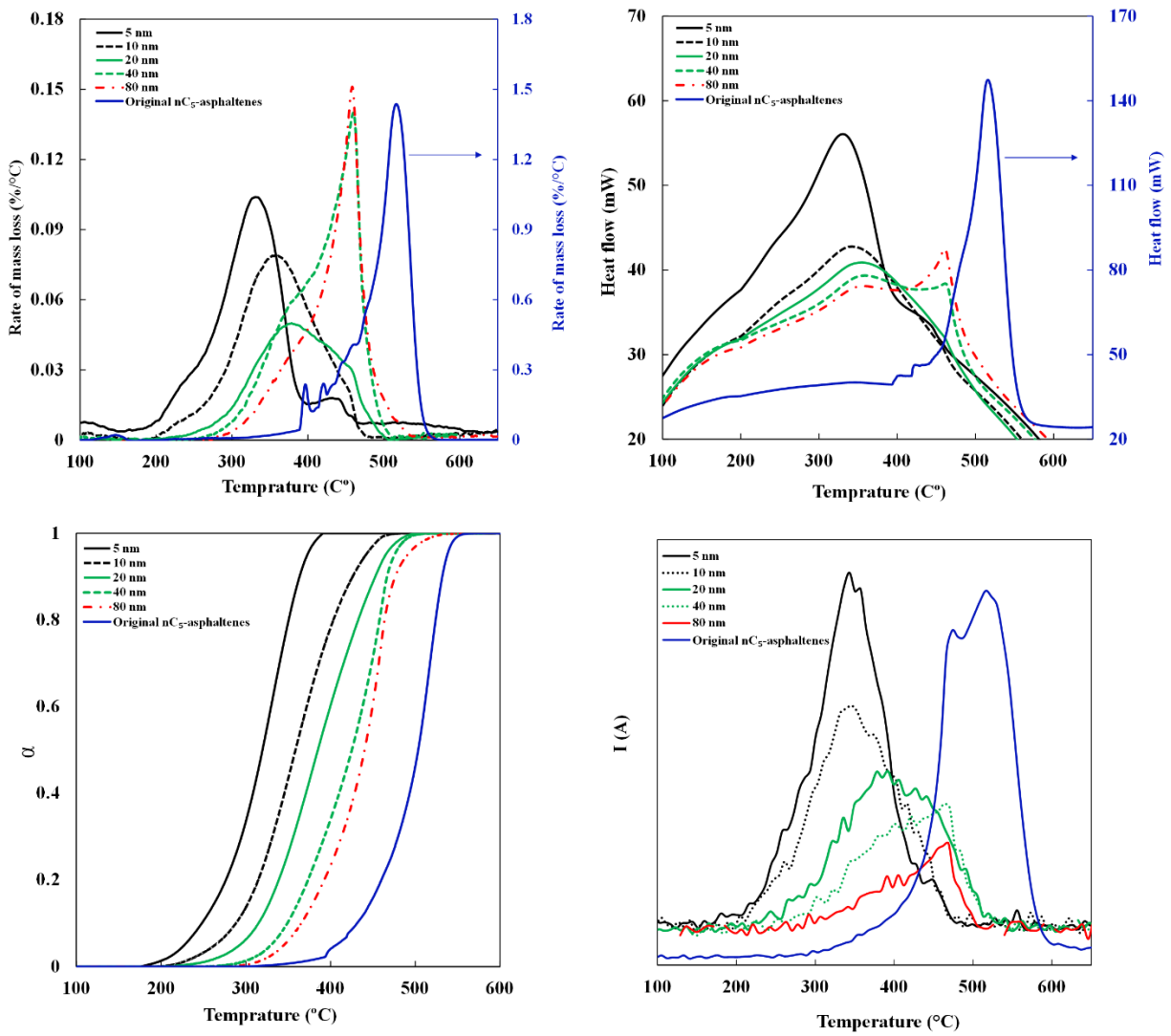

Figure 4.3 TGA-MS plots of n-C_5 asphaltenes oxidation. a) Rate of mass loss for n-C_5 asphaltenes catalytic oxidation in the absence and presence of different-sized NiO, b) plot of heat changes as a function of temperature, c) percent conversion and d) evolution of the production of CO_2. Experimental conditions heating rate = 10 °C/min; air flow, 100 cm^3/min.

4.4.4 Estimation of effective activation energy

Kissinger-Akahira-Sunose (KAS) is used to describe the oxidation mechanism of visbroken residue n-C_5 asphaltenes before and after adsorption onto different-sized NiO nanoparticles, and to confirm the validity of the catalytic effect of the different particle sizes of NiO nanoparticles on the basis of the kinetic triplets (i.e., effective activation energy trends, preexponential factor, and

reaction model). Activation energies were estimated after the catalytic oxidation of n-C_5 asphaltenes adsorbed onto NiO nanoparticles as explained in Chapter 3 (eq 3.2- eq 3.10).

Figure 4.4a and b present the effective activation energy trends as a function of α and T, repectively. The resulting activation energy trends shown in Figure 4.4a for original visbroken n-C_5 asphaltenes demonstrated various trends, suggesting multistep reactions are occurring with a change in the limiting step of the reaction during the oxidation process (Miyazaki, 2009, Vyazovkin, 2016). It is seen that the activation energy trend of original n-C_5 asphaltenes ranged between 120 and 175 kJ/mol. The activation energy trends of n-C_5 asphaltenes oxidized in the presence of different-sized NiO nanoparticles showed different mechanism during oxidation. This indicates that the reaction mechanism is changed. The activation energy trends of 5, 10 and 20 nm showed comparable trends at low conversion values (0.1-0.2). On the other hand 40 and 80 nm demonstrated different trends. At high conversion values between 0.8 and 0.9, the activation energy trends, in most cases, tend to level off at values higher than that for original n-C_5 asphaltenes. Interestingly, 40 nm showed the lowest activation energy trend despite the fact it has the highest value of K parameter of the SLE model (Table 4.2) that corresponds to the degree of asphaltene aggregation on the nanoparticle surface. The higher K values, suggesting a higher effective activation energy trend. This could be attributed to the different morphology of the 40 nm which looks like cylinders (Marei et al., 2016) which might provide more unblocked catalytic active sites on the surface. On the other hand, 10 nm showed the highest activation energy trend. Moreover, the H parameter of the SLE model (Table 4.2) for 10 nm is very low which indicates better affinity. These findings show excellent agreement with Nassar et al (Franco et al., 2015) study that states the higher the adsorption affinity the higher the activation energy. Unexpectedly, 80 nm which has the highest H parameter value did not show the lowest activation energy trend.

However, the q_m parameter of the SLE model that corresponds to the uptake was the highest and K parameter value for self-association was significant when compared to the other sizes of NiO nanoparticles. This could be due to the hexagonal shape of these nanoparticles that affects the interactions between asphaltenes and surface sites depending on the orientation of the functional groups present in the structure of asphaltenes (Marei et al., 2016). This might expose more unblocked catalytic active sites on the surface. Thus, the results of the effective activation energy alone is not the only major parameter to specify the catalytic activity of nanoparticles (Vyazovkin, 2015, Yancey and Vyazovkin, 2014, Mofokeng and Luyt, 2015). When dealing with activation energy profiles, the activation energy at a given point is more an estimate of how sensitive the rate of reaction is to small temperature changes rather than the value of the rate. Therefore, taken together the kinetic triplets, namely E_α, A_α and $f(\alpha)$ can give more meaningful kinetic prediction. Nevertheless, the catalytic effect validity of the different-sized NiO nanoparticles is confirmed in Figure 4.4b.

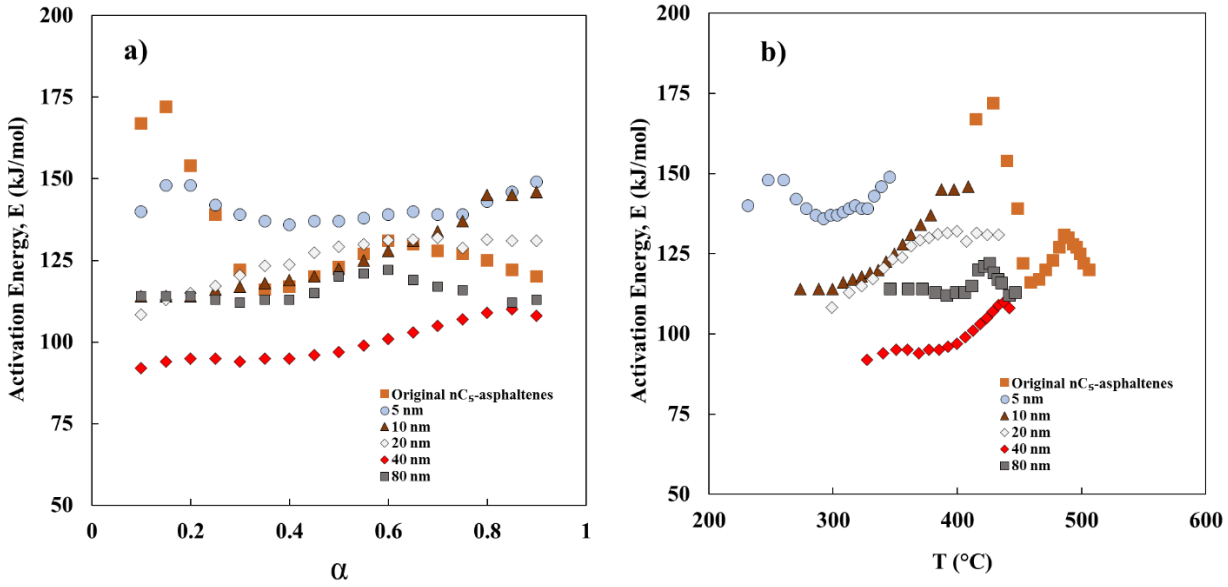

Figure 4.4 Dependencies E_α on: a) α and b) temperature, for thermo-oxidative decomposition of visbroken n-C_5 asphaltenes in presence and absence of NiO nanoparticles studied by thermogravimetry in air. Experimental conditions: heating rate = 5 ºC/min; air flow, 100 cm^3/min.

As seen in Figure 4.4b for the dependency of the effective activation energy as a function of on temperature, the main differences between the NiO nanoparticles and original asphaltenes are observed at the initial and final thermal oxidation stages. This shows good agreement with the MS CO_2 detection results.

4.4.5 Estimation of reaction model function (f (α))

Following the mathematical procedure presented in Chapter 3 and considering different reaction model as proposed by Sestak and Berggren (Šesták and Berggren, 1971), after using eq (3.9) and plotting $\ln(g(\alpha))$ against $ln\left(\frac{\beta_i}{T_{\alpha,i}^2}\right)$, and using a linear regression of the least squares method, the most probable reaction mechanism is determined. Table 4.3 lists the kinetic expressions of $g(\alpha)$ functions used in this study for the solid-state reactions that are given in the literature (Šesták and Berggren, 1971, Nassar et al., 2014). The most probable mechanism function for values of α at a

specified temperature (Tp), corresponds to α = 50% for a heating rate 5 ˚C/min, were applied to calculate the possible mechanism function by substituting α values into $\ln(g(\alpha))$ for all the types of mechanism functions presented in literature (Šesták and Berggren, 1971). The results shown in Table 4.3 indicated that the most probable mechanism functions during the thermo-oxidative process in the absence of NiO nanoparticles was fourth order ($f(\alpha) = (1/4)\ (1-\alpha)^{-3}$) and was fifth order ($f(\alpha) = (1/2)\ (1-\alpha)^{-4}$) for n-$C_5$ asphaltene adsorbed onto NiO nanoparticles in the range between (5-40 nm). Interestingly, bigger NiO nanoparticles between (40-80 nm) showed the same mechanism function of original n-C_5 asphaltenes. This does not clearly explain the trend of catalytic effect of NiO towards n-C_5 asphaltenes oxidation as the oxidation reaction mechanism did not show significant change in the reaction pathway. Therefore, MS CO_2 detection was employed to investigate NiO catalytic effect towards n-C_5 asphaltenes oxidation.

Table 4.3 Most probable mechanism, slopes, and the linear regression coefficients (R^2).

	Mechanism No.	**Slope**	**R^2**
Visbroken residue n-C_5 asphaltenes	4	-1.0000	0.9921
5 nm	5	-0.9738	0.9975
10 nm	5	-0.9302	0.9997
20 nm	5	-0.9302	0.9962
40 nm	4	-0.9130	0.9992
80 nm	4	-0.9130	0.9878

4.4.6 Estimation of pre-exponential factor (A_α)

After knowing the effective activation energies and the most probable mechanism function, the pre-exponential factor A_α is estimated from the intercept of the best-fit-line of the plot of $ln\left(\frac{\beta_i}{T_{\alpha,i}^2}\right)$

against $\frac{1}{T_{\alpha,i}}$, where the intercept equals $\ln\left(-\frac{A_\alpha R}{g_\alpha E_\alpha}\right)$ as per eq (3.9). The obtained pre-exponential factors are shown in Figure 4.5.

The trends of ln A_α upon introducing the NiO nanoparticles followed exactly the trends of activation energy presented in Figure 4.4, confirming the change in the reaction mechanism as compared to original visbroken residue n-C_5 asphaltenes. Noticeably, the values of A_α is higher in the presence of nanoparticles. This could be attributed to the number of active sites presented on the surface of NiO nanoparticles that enhances adsorption and consequently speeds up the reaction rate. Figure 4.5b shows beautiful trend of A_α with temperature for each nanosize. The smaller nanoparticles start and finish before the bigger nanoparticles respectively from 5, 10, 20, 40 and 80 nm. Moreover, the A_α value at each temperature shows higher value for the smaller nanoparticles, suggesting faster reaction or higher acceleration reaction pathway (Yancey and Vyazovkin, 2014).

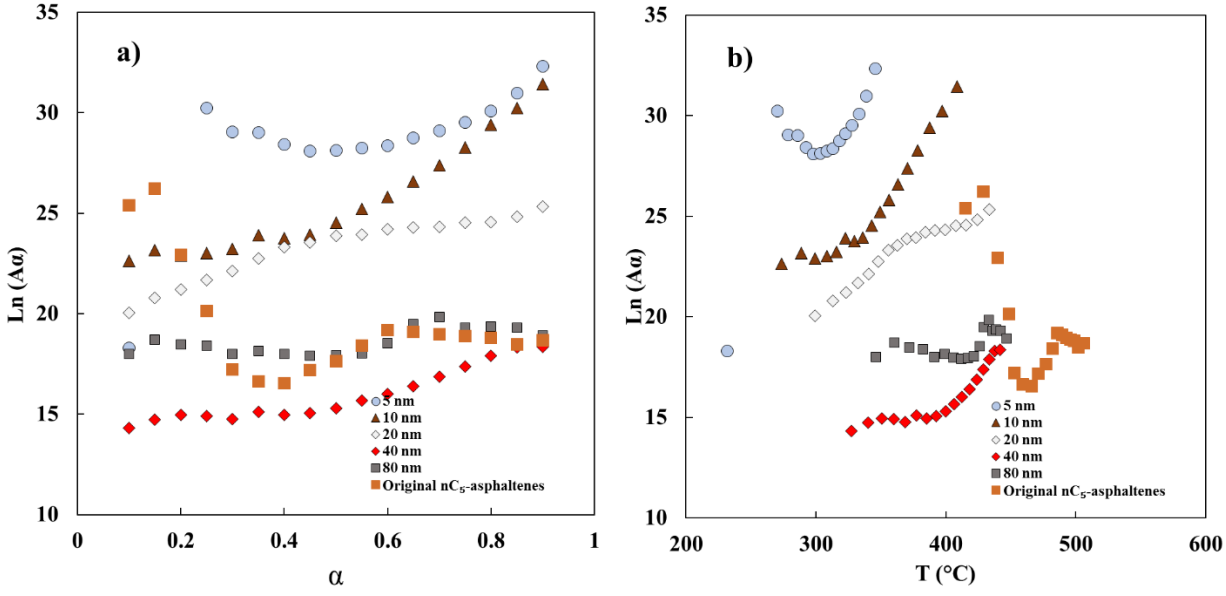

Figure 4.5 Dependencies of A_α on: a) α and b) temperature, for thermo-oxidative decomposition of visbroken n-C_5 asphaltenes in presence and absence of NiO nanoparticles studied by thermogravimetry in air. Experimental conditions: heating rate = 5 ºC/min; air flow, 100 cm^3/min.

4.4.7 Estimation of thermodynamic transition state parameters

The thermodynamic parameters of the transition state functions, namely, changes in Gibbs free energy of activation ($\Delta G^{\ddagger}$), enthalpy of activation ($\Delta H^{\ddagger}$), and entropy of activation ($\Delta S^{\ddagger}$) were estimated to measure the extent of catalytic oxidation of NiO nanoparticles on the oxidation of n-C_5 asphaltenes. These thermodynamics parameters were estimated at the Tp that corresponds to α = 50% at a heating rate 5 ˚C/min (eqs (3.11), (3.12) and (3.13)).

The results of these parameters are shown in Table 4.4. As observed, $\Delta S^{\ddagger}$ values are negative which means that the activated state is less disordered compared to the original n-C_5 asphaltenes. Additionally, the values of $\Delta S^{\ddagger}$ were the lowest in the negative value for 5 and 10 nm indicating a decrease in the entropy and consequently, associative mechanism of the reaction. The positive values of $\Delta G^{\ddagger}$ indicate that the oxidation processes are not spontaneous. Moreover, the smaller the nanosize seems to have lower value of $\Delta G^{\ddagger}$ suggesting more favorable reaction. These findings shows good agreement with TGA-MS analysis and the kinetic triplets results, supporting the fact that the smaller nanosize the higher catalytic activity. Overall, the presence of NiO nanoparticles caused a drop in the values of the thermodynamic parameters, and hence the promising catalytic effect of NiO nanoparticles is confirmed.

Table 4.4 Values of $\Delta S^{\ddagger}$, $\Delta H^{\ddagger}$, and $\Delta G^{\ddagger}$ for the thermos-oxidative decomposition of asphaltenes in the presence and absence of nanoparticles at α = 50%.

	$\Delta S^{\ddagger}$ (**J/mol K**)	$\Delta H^{\ddagger}$ (**kJ/mol**)	$\Delta G^{\ddagger}$ (**kJ/mol**)
Visbroken residue n-C_5 asphaltenes	-148	150	262
5 nm	-22	132	145
10 nm	-45	123	150
20 nm	-78	122	171
40 nm	-126	95	180

	$\Delta S^{\ddagger}$ (J/mol K)	$\Delta H^{\ddagger}$ (kJ/mol)	$\Delta G^{\ddagger}$ (kJ/mol)
80 nm	-106	110	182

From the TGA-MS analysis kinetic triplets and the thermodynamic parameters it is shown that the smaller nanosize have higher a catalytic activity than the bigger nanosizes. These finding can be explained by the fact that the adsorption affinity of the oxygen on the smaller nanoparticles is much higher than the bigger nanoparticles (Campbell, 2013). Which explain the FTIR results that showed higher –OH amount on the smaller nanosize surfaces (Marei et al., 2016a). Moreover, the smaller nanosize could have higher capability to activate O_2 for oxidation reactions due to its stronger bonds with O_2 (Campbell, 2013). The adsorption behavior from Section 4.4.1 could support this fact as well, since SLE constants (like K and H) tend to be higher in the case of the bigger nanoparticles, which indicates a higher asphaltene aggregation possibility and a lower adsorption affinity than the smaller nanoparticles.

4.5 Conclusions

The nanosize effect of NiO nanoparticles on adsorption and post-adsorption catalytic oxidation of visbroken residue n-C_5 asphaltenes was investigated. Different-sized NiO nanoparticles with sizes between 5 and 80 nm were employed for batch adsorption experiments. The adsorption isotherms were described by the solid-liquid equilibrium (SLE) model. On a surface area basis, the adsorption capacity shows significant increase with the size. 80 nm has 10 times adsorption uptake than the 5 nm. Moreover, SLE constants (K and H) decrease with the decreasing of the NiO nanosize from 80 nm to 5 nm, indicates an increasing of the adsorption affinity and decrease of asphaltene aggregation degree. Infrared spectra (FTIR) profiles of visbroken n-C_5 asphaltenes and the different-sized NiO nanoparticles before and after adsorption experiments were obtained. FTIR results show different interaction of adsorbed asphaltenes at different nanosized NiO.

Thermogravimetric analysis of visbroken n-C_5 asphaltenes was also performed and the reaction products were explored by a mass spectrometer. The mass loss, heat flow and CO_2 gas profiles showed that smaller nanoparticles (5 nm) is the faster mass loss and CO_2 production followed by the bigger nanoparticles 10, 20, 40 and 80 nm respectively. The kinetics triplet $f(\alpha)$, E_α and A_α values were estimated using Kissinger-Akahira-Sunose (KAS) to determine the reaction mechanisms and subsequently estimate the transitional thermodynamic parameters, namely $\Delta S^{\ddagger}$,$\Delta H^{\ddagger}$, and $\Delta G^{\ddagger}$. Taken together, kinetic triplets and the thermodynamic parameters showed that the oxidation of n-C_5 asphaltenes on the smaller nanoparticles is more favorable with lower free Gibbs energy values and higher values of the preexponential factor. This confirms that the lower nanosize of NiO nanoparticles the better the catalytic activity.

4.6 References

ACEVEDO, S., RANAUDO, M. A., GARCÍA, C., CASTILLO, J., FERNÁNDEZ, A., CAETANO, M. & GONCALVEZ, S. 2000. Importance of asphaltene aggregation in solution in determining the adsorption of this sample on mineral surfaces. Colloids and Surfaces A: Physicochemical and Engineering Aspects, 166, 145-152.

ADAMS, J. J. 2014. Asphaltene adsorption, a literature review. Energy & Fuels, 28, 2831-2856.

AKBARZADEH, K., HAMMAMI, A., KHARRAT, A., ZHANG, D., ALLENSON, S., CREEK, J., KABIR, S., JAMALUDDIN, A. J., MARSHALL, A. G., RODGERS, R. P., MULLINS, O. C. & SOLBAKKEN, T. 2007. Asphaltenes-problematic but rich in potential. Oilfield Review, 22−43.

AKHLAQ, M. S., GÖTZE, P., KESSEL, D. & DORNOW, W. 1997. Adsorption of crude oil colloids on glass plates: measurements of contact angles and the factors influencing glass surface properties. Colloids and Surfaces A: Physicochemical and Engineering Aspects, 126, 25-32.

BANTIGNIES, J.-L., CARTIER DIT MOULIN, C. & DEXPERT, H. 1998. Asphaltene adsorption on kaolinite characterized by infrared and X-ray absorption spectroscopies. Journal of Petroleum Science and Engineering, 20, 233-237.

CAMPBELL, C. T. 2013. The energetics of supported metal nanoparticles: relationships to sintering rates and catalytic Activity. Accounts of Chemical Research, 46, 1712-1719.

EL-QANNI, A., NASSAR, N. N., VITALE, G. & HASSAN, A. 2016. Maghemite nanosorbcats for methylene blue adsorption and subsequent catalytic thermo-oxidative decomposition: Computational modeling and thermodynamics studies. Journal of Colloid and Interface Science, 461, 396-408.

FRANCO, C., PATIÑO, E., BENJUMEA, P., RUIZ, M. A. & CORTÉS, F. B. 2013a. Kinetic and thermodynamic equilibrium of asphaltenes sorption onto nanoparticles of nickel oxide supported on nanoparticulated alumina. Fuel, 105, 408-414.

FRANCO, C. A., MONTOYA, T., NASSAR, N. N., PEREIRA-ALMAO, P. & CORTÉS, F. B. 2013b. Adsorption and subsequent oxidation of Colombian asphaltenes onto nickel and/or palladium oxide supported on fumed silica nanoparticles. Energy & Fuels, 27, 7336-7347.

FRANCO, C. A., NASSAR, N. N., MONTOYA, T. & CORTÉS, F. B. 2014. NiO and PdO supported on fumed silica nanoparticles for adsorption and catalytic steam gasification of Colombian C_7-asphaltenes. In: AMBROSIO, J. (ed.) Handbook on Oil Production Research. Hauppauge, N.Y. USA: Nova Science Publishers, Inc.

FRANCO, C. A., NASSAR, N. N., MONTOYA, T., RUÍZ, M. A. & CORTÉS, F. B. 2015. Influence of asphaltene aggregation on the adsorption and catalytic behavior of nanoparticles. Energy & Fuels, 29, 1610-1621.

FRANCO, C. A., NASSAR, N. N., RUIZ, M. A., PEREIRA-ALMAO, P. R. & CORTÉS, F. B. 2013c. Nanoparticles for inhibition of asphaltenes damage: adsorption study and displacement test on porous media. Energy & Fuels, 27, 2899−2907.

FREUNDLICH, H. M. F. 1906. Uber die adsorption in losungen. Zeitschrift fur Physikalische Chemie, 57, 385-470.

GABORIAU, H. & SAADA, A. 2001. Influence of heavy organic pollutants of anthropic origin on PAH retention by kaolinite. Chemosphere, 44, 1633-1639.

HASHEMI, R., NASSAR, N. N. & PEREIRA ALMAO, P. 2013. Enhanced heavy oil recovery by in situ prepared ultradispersed multimetallic nanoparticles: A study of hot fluid flooding for Athabasca bitumen recovery. Energy & Fuels, 27, 2194-2201.

HASHEMI, R., NASSAR, N. N. & PEREIRA ALMAO, P. 2014a. In situ upgrading of athabasca bitumen using multimetallic ultradispersed nanocatalysts in an oil sands packed-bed column: Part 1. produced liquid quality enhancement. Energy & Fuels, 28, 1338-1350.

HASHEMI, R., NASSAR, N. N. & PEREIRA ALMAO, P. 2014b. Nanoparticle technology for heavy oil in-situ upgrading and recovery enhancement: Opportunities and challenges. Applied Energy, 133, 374-387.

HASSAN, A., CARBOGNANI-ARAMBARRI, L., NASSAR, N. N., VITALE, G., LOPEZ-LINARES, F. & PEREIRA-ALMAO, P. 2015. Catalytic steam gasification of n-C_5 asphaltenes by kaolin-based catalysts in a fixed-bed reactor. Applied Catalysis A: General, 507, 149-161.

HASSAN, A., LOPEZ-LINARES, F., NASSAR, N. N., CARBOGNANI-ARAMBARRI, L. & PEREIRA-ALMAO, P. 2013. Development of a support for a NiO catalyst for selective adsorption and post-adsorption catalytic steam gasification of thermally converted asphaltenes. Catalysis Today, 207, 112-118.

HMOUDAH, M., NASSAR, N. N., VITALE, G. & EL-QANNI, A. 2016. Effect of nanosized and surface-structural-modified nano-pyroxene on adsorption of Violanthrone-79. Nanoscale (Under Review).

HOSSEINPOUR, N., KHODADADI, A. A., BAHRAMIAN, A. & MORTAZAVI, Y. 2013. Asphaltene adsorption onto acidic/basic metal oxide nanoparticles toward in situ upgrading of reservoir oils by nanotechnology. Langmuir, 29, 14135-14146.

KUMAR, K., DAO, E. & MOHANTY, K. K. 2005. AFM study of mineral wettability with reservoir oils. Journal of Colloid and Interface Science, 289, 206-217.

LANGMUIR, I. 1918. The adsorption of gases on plane surfaces of glass, mica and platinum. Journal of the American Chemical society, 40, 1361-1403.

LÓPEZ-LINARES, F., CARBOGNANI, L., SOSA-STULL, C., PEREIRA-ALMAO, P. & SPENCER, R. J. 2009. Adsorption of original and visbroken residue asphaltenes over solid surfaces. 1. Kaolin, smectite clay minerals, and Athabasca siltstone. Energy & Fuels, 23, 1901-1908.

MAREI, N. N., NASSAR, N. N. & VITALE, G. 2016a. The effect of the nanosize on surface properties of NiO nanoparticles for the adsorption of Quinolin-65. Physical Chemistry Chemical Physics, 18, 6839-49.

MAREI, N. N., NASSAR, N. N., VITALE, G. & HASSAN, A. 2016b. Catalytic effect of nanosized NiO nanoparticles in thermo-oxidative decomposition of Quinolin-65. To be submitted to Catalysis Science & Technology Journal, RSC.

MARLOW, B. J., SRESTY, G. C., HUGHES, R. D. & MAHAJAN, O. P. 1987. Colloidal stabilization of clays by asphaltenes in hydrocarbon media. Colloids and Surfaces, 24, 283-297.

MENON, V. B. & WASAN, D. T. 1987. Particle--fluid interactions with applications to solid-stabilized emulsions Part III. Asphaltene adsorption in the presence of quinaldine and 1,2-dimethylindole. Colloids and Surfaces, 23, 353-362.

MIRZAYI, B. & SHAYAN, N. N. 2014. Adsorption kinetics and catalytic oxidation of asphaltene on synthesized maghemite nanoparticles. Journal of Petroleum Science and Engineering, 121, 134-141.

MITTAL, K. L. & SHAH, D. O. 2002. Adsorption and aggregation of surfactants in solution, CRC Press.

MIYAZAKI, T., SIVAPRAKASAM, K., TANTRY, J. & SURYANARAYANAN, R. 2009. Physical characterization of dibasic calcium phosphate dihydrate and anhydrate. J Pharm Sci, 98, 905-16.

MOFOKENG, J. P. & LUYT, A. S. 2015. Morphology and thermal degradation studies of melt-mixed poly(lactic acid) (PLA)/poly(ε-caprolactone) (PCL) biodegradable polymer blend nanocomposites with TiO2 as filler. Polymer Testing, 45, 93-100.

MONTOYA, T., CORAL, D., FRANCO, C. A., NASSAR, N. N. & CORTÉS, F. B. 2014. A Novel Solid-Liquid Equilibrium Model for Describing the Adsorption of Associating Asphaltene Molecules onto Solid Surfaces Based on the “Chemical Theory”. Energy & Fuels.

MULLINS, O. C., SABBAH, H., EYSSAUTIER, J., POMERANTZ, A. E., BARRE, L., ANDREWS, A. B., RUIZ-MORALES, Y., MOSTOWFI, F., MCFARLANE, R., GOUAL, L., LEPKOWICZ, R., COOPER, T., ORBULESCU, J., LEBLANC, R. M., EDWARDS, J.

& ZARE, R. N. 2012. Advances in Asphaltene Science and the Yen-Mullins Model. Energy & Fuels, 26, 3986-4003.

NASSAR, N. N., BETANCUR, S., ACEVEDO, S., FRANCO, C. A. & CORTÉS, F. B. 2015. Development of a population balance model to describe the influence of shear and nanoparticles on the aggregation and fragmentation of asphaltene aggregates. Industrial & Engineering Chemistry Research, 54, 8201-8211.

NASSAR, N. N., FRANCO, C. A., MONTOYA, T., CORTÉS, F. B. & HASSAN, A. 2015. Effect of oxide support on Ni-Pd bimetallic nanocatalysts for steam gasification of n-C_7 asphaltenes. Fuel, 156, 110-120.

NASSAR, N. N., HASSAN, A., CARBOGNANI, L., LOPEZ-LINARES, F. & PEREIRA-ALMAO, P. 2012. Iron oxide nanoparticles for rapid adsorption and enhanced catalytic oxidation of thermally cracked asphaltenes. Fuel, 95, 257-262.

NASSAR, N. N., HASSAN, A., LUNA, G. & PEREIRA-ALMAO, P. 2013a. Kinetics of the catalytic thermo-oxidation of asphaltenes at isothermal conditions on different metal oxide nanoparticle surfaces. Catalysis Today, 207, 127-132.

NASSAR, N. N., HASSAN, A. & PEREIRA-ALMAO, P. 2011a. application of nanotechnology for heavy oil upgrading: catalytic steam gasification/cracking of asphaltenes. Energy & Fuels, 25, 1566-1570.

NASSAR, N. N., HASSAN, A. & PEREIRA-ALMAO, P. 2011b. Comparative oxidation of adsorbed asphaltenes onto transition metal oxide nanoparticles. Colloids and Surfaces A: Physicochemical and Engineering Aspects, 384, 145-149.

NASSAR, N. N., HASSAN, A. & PEREIRA-ALMAO, P. 2011c. Effect of surface acidity and basicity of aluminas on asphaltene adsorption and oxidation. Journal of Colloid and Interface Science, 360, 233-238.

NASSAR, N. N., HASSAN, A. & PEREIRA-ALMAO, P. 2011d. Effect of the particle size on asphaltene adsorption and catalytic oxidation onto alumina particles. Energy & Fuels, 25, 3961-3965.

NASSAR, N. N., HASSAN, A. & PEREIRA-ALMAO, P. 2011e. Metal oxide nanoparticles for asphaltene adsorption and oxidation. Energy & Fuels, 25, 1017-1023.

NASSAR, N. N., HASSAN, A. & PEREIRA-ALMAO, P. 2013b. Clarifying the catalytic role of NiO nanoparticles in the oxidation of asphaltenes. Applied Catalysis A: General, 462–463, 116-120.

NASSAR, N. N., HASSAN, A. & VITALE, G. 2014. Comparing kinetics and mechanism of adsorption and thermo-oxidative decomposition of Athabasca asphaltenes onto TiO_2, ZrO_2, and CeO_2 nanoparticles. Applied Catalysis A: General, 484, 161-171.

ORTEGA, L. C., ROGEL, E., VIEN, J., OVALLES, C., GUZMAN, H., LOPEZ-LINARES, F. & PEREIRA-ALMAO, P. 2015. Effect of precipitating conditions on asphaltene properties and aggregation. Energy & Fuels, 29, 3664-3674.

PERNYESZI, T. & DÉKÁNY, I. 2001. Sorption and elution of asphaltenes from porous silica surfaces. Colloids and Surfaces A: Physicochemical and Engineering Aspects, 194, 25-39.

PERNYESZI, T., PATZKÓ, Á., BERKESI, O. & DÉKÁNY, I. 1998. Asphaltene adsorption on clays and crude oil reservoir rocks. Colloids and Surfaces A: Physicochemical and Engineering Aspects, 137, 373-384.

POLANYI, M. 1914. Adsorption from the point of view of the Third Law of Thermodynamics. Verh. Deut. Phys. Ges, 16, 1012-1016.

PRAUSNITZ, J. M., LICHTENTHALER, R. N. & DE AZEVEDO, E. G. 1998. Molecular thermodynamics of fluid-phase equilibria, Pearson Education.

SAADA, A., SIFFERT, B. & PAPIRER, E. 1995. comparison of the hydrophilicity/hydrophobicity of illites and kaolinites. Journal of Colloid and Interface Science, 174, 185-190.

SAKANISHI, K., SAITO, I., WATANABE, I. & MOCHIDA, I. 2004. Dissolution and demetallation treatment of asphaltene in resid using adsorbent and oil-soluble Mo complex. Fuel, 83, 1889-1893.

SHEU, E., LONG, Y. & HAMZA, H. 2007. Asphaltene self-association and precipitation in solvents-ac conductivity measurements. In: MULLINS, O. C., SHEU, E. Y., HAMMAMI, A. & MARSHALL, A. G. (eds.) Asphaltenes, Heavy Oils, and Petroleomics. New York: Springer.

SPIECKER, P. M., GAWRYS, K. L. & KILPATRICK, P. K. 2003a. Aggregation and solubility behavior of asphaltenes and their subfractions. Journal of colloid and interface science, 267, 178-193.

SPIECKER, P. M., GAWRYS, K. L., TRAIL, C. B. & KILPATRICK, P. K. 2003b. Effects of petroleum resins on asphaltene aggregation and water-in-oil emulsion formation. Colloids and surfaces A: Physicochemical and engineering aspects, 220, 9-27.

VYAZOVKIN, S. 2015. Isoconversional kinetics of thermally stimulated processes, Springer International Publishing.

WITTHAYAPANYANON, A., HARWELL, J. & SABATINI, D. 2008. Hydrophilic–lipophilic deviation (HLD) method for characterizing conventional and extended surfactants. Journal of colloid and interface science, 325, 259-266.

YANCEY, B. & VYAZOVKIN, S. 2014. Venturing into kinetics and mechanism of nanoconfined solid-state reactions: trimerization of sodium dicyanamide in nanopores. Physical Chemistry Chemical Physics, 16, 11409-11416.

CHAPTER FIVE: CONCLUSION AND RECOMMENDATIONS

Each chapter in this thesis has its own separate detailed conclusion. Only key findings and remarkable conclusions are presented below, followed by recommendations for future work in this area of studies.

5.1 Conclusions

The effect of nanosize on surface properties of NiO nanoparticles as (nanosorbcats) for adsorptive removal, and subsequent thermo-oxidative decomposition of heavy hydrocarbons was carefully investigated for this study. Initially, the study was conducted on Quinolin-65 (Q-65) as a model molecule mimicking asphaltenes for its remarkable similar molecular characteristics. It was then further validated by using visbroken residue n-C_5 asphaltenes.

Nanoparticles of sizes between 5 to 80 nm NiO were prepared in-house using the controlled thermal dehydroxylation method. The prepared nanoparticles were tested and characterized with the following results,

- The High resolution transmission electron microscopy (HRTEM) images revealed different nanoparticles shapes with different sizes.
- The FTIR analysis identified the difference between the framework group and the hydroxyl density with different nanosizes.
- The TGA analysis showed that the higher the nanosize, the less the hydroxyl surface content, which provides more chances for the adsorption of Q-65 and n-C_5 asphaltenes molecules.

Computational modeling was studied to gain better insight into the Q-65 interaction with NiO nanoparticles, with the assumption of spherical or tablet-like shape nanoparticles in order to study the effect of shape on the morphology and the atomic distribution together, and on the adsorptive behavior. The results of the experimental adsorption isotherms (molecule per nm^2), support the

characteristic studies and confirms that the smaller NiO nanoparticles with a 5 nm size have the lowest adsorption capacity, while the 80 nm size particles have the highest uptake.

Langmuir and Freundlich adsorption isotherms models were employed to describe the Q-65 experimental isotherms. The data presented a better fit with the Langmuir model suggesting a monolayer adsorption on all NiO sizes. For the n-C_5 asphaltene adsorption, the solid-liquid equilibrium (SLE) model was applied to understand the adsorption behavior and the asphaltene aggregation on the NiO nanoparticles. Interestingly, SLE constants K and H, tend to be higher in the case of the bigger nanoparticles, which indicates a higher asphaltene aggregation possibility and a lower adsorption affinity, than the smaller nanoparticles.

Thermogravimetric experiments on the adsorbed Q-65 and n-C_5 asphaltenes were performed where the reaction products were probed by an online mass spectrometer. To measure the rate of mass loss and CO_2 evolution profiles. The set of reliable $f(\alpha)$, E_α and A_α frequently called the kinetic triplets, were estimated using the Kissinger-Akahira-Sunose (KAS) to determine the reaction mechanisms and estimate the transitional thermodynamic parameters, namely $\Delta S^{\ddagger}$, $\Delta H^{\ddagger}$, and $\Delta G^{\ddagger}$.

In conclusion, nanosize plays a vital role in selective adsorption and subsequently, in the catalytic decomposition of heavy hydrocarbons. This study widens our understanding of the metal-based nanoparticles' functionality and chemical activity, and opens up new possibilities for countless research in this area. These findings can be directly applied in the oil and gas industry in particular for the crude oil upgrading and recovery processes.

5.2 Recommendations for future work

- Using different model molecules mimicking the asphaltenes as Perylene-based family. Due its close chemical structure and similar solubility properties. To get better understanding for the aromaticity, heteroatoms and polarity in the adsorption process.
- Using different asphaltenes from different origins and different refinery units. Since, asphaltenes is a product of different units at the refinery with different characteristics. That will help to decide which asphaltenes is easier to remove and catalytic decomposing.
- Employing this study using different nanoparticles with and without support, considering the cost feasibility and the environmental impact of the real application.
- Run a computational simulation to get better insights of the asphaltene model molecule oxidation process mechanism.
- Scaling up the process; dynamic adsorption experiment followed by post-adsorption catalytic decomposition processes, such as: hydrocracking and pyrolysis of the adsorbed species.

APPENDIX A

A.1 Conversion degree (α) at different heating rates

The conversion degree (α) and is equal to $(m_o - m_t)/(m_o - m_f)$; m_o, m_t, and m_f are the initial mass of sample, current mass of sample at temperature of time t, and final mass of sample at a temperature at which the mass loss is approximately unchanged. As mentioned in Chapter 3 each sample was oxidized at three different heating rates of 5, 10, and 20 °C/min, in separate experiments, in an air atmosphere. Figure A.1 shows Quinolin-65 oxidation in the presence and absence of nanoparticles as a function of temperature at three different heating rates. As anticipated, the rate of mass loss changes with the heating rate: at a fixed temperature, a slower heating rate yields a higher α.

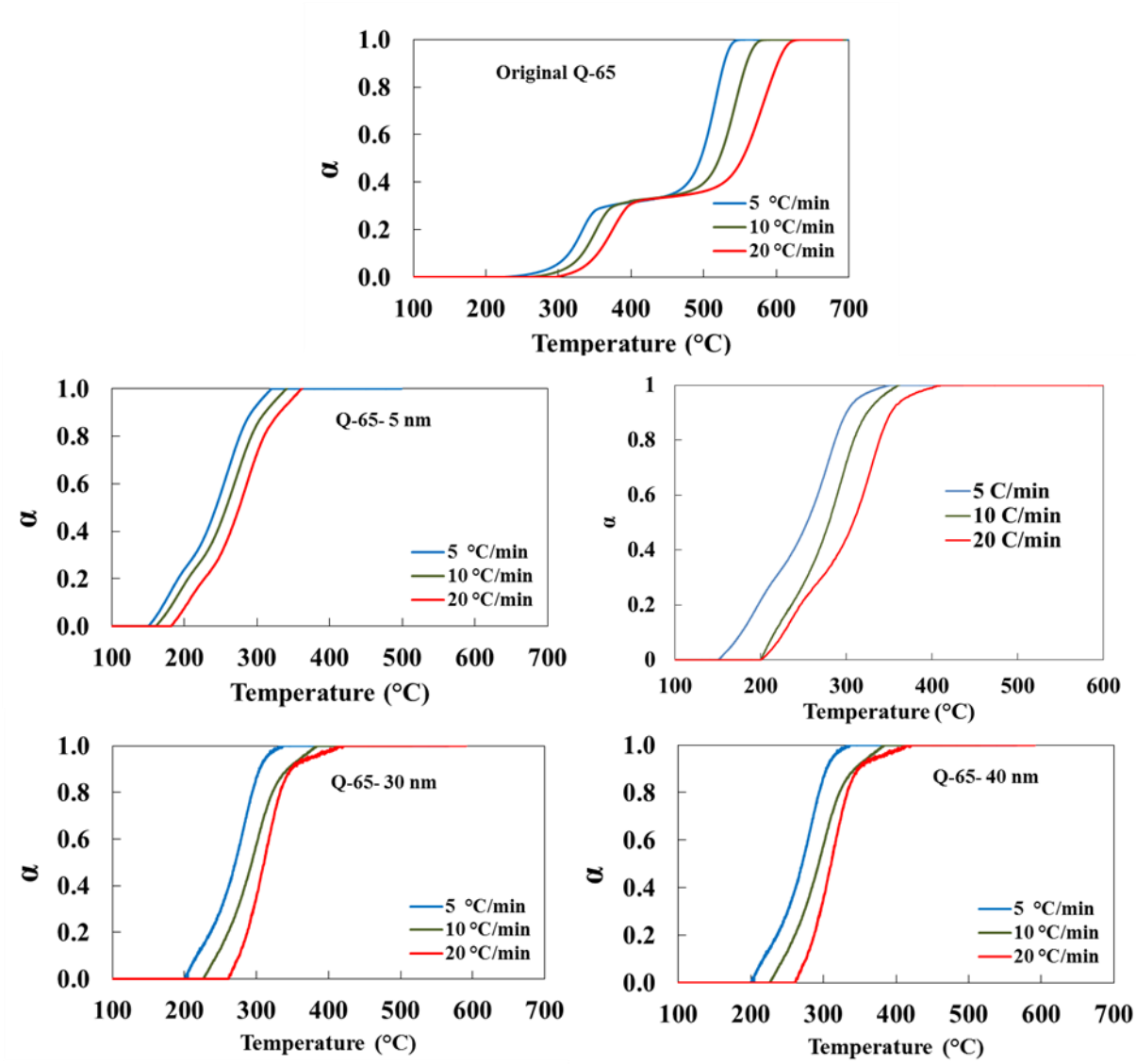

Figure A.1 Conversion of Q-65 at different three heating rates in the presence and absence of NiO different nanosized as a function of temperature at 100 cm^3 air flow.

A.2 plotting $\ln(g(\alpha))$ against $ln\left(\frac{\beta_i}{T^2_{\alpha,i}}\right)$

Eq (3.9) was used to determine the most correct reaction function by plotting $\ln(g(\alpha))$ against $\ln(\beta)$ and using a linear regression of the least squares method. If the considered mechanism complies with the specified $g(\alpha)$ function, then the slope of the best-fit-line should be equal to -1 and the linear correlation coefficient, $R^2 = 1.0$. Figure A.2 shows the plots of selected mechanisms for original Q-65 oxidation.

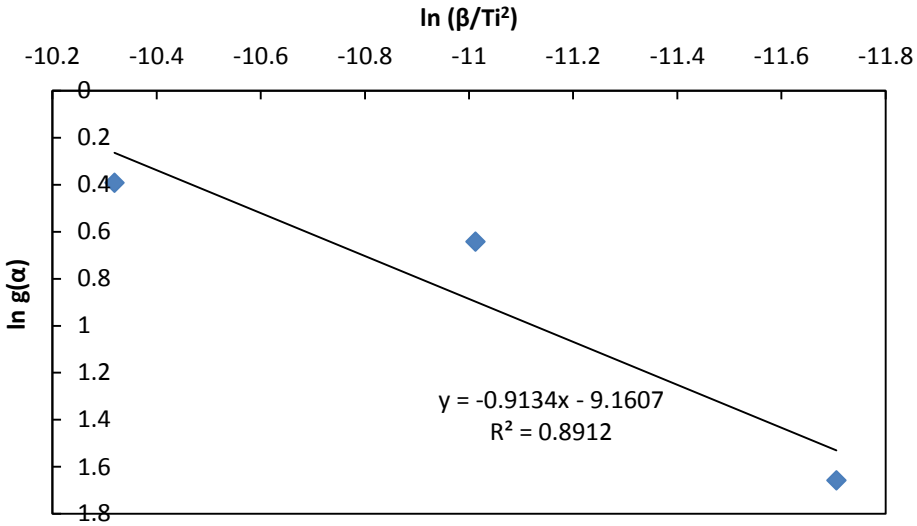

Figure A.2 Plots of $\ln(g(\alpha))$ against $ln\left(\frac{\beta_i}{T^2_{\alpha,i}}\right)$ and linear regression, eq (3.9), for the oxidation of Original Q-65.

A.3 Error analysis

Error bars on adsorption figures were estimated, where the concentration is the independent variable and the UV absorbance is the dependent variable being recorded using UV-Vis Spectrophotometer. Selected samples were repeated 3 times in order to estimate the standard deviation.

$$\sigma = \sqrt{\frac{\sum(x-\bar{x})^2}{N}} \quad \text{(A1)}$$

Where σ is the standard deviation, x is each valu of adsorption uptake, $\bar{x}$ is the mean value of the adsorption uptake and N is the number of values which is 3.

By dividing the standard deviation by the square root of N, the standard error grows smaller as the number of measurements (N) grows larger.